GLIDE BLOCK OR OUT-RUNNER BLOCK IMPACT ON SUSPENDED SUBMARINE PIPELINE

KEN FAI CHI

GLIDE BLOCK OR OUT-RUNNER BLOCK IMPACT ON SUSPENDED SUBMARINE PIPELINE

by

© **Ken Fai Chi**

A Thesis submitted to the

School of Graduate Studies

in partial fulfillment of the requirements for the degree of

Masters of Engineering

Faculty of Engineering and Applied Science

Memorial University of Newfoundland

August 2012

St. John's Newfoundland

ABSTRACT

Due to the high demand of oil and gas, offshore exploration and development are forced to explore and/or develop near areas of potential slope failure. A glide block or out-runner block is the product of a slope failure and can cause great damage on offshore structures, such as a submarine pipeline, since it can travel a long distance from its origin and carries the soil properties of the parent slide.

To better understand the drag force generated from a glide block or out-runner block on to a suspended submarine pipeline, 11 physical tests were conducted to quantify it and are presented in this thesis. The tests were conducted in a geotechnical centrifuge located at C-CORE under submerged conditions with a centrifugal force of 30 times the Earth's gravity (i.e., N = 30) and simulated impact situations under steady state conditions and uniform velocities. The soil blocks (approximately 4.5 m high in prototype terms) were made of kaolin clay with undrained shear strengths ranged from 4 to 8 kPa. The model pipes were 6.35 and 9.52 mm in diameter, which corresponds to 0.19 and 0.29 m in prototype. The impact velocities ranged from 0.04 to 1.3 m/s. The pipe centerline was at mid-height of the block. The shear strain rates, defined as the ratio of impact velocity to pipe diameter, in the centrifuge model are N times higher than that in the prototype, and it ranged from 4 to 137 reciprocal seconds. Hence, the test results are applicable to a wide range of field situations. A geotechnical approach was adapted, based on the results of the centrifuge tests, and a method is presented for estimating drag force for soil block impacting on submarine pipeline.

ACKNOWLEDGEMENTS

I would like to thank my supervisors, Dr. Bipul Hawlader, an Associate Professor in the Faculty of Engineering and Applied Science at Memorial University, and Dr. Arash Zakeri, the former Director of the Geotechnical Engineering group from C-CORE and currently a Senior Geotechnical Engineer at BP America, for their patience, guidance, and encouragements throughout the Master program.

I also would like to thank the members of Geotechnical Group - Brad Elliott, Gerry Piercey, Derry Nicholl, Don Cameron, Karl Tuff and Andrew Macneill, for their dedicated support and advice for making this experiment successful.

I would like to acknowledge C-CORE and MITACS for providing graduate student funding and research expenses.

Most of all, I would like to thank my wife, Xiaoli and daughter, Jiayi for their love, encouragement, and support throughout the program.

Table of Contents

List of Tables

List of Figures

List of Symbols

α	Deflection angle of pipeline
A	Area
B	Coefficient of lateral stability
c_v	Coefficient of consolidation
d	Outer diameter of T- bar
D	Outer diameter of pipe
f_b	Buoyancy force per unit length
F_B	Buoyancy force
f_d	Drag force per unit length in the lateral direction
F_D	Drag force in the lateral direction
$F_{Da,d}$	Axial drag force in the down slope direction
$F_{Da,u}$	Axial drag force in the upslope direction
F_v	Hydrodynamic lift force per unit length
g	Gravity
G_s	Specific gravity
h	Distance measured from the soil surface to pipe center
h_i	Depth where vertical stress in model and prototype are identical
h_m	Depth, in model
h_p	Depth, in prototype
k	Drag force coefficient
k_r	Drag force coefficient at a reference point

l	Length of T-bar
L	Length
n	Dimensionless parameter
N	Number of times larger than Earth's acceleration
N_b	T-bar factor
N_c	Bearing capacity factor
P	Force acting on T-bar
r	The distance from the central axis of rotation
r_e	Effective radius
r_t	The radius to the top of the soil model
r_u	Ratio of the maximum under stress
r_o	Ratio of the maximum over stress
S_t	Sensitivity of clay
s_u	Intact undrained shear strength of clay
s_{um}	Intact undrained shear strength of clay at mud line
s_{ur}	Remoulded undrained shear strength of clay
V	Velocity
V_r	Velocity at a reference point
V_{disp}	Volume of displaced fluid
W	Width
y	Undrained shear strength gradient with depth
ε	Strain

Δ	Relative distance to the pipe diameter
$\dot{\gamma}$	Shear strain rate
σ	Total stress
σ_v	Vertical total stress
σ_{vm}	Vertical stress in model
σ_{vp}	Vertical stress in prototype
ρ	Soil density
ρ_f	Density of fluid
ω	Angular velocity of rotation
w	Moisture content
ϕ	Angle between the longitudinal pipe axis and the moving soil

Chapter 1

Introduction

1.1 General

Submarine landslides and the associated mass movement can potentially have devastating consequences on seafloor installations such as pipelines, flow lines, well systems, cables, etc. Submarine landslides occur frequently on both passive and active continental margins and slopes, releasing sediment volumes that may travel distances as long as hundreds of kilometres on gentle slopes (0.5 to 3°) over the course of less than an hour to several days (Nadim and Locat, 2005). The movement of landslide and the released sediment volumes are often called "density flows". From the initiation to deposition, density flows undergo complex processes that depend on many factors such as the composition, strength characteristics and properties, terrain topography, etc.

Geohazard can be defined as a geological state, which represents or has the potential to develop further into a situation leading to damage or uncontrolled risk (Vanneste, 2010). Typical geohazards are schematically shown in Figure 1.1. Triggering of these events can be caused by natural events or by human activities (Masson et al., 2006). Research on understanding the mechanisms behind and the risks posed by submarine landslides has increased in the past decade, mainly because of the increasing number of deep-water petroleum fields that have been discovered and developed in some cases. The development and production from offshore fields in the areas of previous

sliding activities are ongoing in the Norwegian margin, Gulf of Mexico, offshore Brazil, the Caspian Sea and West Africa (Nadim and Locat, 2005).

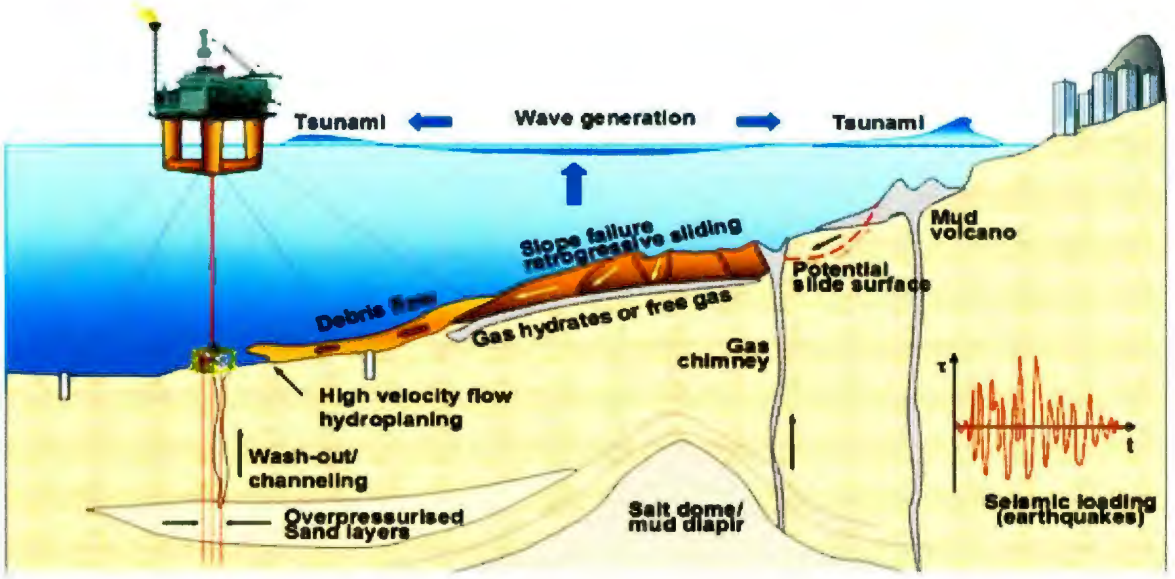

Figure 1.1: Schematic diagram showing main offshore geohazards (Vanneste, 2010).

The drag force on pipelines caused by density flow impact is an important design consideration in offshore engineering. For buried pipelines in cohesive soils in slowly moving unstable slopes, the available methods seem to provide more or less reasonable estimates for the drag force normal to the pipe axis. In cohesive soils, the magnitude of the drag force is a function of the rate at which the soil is sheared during interaction with the pipe. Recent works done by Zakeri et al. (2008, 2009b, 2009c) provide a method for estimating drag forces caused by a fully remoulded and fluidized clay-rich debris flow impacting a pipeline normal to its axis. Later, the work was extended to cover the angles of impact (Zakeri, 2009).

The present study deals with quantification of the drag force from glide blocks or out-runner blocks impacting suspended submarine pipelines at an angle normal to its

axis. Glide blocks and out-runner blocks are essentially an intact block of soil from its original source (see Chapter 2 for more details on the definition). Eleven physical tests were carried out in the geotechnical centrifuge at C-CORE under submerged conditions at a centrifugal force of 30 times the Earth's gravity. The tests simulated an approximate 12 m long, 6 m wide and 4.5 m high intact glide block or out-runner block (made from kaolin clay), with undrained shear strengths ranging from 4 to 8 kPa, impacting a suspended submarine pipeline at velocities ranging from 0.04 to 1.30 m/s at mid-height of the clay block. The diameter of the model pipes were 6.35 and 9.52 mm, which correspond to 0.19 and 0.29 m in prototype terms. The shear strain rates, defined as the ratio of impact velocity to pipe diameter, ranged from 4 to 137 reciprocal seconds, corresponding to 0.13 to 4.57 reciprocal seconds in prototype terms. As such, the test results are applicable to a wide range of field impact situations.

Further, this thesis adopts the geotechnical approach and presents a method for estimating the drag force generated by the impact of glide block or out-runner block onto suspended submarine pipelines, based on the results from the centrifuge experiment.

1.2 The Objectives

The main objective of this thesis is to develop an empirical formula to estimating the drag force on a suspended offshore pipeline generated from a submarine landslide in the form of a glide block or out-runner block. Since a glide block and out-runner block is an intact block of soil whose strength is the same as its original source, the geotechnical approach is adapted. The drag force is a function of the projected area (length and diameter of the pipe), soil strength, and the interaction between soil and the pipe. The

main interest of this study is to model cohesive soil (clay) block on pipelines. As the undrained shear strength of clay depends on strain rate, the experiments are conducted at a range of impact velocities to simulate the effects of strain rate on impact force.

1.3 Organization of Thesis

This thesis includes 5 Chapters and 1 Appendix. Chapter 1 is an introduction that describes the reason behind developing a method for estimating a glide block or out-runner block impact drag force on submarine pipelines. The objectives for this experimental program and the contributions from this work are also described in this chapter.

Chapter 2 is the literature review related to this study. The first section of this chapter provides the terminology and definition used in this thesis. Case studies from previous submarine landslides and their consequences are shown. The methods available in the literature which may be used to estimate the submarine landslide impact drag force on submarine pipelines and piles are also discussed.

Chapter 3 of this thesis is for experimental setup. A brief overview of the principal in centrifuge modeling and scaling laws are discussed. Experimental setup and instrumentations, soil specimen preparation and test procedures are discussed in this chapter.

Experimental results are analyzed and are located in Chapter 4 of this thesis. Based on the analysis, an equation has been proposed for estimating drag force. A worked example is given showing the use of proposed method.

In Chapter 5, the conclusions and further recommendations are presented.

The appendix at the end presents some additional information about this study. Instrumentation calibrations, lab-floor consolidation results, consolidation in-flight, undrained shear strength and moisture content profile in clay blocks are presented here.

1.4 Original Contribution

In addition to the technical contribution presented in this thesis, the following four (one journal and three conference) papers have been published from this research work.

1. Zakeri, A., Hawlader, B. C. and Chi, K. (2011). "Drag forces caused by submarine glide block or out-runner block impact on suspended (free-span) pipelines." Ocean Engineering, Vol. 47, pp. 50-57.

2. Chi, K., Zakeri, A. and Hawlader, B. C. (2011). "Centrifuge Modeling of Subaqueous and Subaerial Landslides Impact on Suspended Pipelines." Proc. 2011 Pan-American CGS Geotechnical Conference, Toronto, Canada, October 2–6, Paper ID 707, 5p.

3. Zakeri, A., Chi, K. and Hawlader, B. (2011). "Centrifuge Modeling of Glide Block and Out-runner Block Impact on Submarine Pipelines" Proc. Offshore Technology Conference, Houston, Texas, USA, 2–5 May 2011. OTC 21256, 9p.

4. Chi, K., Zakeri, A., and Hawlader, B. (2011). "Modeling of Submarine Glide Block Impact on Pipelines" Proc. 5th International Symposium on Submarine Mass Movements and Their Consequences, Kyoto, Japan, October 24-26, 8p.

Chapter 2

Literature Review

2.1 Terminology and Definition

Mulder and Alexander (2001) attempts to clarify the classification of sedimentary density flow based on physical flow properties and grain-support mechanisms, and briefly discusses the likely characteristics of the deposited sediments. Density flow, or more commonly known as submarine mass movement or submarine landslide, is the process of soil movement, caused by current, gravity etc., within a fluid. Mulder and Alexander (2001) divided the density flows into two categories: cohesive and non-cohesive (frictional) density flow. Cohesive density flows are divided into debris flow and mud flow based on the sediment size sorting. Mud flow deposits have less than 5% gravel by volume and a ratio of mud to sand of more than 1:1. It can transport little or no coarse sediments and may transport isolated large blocks. Debris flow consists of more poorly sorted sediments with greater than 5% gravel with variable sand proportion and may transport boulder-sized clasts of soft sediments or rock and very large rafts or olistoliths.

Classification of frictional flows are not described here, and readers can refer to Mulder and Alexander (2001) for more details as it is not the interest of this study. The main focus of this study is to model the glide block and out-runner block impact on offshore pipelines. Mulder and Alexander (2001) did not discuss the physical properties of a glide block or out runner block. Hence, the terminologies used in this study for glide block and out runner block are discussed below:

- Glide block: an intact cohesive sediment hydroplaning block during early stages of density flow that has not been disintegrated and/or remoulded. It still carries the strength properties of the parent soil mass. Here the term hydroplaning means that when a block of cohesive soil moves downward, a layer of water is trapped under the soil blocks which reduces the shear resistance significantly to downward movement.
- Out-runner block: an intact cohesive sediment block that has departed from the parent density flow during the movement due to hydroplaning and rides freely downstream. It has not been remoulded and still carries the strength properties of the parent soil mass.

The following terminologies are also used in this study to describe the clay at various stages in the experiment.

- Consolidated clay: a large clay block prepared from kaolin clay slurry, and which was consolidated under a given vertical stress in a consolidation box on the laboratory floor. It was used to prepare the clay blocks and clay square for the experiments.
- Clay block: an intact block of kaolin clay used to model the glide block and out-runner block impact. It was prepared from the consolidated clay. During the centrifuge test, this block of clay was allowed to consolidate under its self weight again. It was used to conduct the T-bar and the impact test.
- Clay square: an intact block of kaolin clay used to monitor the progress of consolidation during the centrifuge tests and to determine the moisture content that represents the clay block. It was located inside an aluminum square tube. This clay was prepared from the consolidated clay.

2.2 Submarine Landslide

Submarine landslides and their effects are the interest of many researchers of a very wide range of background. Various classification systems of submarine landslides have been proposed in the past. The Technical Committee on Landslides (TC-11) of the International Society for Soil Mechanics and Geotechnical Engineering (ISSMGE) has developed a classification chart, as shown in Figure 2.1. The "slide" is the interest of this study.

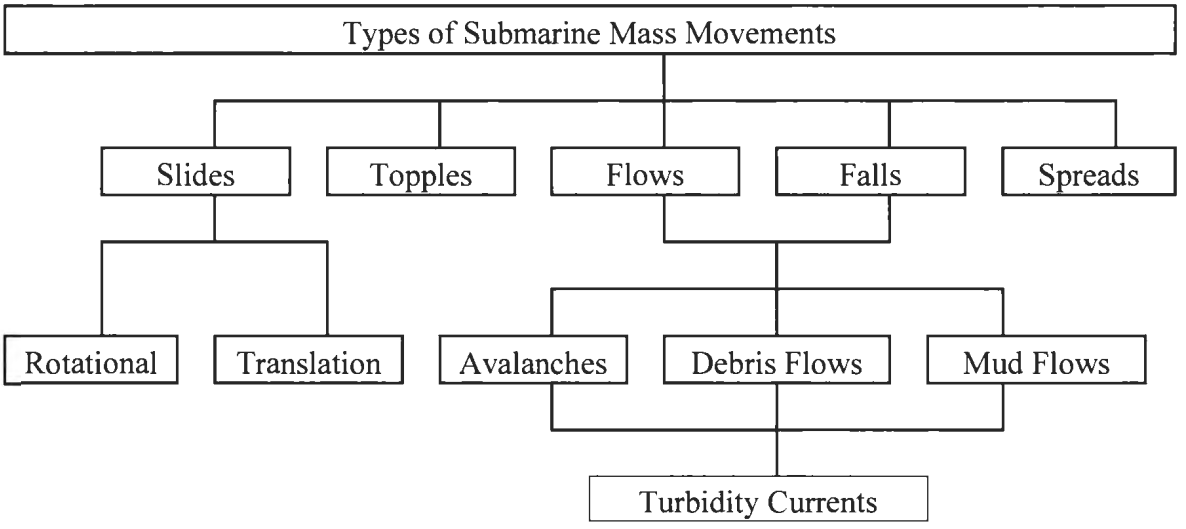

Figure 2.1: Classification of submarine mass movements proposed by the ISSMGE Technical Committee on Landslide (TC11) (Locat and Lee, 2000).

2.2.1 Triggering Mechanisms

There are many factors that have been suggested in the past contributing to the initiation of submarine landslides, as shown in Table 2.1. Interested readers are referred to Masson et al. (2006) for further details on Table 2.1. These triggering factors can occur within a timescale of minutes or days (e.g., vibration due to earthquakes or construction) to a timescale of tens to hundreds of thousands of years (e.g., climate

change). These factors are also divided into two types: those related to the geological characteristics of the landslide material (e.g., overpressure due to dissolving of gas hydrates) and those driven by transient external events (e.g., earthquakes).

Table 2.1: Factors contributing to the initiation of submarine landslides (Note that more than one factor may contribute to a single landslide event) (Masson et al., 2006).

Historically Documented	**Examples**
Earthquakes	Grand Banks
Hurricanes or cyclic loading	Mississippi Delta
Loading or over steepening of slopes	Nice, Canary Islands
Underconsolidation (overpressure)	Mississippi Delta
Rainfall (where landslides have a subaerial extension)	Norway, Hawaii
Slope parallel weak layers in bedded sequences	East coast US, Storegga, West Africa
Gas hydrate dissociation east coast	US, Storegga
Sea-level change	Madeira Abyssal Plain
Volcanic activity	Hawaii, Canaries

2.2.2 Failure of Submarine Landslide

A very wide variety of soil could be found in seabed. The main focus of this study is to model submarine landslides consist of cohesive clay material. The failure of a slope is first initiated by one or combined effects of a number of triggering factors listed in Table 2.1. Once the failure is occurred, the failed soil mass gets detached and can travel a long distance. If it travels a long distance, the materials within the detached soil mass may be broken down into small pieces by hydrodynamic action and/or the shear resistance between seabed and sliding soil mass. Eventually, the sliding soil mass may

turn into a debris flow, and the end result will be a turbidity current. These sequences are schematically shown in Figure 2.2.

However, it is noted here that some slides can travel a long distance (hundreds of kilometres) without noticeable transformation into turbidity currents, while others transform entirely into turbidity currents after traveling a short distance from its source (Masson et al., 2006). This is because the mechanism for turning into flow is not well understood, but at least one factor is likely to be the initial density state of the landslide. If the sediment is less dense than an appropriate steady state condition the sediment appears to be more likely to flow than the one that is denser than the steady state. The ability to flow may also be related to the amount of energy transferred to the failing sediment during the failure event (Locat and Lee, 2000).

The failure of slope and subsequent downward movement also causes a change in shear strength (or mobilized shear stress) to several orders of magnitude. Boukpeti et al. (2012) shows the variation of soil properties at different stage of the slide (Figure 2.2). As shown in this figure there is a wide range of variation of soil shear strength and slide velocity. These should be considered in estimation of drag force on pipelines, which is the interest of the present study.

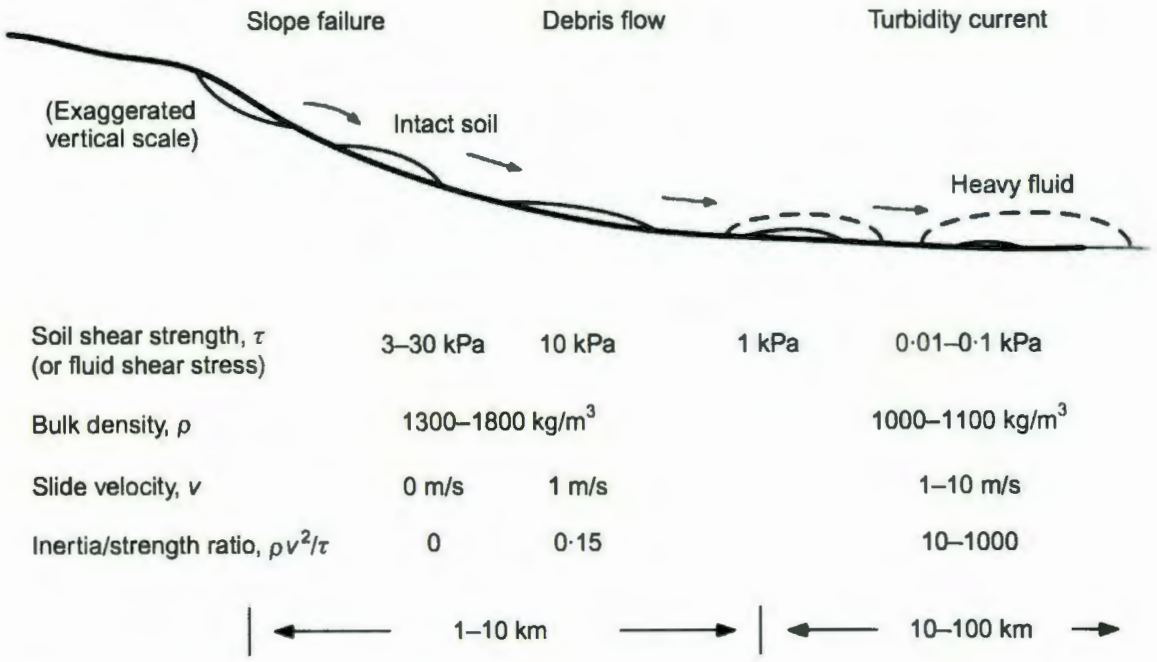

Figure 2.2: Schematic diagram of key submarine slide characteristics (Boukpeti et al., 2012).

Submarine landslides may involve in a larger volume of material and travel a longer distance at a lower slope than subaerial landslides. This long distance at a low slope could be explained by hydroplane and/or a thin layer of lubricant between the soil and seabed (Blasio et al., 2006, Harbitz et al., 2003, Ilstad et al., 2004, Mohrig et al., 1998).

2.2.3 Case Studies

Because of this hydroplaning phenomena, out-runner blocks can travel the same distance as debris flow, or even further. For example, the Finneidfjord slide occurred in 1996 in northern Norway which killed four people. The slide was a combined submarine/subaerial, retrogressive clay slide which was initiated along a weak layer due to excess pore pressure generated from weather conditions and human activities. The

slide mobilized 1 million cubic metres of sediment and the majority of the material did not travel more than three hundred metres. However, the out-runner blocks, as shown at the bottom left corner of Figure 2.3, were deposited nearly 100 m further than the deposition from the debris flow (Longva et al., 2003).

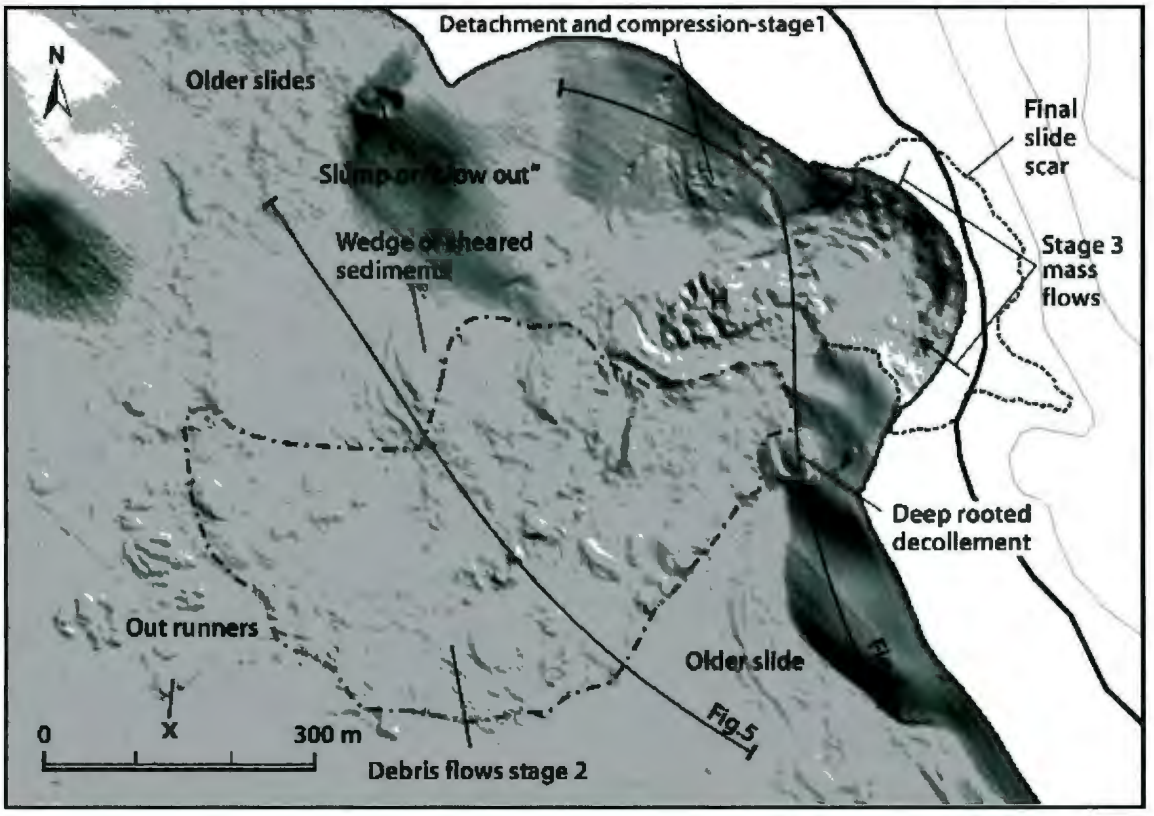

Figure 2.3: Bathymetry of the 1996 Finneidfjord slide (Longva et al., 2003).

One of the most well documented submarine landslides in Canada is the Grand Bank slide which occurred in 1929 that brought attention to many researchers involved in offshore development programs. The submarine landslide mobilized 200 km^3 of sediment which was initiated by an earthquake magnitude of 7.2 on the Richter Scale, and generated a tsunami that killed 28 people. The tsunami generated had amplitudes

ranging from 3–8 m and runup measured up to 13 m along the coast of the Burin Peninsula in Newfoundland. Tsunami waves were observed along other parts of the Atlantic coast of Canada and the United States. The landslide was transformed into turbidity current and traveled up to 1,000 km at a speed ranged from 16 to 28 m/s (60 – 100 km/h), and damaged 12 telegraphic cables along its path (Fine et al., 2005).

2.3 Estimating Drag Forces on Offshore Pipelines

When a failed soil mass travels downward, it can create a significant force on offshore structures, such as pipelines or piles that is in its pathway. Therefore, the estimation of drag force is one of the key design parameters for these types of offshore structures. The failure of offshore pipelines may have a big impact in the economy and the environment.

As the offshore oil and gas development activities are moving into deeper water, there is a need to better assess and quantify the risk associated with geohazards. As mentioned before, the failed soil mass could be at different states — it might behave as soil when it has the original soil properties to fluid where it completely mixed with water. Therefore, the failed soil block might impact the pipeline as a soil block or as fluid. The available methods to estimate the drag force on pipelines and piles can be divided into two approaches: (i) geotechnical approach and (ii) fluid dynamics approach. In the geotechnical approach, the drag force is directly related to the undrained shear strength of soil, which is in a function of rate of shearing. Logarithmic or power-law functions are typically used to include the effect of the rate of shear. The fluid dynamics approach considers the soil as a fully fluidized material and applies the fluid mechanics principles.

The geotechnical approach is more suitable when the moving soil has not been remoulded or fluidized and still carries the soil strength as the parent material, while the fluid dynamics approach is more suitable when the moving soil has been remoulded or fluidized, and has a very low soil strength.

The main interest of this thesis is to develop a relationship to determine the drag force it generates from a glide block or out-runner block onto a suspended pipeline. A glide block and out-runner block is an intact block of soil that carries its parent slide material of minimum disturbances, and hence the geotechnical approach is used in this thesis. Readers are refer to other studies, for example Pazwash and Robertson, (1975) or Zakeri et al. (2008, 2009a, 2009b, 2009c), for more details on the fluid dynamic approach.

Geotechnical approach directly relates the drag force acting on a structure (e.g., pipeline or pile) to the shear strength of the moving soil. A typical equation for the drag force on a structure has the form of:

$$F_D = k \cdot s_u \cdot A \tag{2.1}$$

or in the form of drag force per unit length:

$$f_d = k \cdot s_u \cdot D \tag{2.2}$$

where k is the drag force coefficient, s_u is the undrained shear strength of soil, A is the projected area, and D is the pipe diameter. The drag force coefficient, k, in Equation 2.1 has been determined by several authors either experimentally or based on field data and can be further divided into two groups: (i) Conventional approach and (ii) Strain-rate dependent approach.

2.3.1 Conventional Approach

In the conventional approach, authors have selected a constant k value for Equation 2.1 based on the conventional shallow foundation bearing capacity analysis to determine the drag force generated from a moving soil. It is suitable when the velocity of moving soil is fairly low.

2.3.1.1 Soil and pipe interaction

Demars (1978) proposed an empirical approach to determine the drag force generated by a moving soil. He analyzed the pipeline failure from field data collected between 1971 and 1975 in the Gulf of Mexico. Over 125 failures were recorded during that period, and about 20% of the failures were caused by moving sediment. For the purpose of this analysis, shear and bending of the pipe in the slide zone was neglected. The pipe was initially resting at an average angle, ϕ, to the bottom contours as shown in Figure 2.4a. The force generated from the moving soil on the pipeline was equivalent to a suspended load on a cable and the generated force polygon is shown in Figure 2.4b.

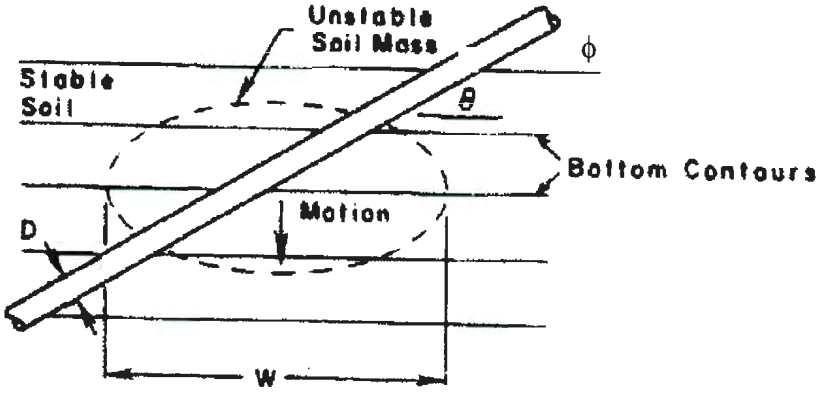

a)

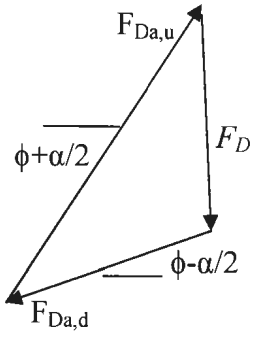

b)

Figure 2.4: Force-deformation conditions for pipeline subjected to soil motion (Demars, 1978).

The force polygon was broken into the drag force, upslope tension, $F_{Da,u}$, and downslope tension, $F_{Da,d}$, components, and its initial angle, and final deflection angle, α, after soil motion. The drag force, F_D, generated by the moving soil mass was calculated by using Equation 2.1, with k equivalent to the bearing capacity factor, N_c of shallow foundation. The upslope tension, $F_{Da,u}$, is the largest and it is a function of its slack of the pipeline and the pipeline orientation with the moving slide.

It was concluded that tension within the buried pipeline orientated parallel to the bottom contour ($\phi = 0°$) is the greatest, and the least when it is orientated along the axis of the moving sediment ($\phi = 90°$). Tension also decreases if there are slacks within the line. As the burial depth increases, the force will increase, since soil strength and bearing capacity is depth dependent, and it may worsen the condition.

Swanson and Jones (1982) studied the effects of down slope movement of soil on pipelines in the Mississippi Delta. The problem has been broken down into two slide regions (i.e., within and outside the slide, Figure 2.5). The generated force from the moving soil onto a pipe has two components; namely lateral and axial forces. The slide is indicated by a width, W, and the angle between the longitudinal axis of the pipeline and direction of the slide,ϕ. In Figure 2.5, the slide region is shown by the area between points 2 and 3, while the outside of the slide regions are shown by the areas between the points 1 and 2 in the left and 3 and 4 in the right. For simplicity, dynamic effects during the slide and bending stiffness were ignored in the calculations.

For the pipeline section located within the slide (i.e., between points 2 and 3), it was assumed that the slide has covered the pipeline. The lateral force per unit length, f_d, can be calculated by Equation 2.2 with a k value of 10. This value was based on experimental results from relative small movement of piles into stationary soils. A parametric study was also performed. The parameters of interest were soil strength, outer diameter of the pipeline, wall thickness, operating conditions, and slide angle. The computed results suggest that some slack in the pipeline, increase of wall thickness, burial depth prior to the slide event, and smaller pipe diameters reduce the likelihood of

failure of the pipeline. On the other hand, high operating pressure increase the likelihood of failure. Finally, Swanson and Jones (1982) stated that pipeline will experience the least stress when the slide is moving in the lateral direction, opposite of what Demars (1978) have suggested. Swanson and Jones (1982) explained that Demars (1978) oversimplified his method and has led him to predict the opposite effects of the slide angle.

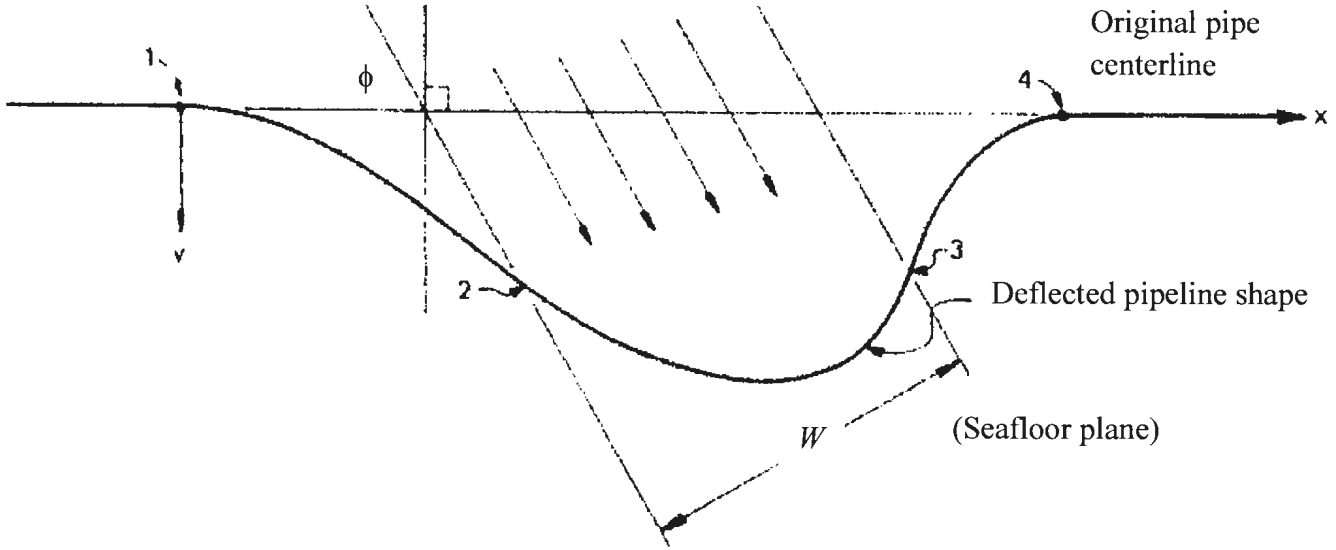

Figure 2.5: Mudslide geometry description (Swanson and Jones, 1982).

Bea and Aurora (1983) carried out analysis to optimize the layout of two steel crude-oil pipelines that may interact with moving soil. Table 2.2 shows the geometry and soil conditions used in the study. They have conducted the analysis for both fast and slow moving soil scenarios. For the fast moving soil scenario, they have adapted the fluid dynamics approach to estimate the forces generated on a pipeline for an impact speed of 0.3 to 1.2 m/s. For the slow moving cases (60 to 100 m/year, which is equivalent to 1.90×10^{-6} to 3.17×10^{-6} m/s), they have adapted the geotechnical approach. Only the geotechnical approach is reviewed here as that is the interest of this study.

Table 2.2: Pipeline properties (Bea and Aurora, 1983).

Pipeline Properties	**Pipe 1**	**Pipe 2**
Outer Diameter (mm)	320	320
Type of Steel	X-52	X-42
Wall Thickness (mm)	10	1.3
Concrete Weight Coating (mm)	38	N/A
Relative density of the empty pipe with respect to seawater	1.33	1.16
Depth of Water (m)	< 60	> 60
Cover	buried	unburied

The authors used the methods produced by Audibert et al. (1979). The generated force from the moving slide was broken into axial and lateral components. The lateral force component per unit length for the unburied pipeline was:

$$f_d = B(f_b - f_v) \qquad 2.3$$

where B is the coefficient of lateral stability, f_b is the buoyant force of pipeline per unit length, and f_v is the hydrodynamic lift force per unit length. Equation 2.2 was used for buried pipeline with a k-value equivalent to the bearing capacity in the horizontal

direction. They concluded that for a pipeline to withstand in a moving soil of 150 m wide, the pipeline should not be buried or buried across an unstable zone where the undrained shear strength is 4 kPa or greater at the surface. Furthermore, if the undrained shear strength of the soil in the unstable zone is between 1.0 kPa and 2.4 kPa, the stresses induced in the buried pipeline are likely to be less than the pipe yield stress for the design depths of burial.

2.3.1.2 Drag force from soil/pile interaction

In the past the drag coefficients were also obtained from soil/pile interaction as it is conceptually very similar to the soil/pipe interaction events. Therefore, in the following sections some studies on soil/pile interaction is described.

Towhata and Al-Hussaini (1988) conducted physical model experiments to simulate mudflow around a vertical column. The experiment setup is shown in Figure 2.6. The tests were conducted in a model tank filled with clay slurry. Table 2.3 shows further information about test conditions and soil properties. An iron model column was pulled across a tank filled with Bangkok clay at different velocities, depths and moisture contents.

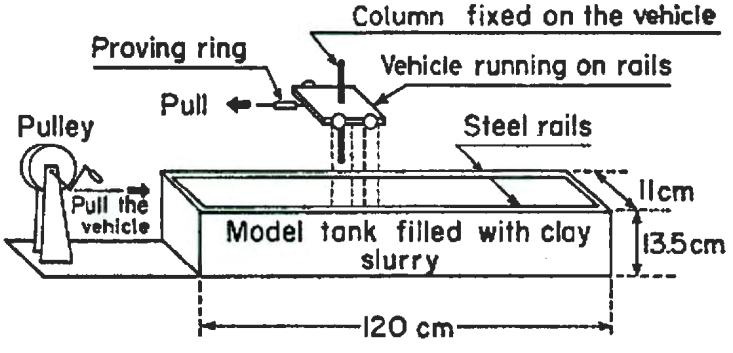

Figure 2.6: Experimental setup (Towhata and Al-Hussaini, 1988).

Table 2.3: Test condition and soil parameters (Towhata and Al-Hussaini, 1988).

Parameters	**Values**
Pipe diameter (mm)	4.7 and 9.5
Velocity, V (mm/s)	10 to 120
Column embedment (mm)	4 to 8
Moisture content (%)	90 to 150

The authors verified that the generated drag force increases with speed, and projected area of the pile (pile diameter and embedment), but decreases with moisture content as shown in Figure 2.7. The generated drag force increases linearly with diameter and length, (Figure 2.7a and b). The effects of velocity and moisture content are shown in Figure 2.7c and d. In the fluid dynamics approach, the velocity term is squared, that means the drag force versus velocity curve should be concaved upward. However, the drag force versus velocity curves obtained in their experiments (Figure 2.7c) is concaved downward. Therefore, the author suggested that the fluid-dynamic approach should be used with caution for estimating drag force.

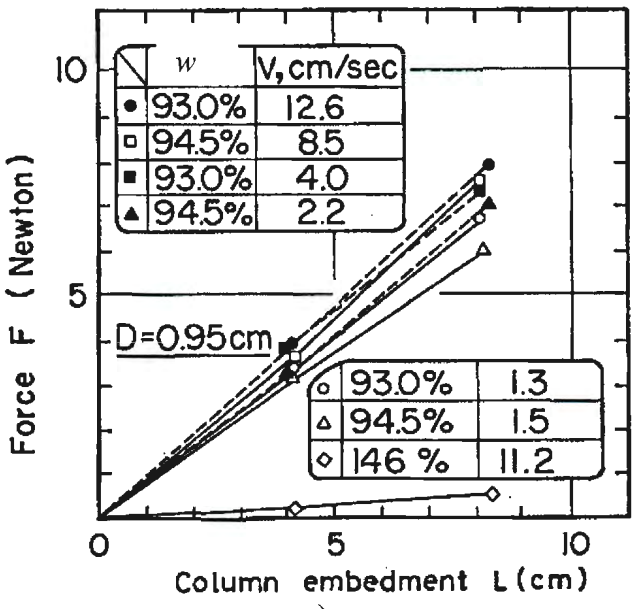
w
V, cm/sec
93.0% 12.6
94.5% 8.5
93.0% 4.0
94.5% 2.2
D=0.95cm
93.0% 1.3
94.5% 1.5
146 % 11.2
Force F (Newton)
Column embedment L (cm)
0
5
10

a)

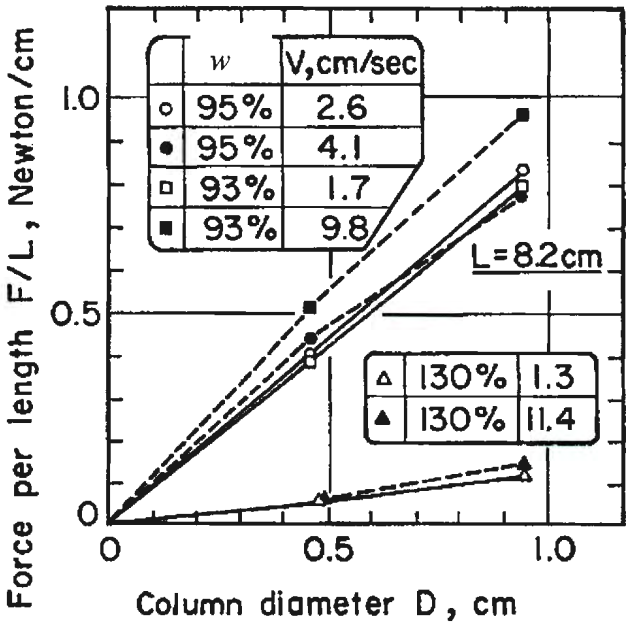
w
V, cm/sec
95% 2.6
95% 4.1
93% 1.7
93% 9.8
L=8.2cm
130% 1.3
130% 11.4
Force per length F/L, Newton/cm
Column diameter D, cm
0
0.5
1.0

b)

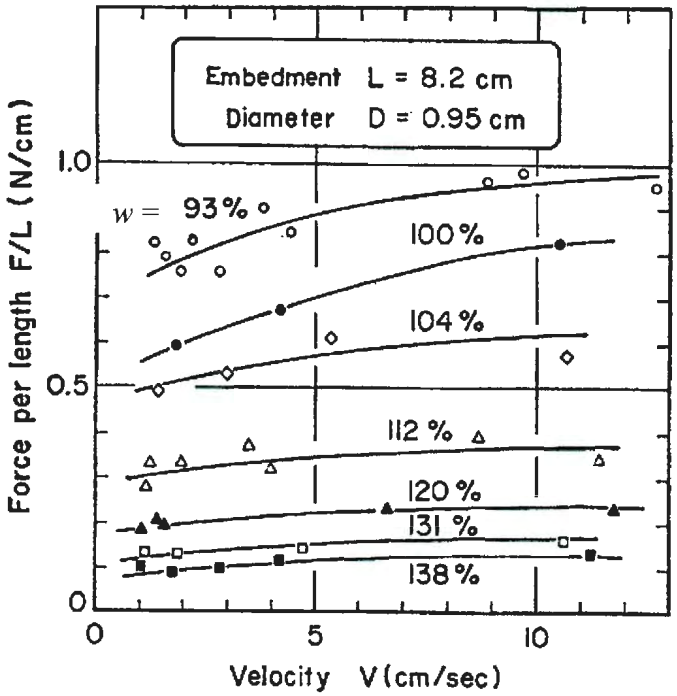

c)

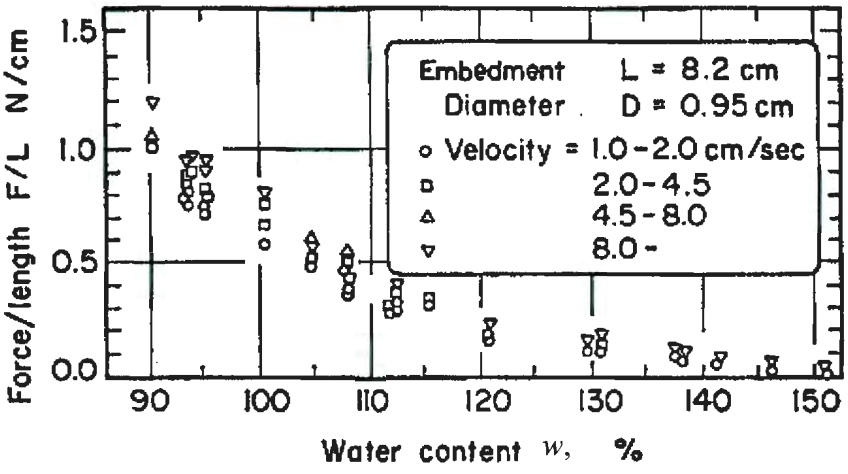

d)

Figure 2.7: Drag force on vertical column (Towhata and Al-Hussaini, 1988): a) effect of column embedment, b) effect of column diameter, c) effect of velocity, and d) effect of moisture content.

Using Equation 2.1, the values of k were back calculated and it ranged from 12 to 20, as shown in Figure 2.8. The authors suggested a mean value of 16 for practical application.

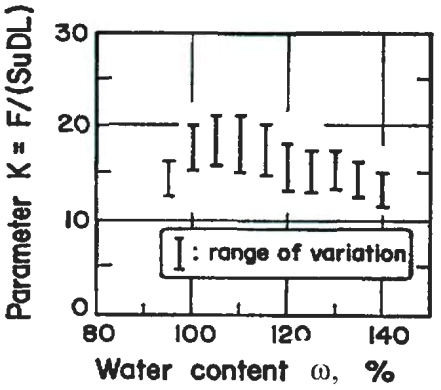

Figure 2.8: k values plotted against water content of slurry (Towhata and Al-Hussaini, 1988).

2.3.2 Strain-Rate Dependent Approach

Towhata and Al-Hussaini (1988) show that the drag force increases with increase in velocity of model pile. In fact when the velocity of the pile is increased the rate of shearing the soil increased. That means the drag force is related to shear strain rate.

The strain-rate effects on undrained shear strength of soil have been investigated in the past by a number of researchers. Bjerrum (1972) conducted triaxial compression tests on plastic clay from Drummen, Norway. He concluded that undrained shear strength increases about 10% for every tenfold increase of shear strain rate. Vaid and Campanella (1977) performed a constant rate of strain, creep triaxial tests on undisturbed Haney clay. The test results showed a linear increase in undrained shear strength with the log of strain rate in the higher strain rate region. However, below a certain strain rate, the undrained shear strength is almost constant. This strain rate can be considered as

"reference strain rate" above which undrained shear strength is rate dependent. Nakase and Kamei (1986) investigated the influence on strain rate on consolidated cohesive soil on triaxial compression and extension tests. Prapaharan et al. (1989) compiled some of these test results and plotted as Figure 2.9. The vertical axis in this figure shows the undrained shear strength normalized by undrained shear strength at shear strain rate of 0.01%.

Kulhawy and Mayne (1990) also showed similar trend with 209 triaxial compression test results on 26 clays, (Figure 2.10). Based on these test results the reference rate of 1%/hour was suggested. The undrained shear strength for other strain rate can be calculated using the following equation:

$$\frac{s_u}{s_u \; at \; 1\%/hr} = 1.0 + 0.1 \cdot \log \dot{\gamma} \qquad 2.4$$

Based on above discussion it is clear that the undrained shear strength of clay increases with shear strain rate. In the modeling of drag force, the velocity of the soil around pipelines or pile is related to shear strain rate. The higher the velocity implies a higher the rate of shearing, and because of that, the drag force increases with velocity. One way to include this effect of strain rate is to define the drag coefficient, k in Equation 2.1 as a function of strain rate.

It is to be noted here that the strain rates typically used in triaxial tests are much smaller than it is encountered in a typical landslide in which the failed soil mass might move at a velocity of more than 1m/s. In the following sections some studies where higher velocity was used are discussed.

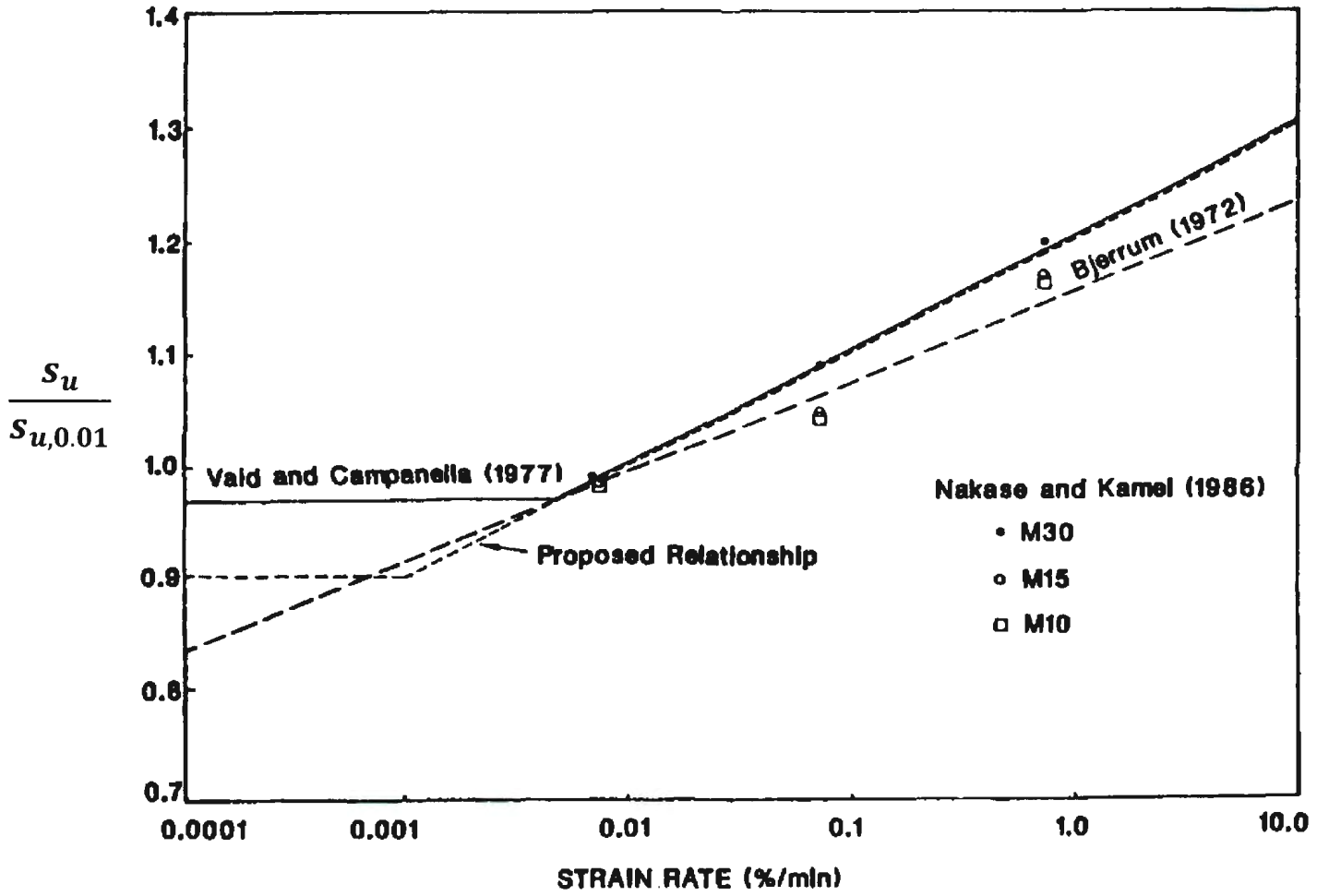

Figure 2.9: Normalized shear strength versus strain rate from triaxial tests (Prapaharan et al., 1989).

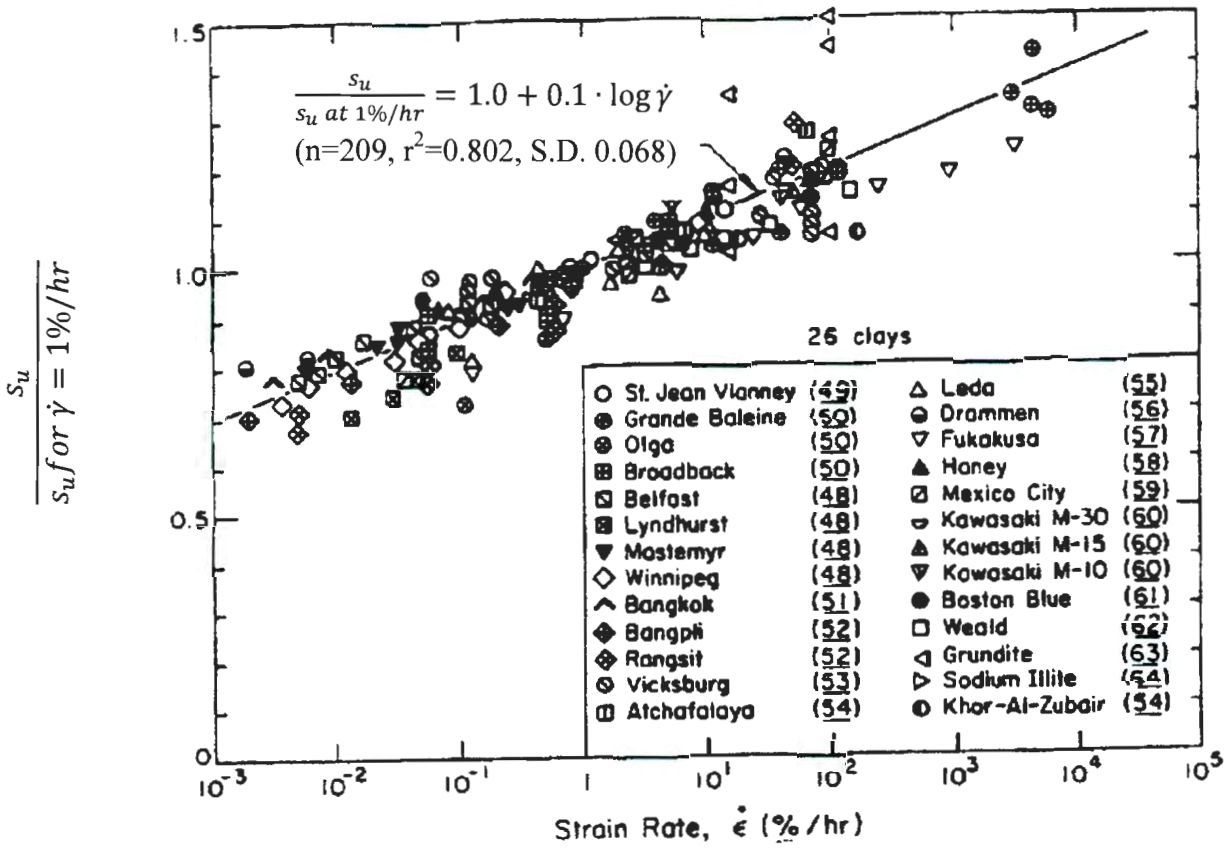

Figure 2.10: Strain rate influence on s_u (Kulhawy and Mayne, 1990).

2.3.2.1 Soil/pipe interaction at large velocity

Georgiadis (1991) conducted a literature survey to determine the values for the drag force coefficient, k, proposed by different authors. He found a wide a range of different values of k. He concluded that the main reason of this difference is that the drag force is dependent on the velocity of the moving soil mass, which was not taken into account in the conventional approach. To prove this concept, eight shear box tests were performed on clay samples using different shear rates in an undrained condition. The shear box tests showed that undrained shear strength of clay increases with increasing shear speed.

Further, he conducted nine model tests by pushing a 10.6 mm diameter steel rod through the clay at various velocities ranged from 1 to 90 mm/min, corresponding to a shear strain rate ranged from 1.6×10^{-6} to 1.4×10^{-4} 1/s, see Equation 3.9 for the shear strain rate equation. Based on experimental results, he proposed the following power-law relationship for k- in Equation 2.1.

$$k = k_r \cdot \left(\frac{V}{V_r}\right)^n \qquad 2.5$$

where, k is the drag coefficient of the pipe (Equation 2.1), V is the velocity of the pipe, n is the viscosity coefficient obtained from the shear box tests, and k_r and V_r is the drag force coefficient and velocity at the reference point, respectively. The value for n obtained from the shear box tests was 0.125. The proposed equation matched fairly close with the test data as shown in

Figure 2.11. The k values ranged from 7 to 12 at a speed of 1 mm/min to 90 mm/min, respectively. He also mentioned at a speed of 1 m/s, which is a typical speed for a slide, the k value is 27.

This relationship was also used to compare the test data reported by other researchers (Schapery and Dunlap, 1978, Towhata and Al-Hussaini, 1988) and showed a reasonable agreement as shown in Figure 2.12 and

Figure 2.13.

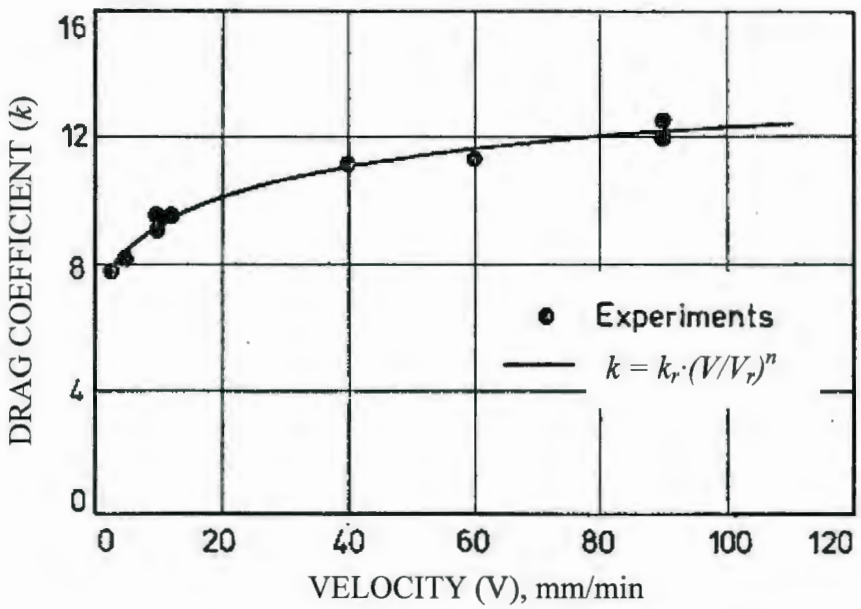

Figure 2.11: Effect of velocity on drag coefficient (Georgiadis, 1991).

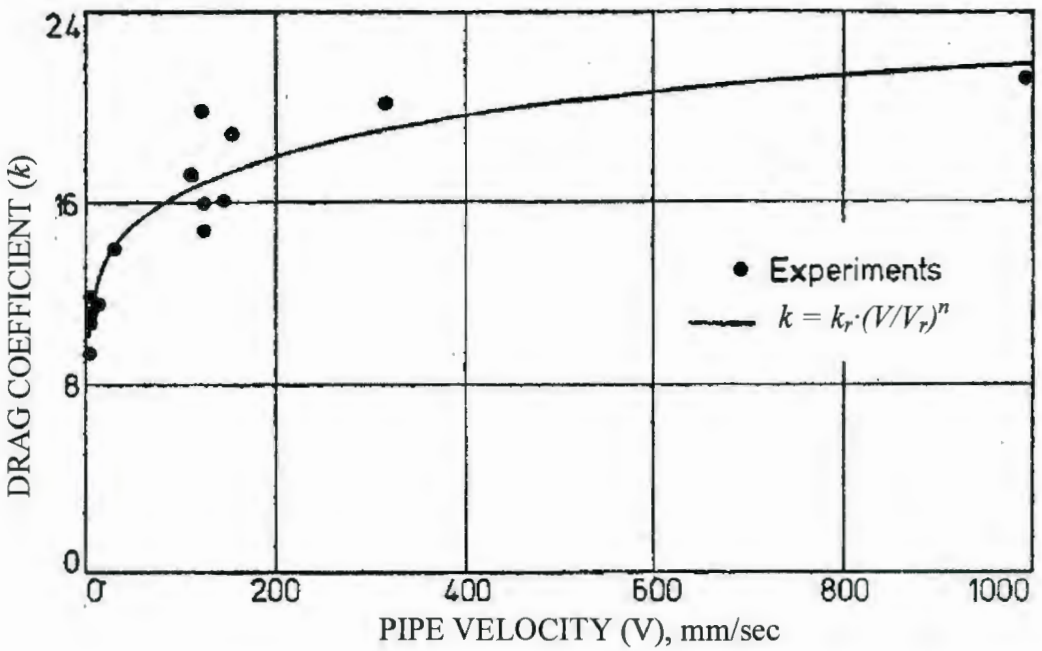

Figure 2.12: Effect of velocity on drag coefficient (experimental results after Schapery and Dunlap (1978)).

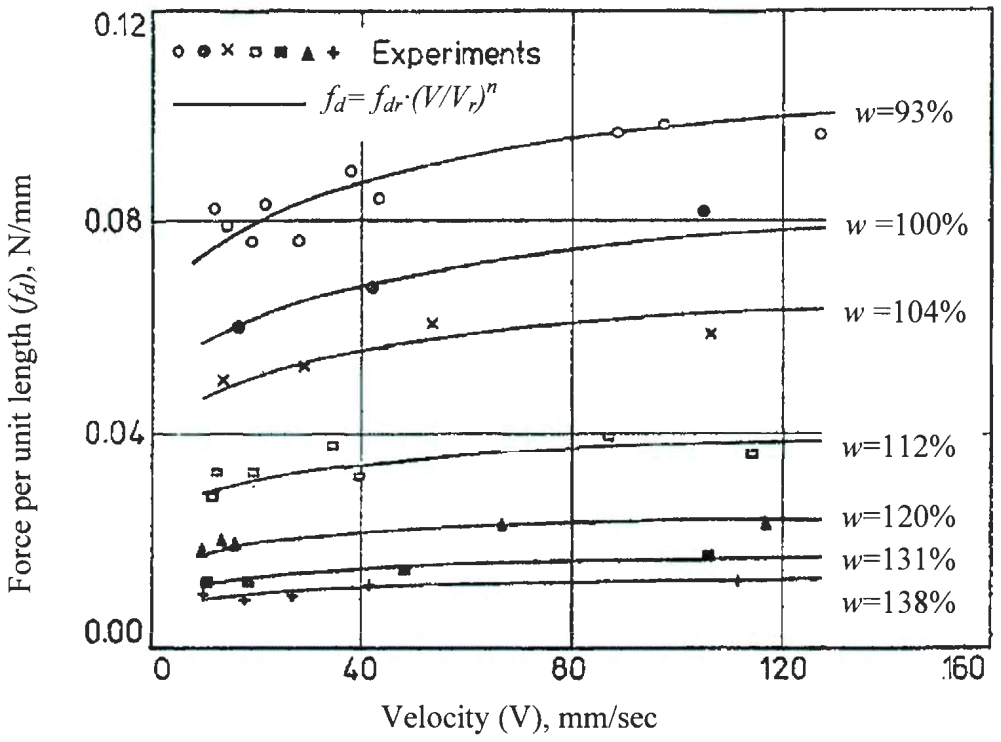

Figure 2.13: Effect of velocity on drag force (experimental results after Towhata and Al-Hussaini (1988)).

2.3.2.2 Soil/pile interaction

Schapery and Dunlap (1978) conducted an experiment in a large shear box containing a pile, (Figure 2.14). Sediment was placed in a rubber bag which fits inside the shear box. Rubber bladders were placed between the rubber bag and the walls of the box and filled with water to pressurize the sediments inside the box to a maximum pressure of 483 kPa (70 psi). The walls were rotated back and forth with a fixed period of 15.7 seconds. A servo-controlled ram was used to move the pile horizontally to a maximum displacement of ± 76.2 mm (± 3") at various frequencies.

Three model pile with 12.7, 24.5, and 38.1 mm (0.5", 1.0", and 1.5") diameters were used to provide information on scaling affects. Additional piles (same diameters

but with different lengths) were used to evaluate end affects, and to measure pore pressures associated with cyclic loading in the sediment adjacent to the pile.

Figure 2.15 shows the first cycle peak drag coefficient, k, with velocity, V, expressed in terms of the pipe diameter, D. Note that the drag coefficient was determined by using Equation 2.1, and the s_u was determined by a vane shear test.

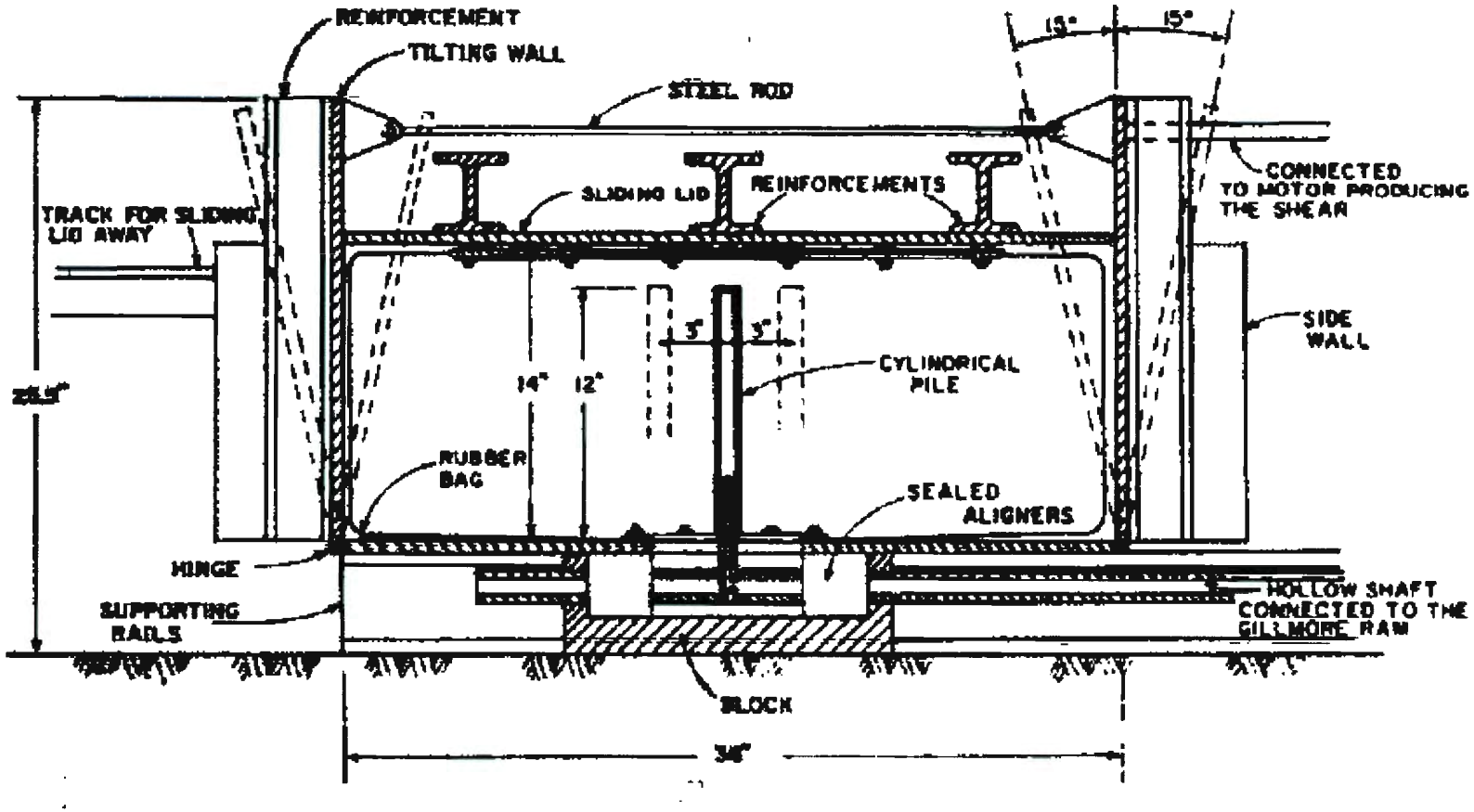

Figure 2.14: Longitudinal section of the shear box (Schapery and Dunlap, 1978).

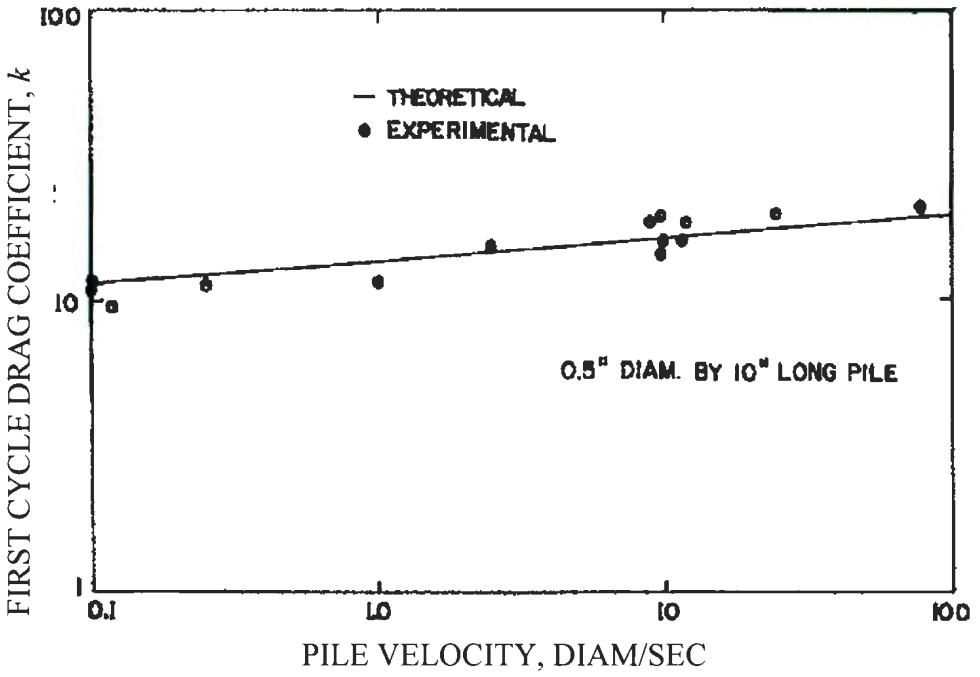

Figure 2.15: The variation of drag coefficient with pile velocity (Schapery and Dunlap, 1978).

The drag coefficients from the experiment were also compared with a theoretical formula based on slip-line model as shown in Equation 2.6, and a reasonably good agreement with the test results.

$$k = (11.42)(125.9 \cdot n_0)^{n_0} \cdot \left(\frac{V}{D}\right)^n \qquad 2.6$$

where n is a dimensionless parameter gained from independent measurements of the shear modulus of the sediment.

However, the authors mentioned that the results should not be used directly to the field situations due to small scale effects.

2.4 Summary

Several authors have proposed mathematical models, based on the geotechnical approach, as shown in Equation 2.1, to estimate the drag force on offshore pipelines generated from a submarine landslide by evaluating the values for the drag force coefficient, k. Table 2.4 summarize the drag coefficient values proposed by previous authors. The undrained shear strength of the soil is strain rate dependent. One of the reasons of this wide variation in the k values is the strain rates or velocities the authors used in their experiments.

Most of the authors conducted their model tests under the velocities lower than the typical velocity of submarine landslide (more than 1 m/s). The tests under highest velocity conducted were done by Towhata and Al-Hussaini (1988), which was 0.126 m/s, to understand pile/soil interaction behaviour.

Based on the literature review presented in this chapter, it has been found that drag coefficient is highly dependent on velocity of the sliding soil block. The model tests conducted in the past are limited to low velocity range. For better estimation of drag force on offshore pipelines, model tests should be conducted for higher velocities as typically observed in submarine landslides. Based on such test results, a better model for k values could be developed, which is the aim of the present study.

Table 2.4: Summary of drag coefficient (k) value/models available in the literature.

Author(s)	**Method of approach**	**Velocity (m/s)**	**Drag force coefficient , k**	**Comments**
Demars (1978)	Conventional	-	-	Bearing capacity factor
Swanson and Jones,(1982)	Conventional	-	10	For buried pipelines within the sliding zone
Bea and Aurora (1983)	Conventional	-	-	For buried pipelines and based on the bearing capacity factor
Towhata and Al-Hussaini (1988)	Conventional	0.01 to 0.12	12 to 20	Suggest 16 for practice
Georgiadis (1991)	Strain-rate dependent	1.67×10^{-5} to 1.50×10^{-3}	7 to 13	
Schapery and Dunlap (1978)	Strain-rate dependent	6.35×10^{-4} to less than 0.635	9 to 21	Velocities were determined from Figure 2.15, and the k values were from Figure 2.12.

Chapter 3

Experimental Program

3.1 Centrifuge Modelling

Geotechnical centrifuge is a well accepted physical modeling technique that has been used successfully to study various geotechnical engineering problems such as the soil/pipeline interaction, bearing capacity of foundations, embankment, and frost heave. A centrifuge is a load frame, and the model is placed at the end of the centrifuge arm that is rotated about the central axis of the centrifuge. During the rotation, the model experiences a higher acceleration in the radial direction than that of Earth's gravity. As the rate of increase in stress of the soil in the radial direction is higher, a small-scale model in the centrifuge can provide a similar stress profile as in a thick layer of soil in the field. That is why centrifuge modelling is widely used in geotechnical engineering.

3.1.1 Principal of Centrifuge Modeling

When a soil model is placed at the end of the centrifuge arm and rotated around the central axis at a radius, r, and an angular velocity of rotation expressed in radian per second, ω, the centrifuge will introduce the model to a radial acceleration of N times the gravity, where $N = r \cdot \omega^2$. When the model and prototype is using the same soil and an radial acceleration of N times Earth's gravity is applied to the model, the vertical stress at depth h_m of the model will be identical to that in the corresponding prototype at depth h_p, where $h_p = N \cdot h_m$ (Taylor, 1995, Yang, 2009), as illustrated in Figure 3.1. This is the basic scaling law of centrifuge modeling.

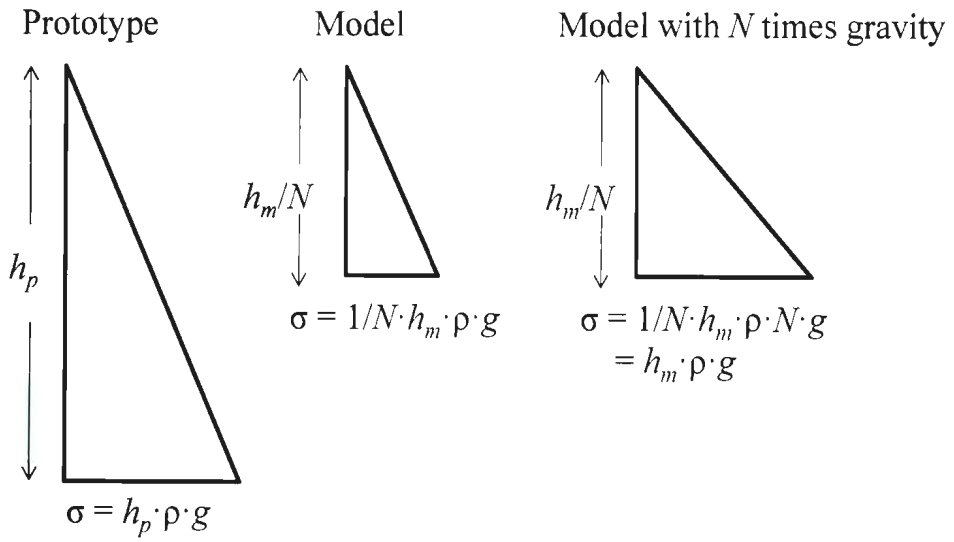

Figure 3.1: Vertical stress distribution in model and prototype.

3.1.1.1 Scaling law

The basic scaling law was derived to ensure that the parameters (e.g., stress, displacement, and velocity) between the model and the corresponding prototype are similar. If an acceleration of N times Earth's gravity (g) is applied to a material of density, ρ, then the vertical stress, σ_v, at depth h_m in the model (using subscript m to represent the model) is given by:

$$\sigma_{vm} = \rho \cdot g \cdot N \cdot h_m \qquad 3.1$$

In the prototype (using the subscript p) is:

$$\sigma_{vp} = \rho \cdot g \cdot h_p \qquad 3.2$$

Thus for $\sigma_{vm} = \sigma_{vp}$, then $h_m = h_p \cdot N^{-1}$ and the scale factor for linear dimension is 1:N (model:prototype). Since the model is a linear scale representation of the prototype, the displacements will also have a scale factor of 1:N, then the strains have a scale factor

of 1:1. So the part of the soil stress-strain curve in the model will be identical to the prototype.

3.1.1.2 Scaling errors

The radial acceleration ($r \cdot \omega^2$) is not linear and therefore it cannot represent the true stress profile of the prototype. However, as shown by Taylor (1995), there is a location were the stress between model and prototype is the same. If the vertical stress in model and prototype are the same at depth, h_i, the effective centrifuge radius for the model, r_e, can be shown as:

$$r_e = r_t + 0.5 \cdot h_i \tag{3.3}$$

where r_t is the radius to the top of the model. A convenient rule for minimising the error in stress distribution is calculated by taking in the relative magnitudes of under and over stress, see Figure 3.2. The ratio, r_u, of the maximum under stress which occurs at model depth $0.5h_i$, to the prototype stress at that depth is:

$$r_u = \frac{h_i}{4 \cdot r_e} \tag{3.4}$$

Similarly, the ratio, r_o, of maximum over stress, which occurs at the base of the model, h_m, to the prototype stress at that depth is:

$$r_o = \frac{h_m - h_i}{2 \cdot r_e} \tag{3.5}$$

Solving the two ratios r_u and r_o gives:

$$h_i = \frac{2}{3 \cdot h_m} \tag{3.6}$$

And so:

$$r_u = r_o = \frac{h_m}{6 \cdot r_e} \tag{3.7}$$

Also, using Equation 3.6:

$$r_e = r_t + \frac{h_m}{3} \tag{3.8}$$

Using this rule, there is exact correspondence between the model and prototype stress at two-thirds model depth, and the effective centrifuge radius should be measured from the central axis to one-third the depth of the model.

For most of the geotechnical centrifuges, h_m/r_e is relatively small and is typically less than 0.2. Therefore, the maximum error in the stress profile is minor and generally less than 3% of the prototype stress.

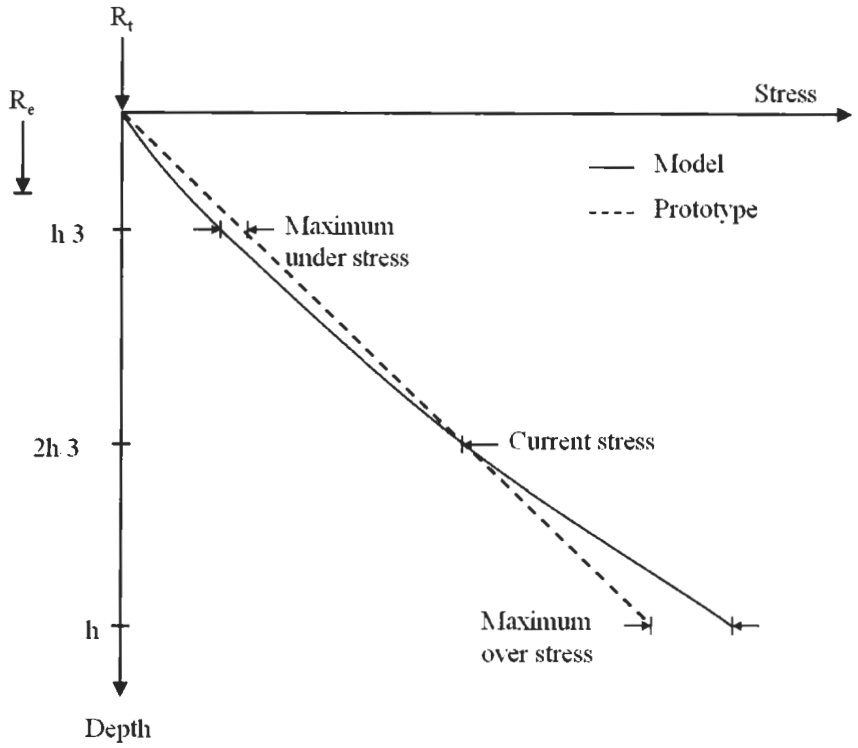

Figure 3.2: Comparison of stress variation with depth in a centrifuge model and its corresponding prototype (Taylor, 1995).

3.1.1.3 Scaling factors

Some basic centrifuge scaling relationships are shown in Table 3.1.

Table 3.1: Some common centrifuge scale factors.

Parameter	Unit	Scale Factor
Acceleration	LT^{-2}	$a_m = N\,a_p$
Length	L	$h_m = 1/N\,h_p$
Stress	$ML^{-1}T^{-2}$	$\sigma_m = \sigma_p$
Force	MLT^{-2}	$F_m = 1/N^2\,F_p$
Velocity	LT^{-1}	$V_m = V_p$
Time – consolidation	T	$t_m = 1/N^2\,t_p$
Strain	-	$\varepsilon_m = \varepsilon_p$
Shear strain rate	T^{-1}	$\dot{\gamma}_m = N\,\dot{\gamma}_p$

Note: Subscript *m* denotes model and *p* denotes prototype.

The current study is related to impacting an intact clay block on a suspended pipeline. The scaling laws that should be considered are the force, soil strength, and the velocity. Instead of using velocity directly, shear strain rate will be used and shear strain rate in the model is N times higher than the prototype. Shear strain rate is defined as (Gaudin et al., 2006):

$$\dot{\gamma} = \frac{V}{D} \qquad 3.9$$

3.2 Experimental Setup

A new experimental setup was developed in this study. The experiments were conducted using the C-CORE Acutronic 680-2 geotechnical centrifuge to generate artificial gravity (radial acceleration) to simulate the model stress level to the prototype. The experimental setup placed in an aluminum strong box and transferred it to the centrifuge. The setup consists of load cells to measure the impact force in both horizontal

and vertical direction, T-bar apparatus to determine the undrained shear strength profile of the model glide or out-runner block, string potentiometer to measure the traveled displacement (used to calculate velocity). Sections below describe the setup in more details.

3.2.1 C-CORE Geotechnical Centrifuge

The Acutronic 680-2 geotechnical centrifuge is contained in a 13.5 m diameter chamber with 0.3 m thick concrete wall, see Figure 3.3 a and b. The centrifuge is located in the C-CORE building in the St. John's campus of Memorial University. The centrifuge includes a swinging platform where models are placed, two parallel steel tubes that connects to the platform, a 20.2 tonne adjustable counterweight, a central drive box and electrical cabinets, pedestal, gear box, motor and drive. The power of the centrifuge is provided by an AC variable speed motor, and main power consumption is the aerodynamic drag within the centrifuge chamber.

The centrifuge has a radius of 5.5 m to the surface of the swinging platform. It has the capacity to generate 200 times of Earth's gravity at a payload of 650 kg. As the payload increase, the output g-levels decrease linearly to a maximum payload of 2,200 kg at a g-level of 100, as shown in Figure 3.3 c. The platform can carry a model up to a dimension of 1.4 m long × 1.1 m wide × 2.1 m high.

a)

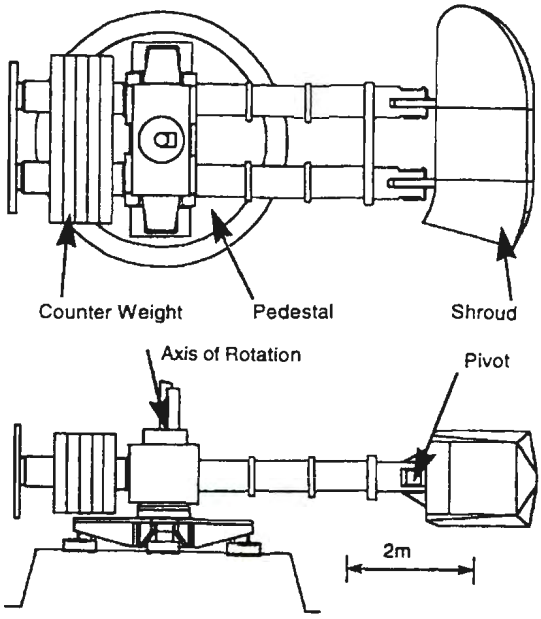

b)

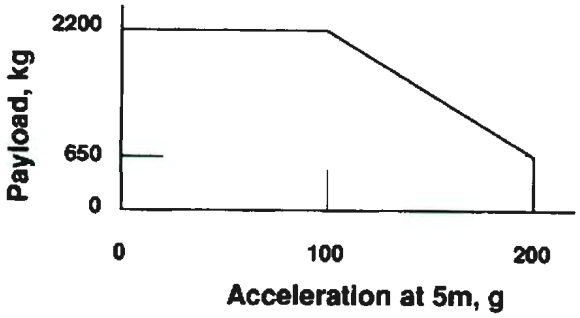

c)

Figure 3.3: a) Geotechnical Centrifuge at C-CORE, b) Schematic view, and c) Payload capacity.

3.2.2 Supporting Equipments

The model and all equipments were placed in or on top of an aluminum strong box (see Figure 3.4). The strong box consisted of an 80 mm lighten wall, and its inner dimension was 1,180 mm long × 940 mm wide × 400 mm high. The empty mass of the strong box was 335 kg. The strongbox was carried by a forklift and loaded onto the centrifuge platform for the tests.

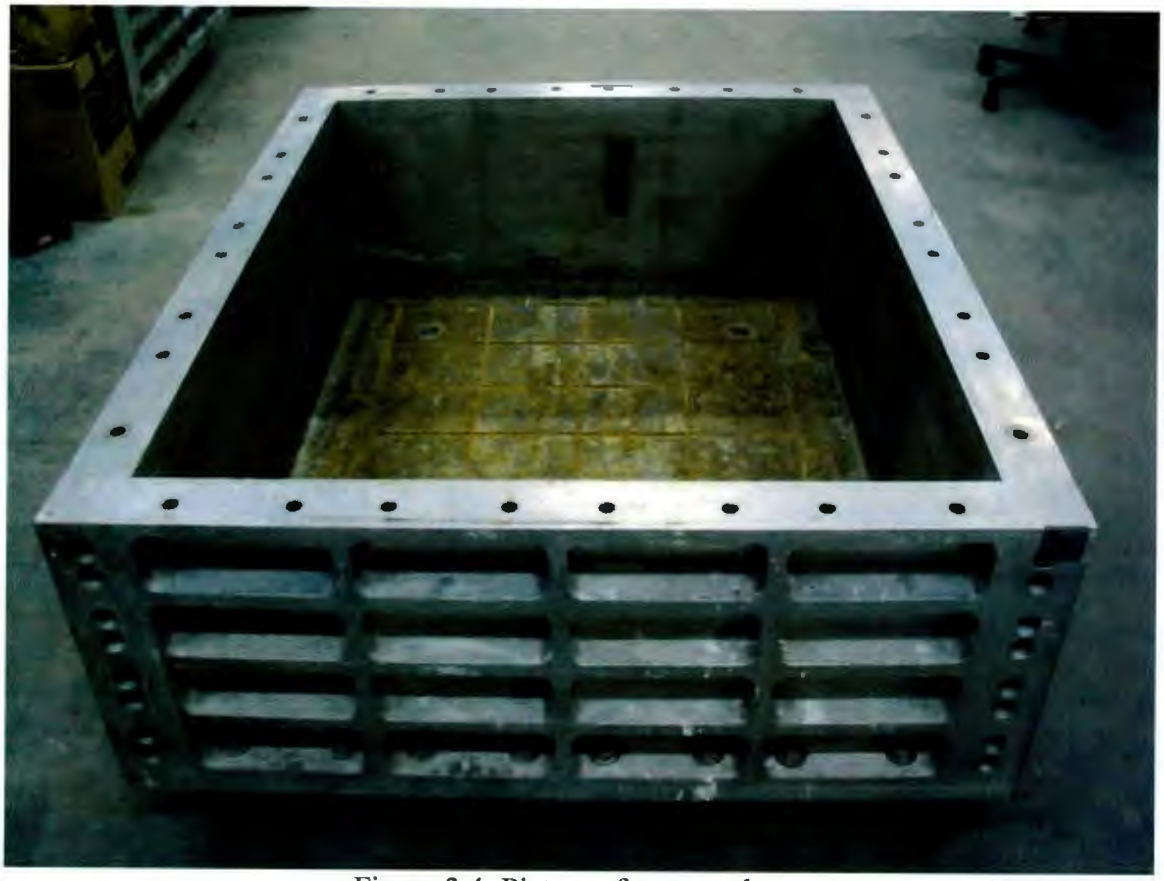

Figure 3.4: Picture of a strong box.

A 1,155 mm long by 935 mm wide by 9.5 mm (3/8") high extrusion steel plate was used as a base plate to transport equipments and instruments in and out of the strong box. The mass of this plate was 80 kg.

A plywood extension (see Figure 3.5) was used to reduce water splashes that may have generated from the moving clay block through the water. The plywood extension has an 80 mm thick wall that fits right on the top of the strong box. Its height was 305 mm (1′) and the mass was 40 kg.

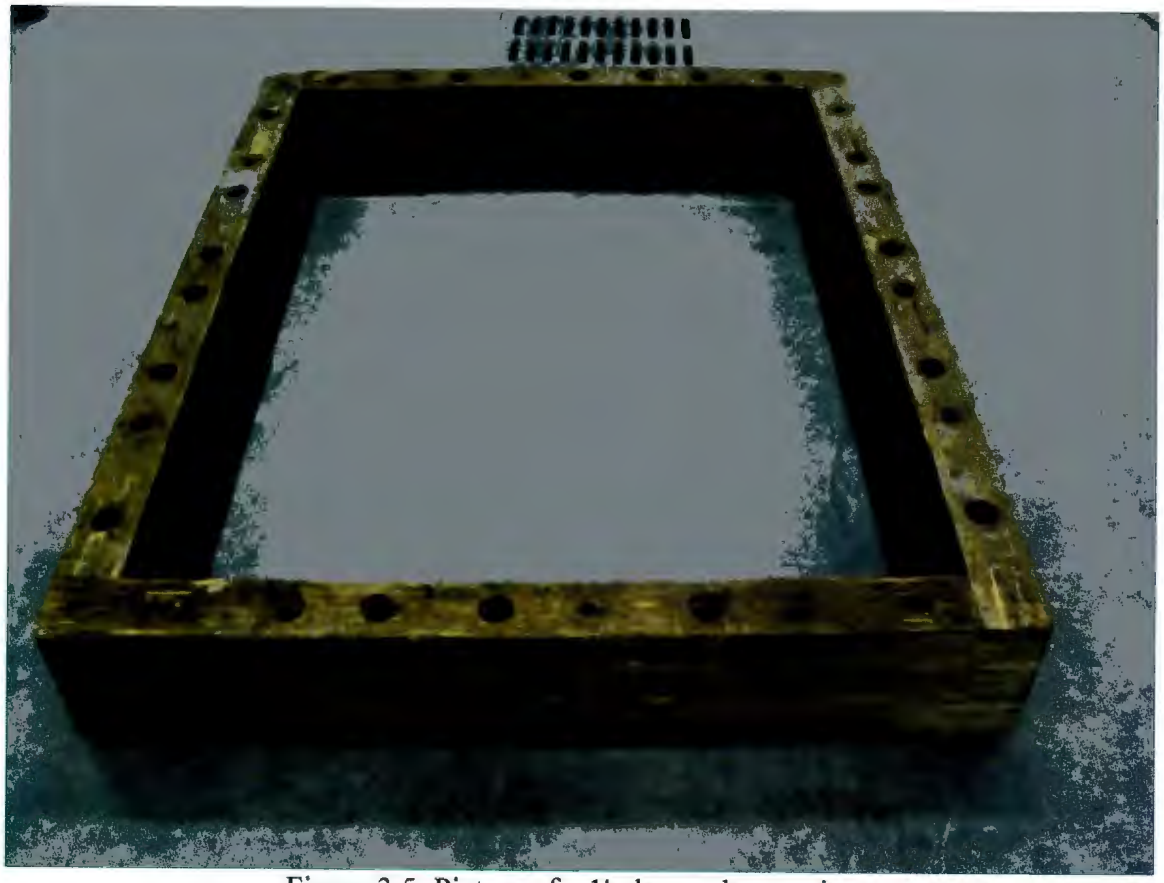

Figure 3.5: Picture of a 1' plywood extension.

Two wide flange aluminum beams measured in 1,340 mm long were placed across the strong box in the longitudinal direction to support instruments that were not

waterproof and/or needed to be on the top, like the vertical actuators. The mass of the two beams were 19 kg.

An aluminum plain strain box was used to conduct the lab-floor consolidation. This plain strain box well be referred to as "consolidation box" and it has an inner dimension of 900 mm long × 300 mm wide × 400 mm high.

3.2.3 Flume and Cart

Located at the middle of the extrusion plate, were two 11.3 mm thick plexiglass that were measured 300 mm high and 1,000 mm long, see Figure 3.6. The isometric view of the flume and cart is shown in Figure 3.7. The plexiglass were aligned longitudinally with the extrusion plate. These plexiglass act as walls, and hereafter it will be referred as "wall". Each wall was attached to its individual 25.4 mm by 25.4 mm by 6.35 mm (1" by 1" by ¼") steel angle, and onto the extrusion plate. There was a 20 mm diameter hole locate near the center of each wall. These holes were used for the model pipes to extend through the walls and connect to the load cells. The space created by the walls was 200 mm and this space will be referred as the "flume."

Inside the flume was a cart made of aluminum. It was used to carry and move the clay block at various velocities. The cart is "L" shaped and measured 6.35 mm (1/4") thick by 200 mm long × 198 mm wide × 150 mm high. The cart was mounted on top of four pillow-block linear ball bearings and was guided by two linear precision shafts with support rails. At the front of the cart was an 11.3 mm thick plexiglass. This plexiglass acted as a gate and will be referred as "gate". The gate was used to contain the clay blocks during centrifuge consolidation and lifted, via a 2.4 mm diameter air craft cable

connected to a vertical actuator, prior moving the clay block. The gate was supported by two 11.5 mm wide by 3 mm deep groves that were cut from each side of the wall.

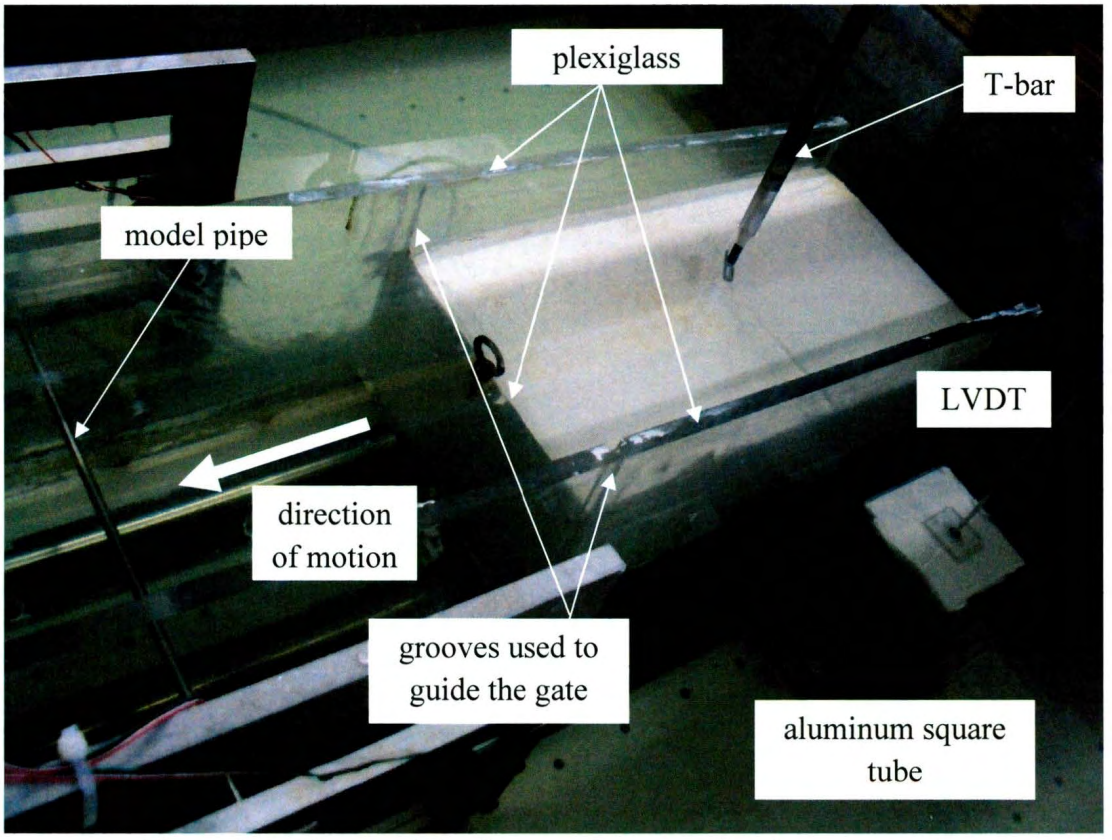

Figure 3.6: Picture of the flume and surrounding instrumentations.

3.2.3.1 Instrumentations in the flume

A limit switch was a safety feature used to stop the servo motor from moving the cart once a magnet, attached to the back of the cart, has past the limit switch. The limit switch was placed inside a plexiglass wall 55 mm upstream from the model pipe.

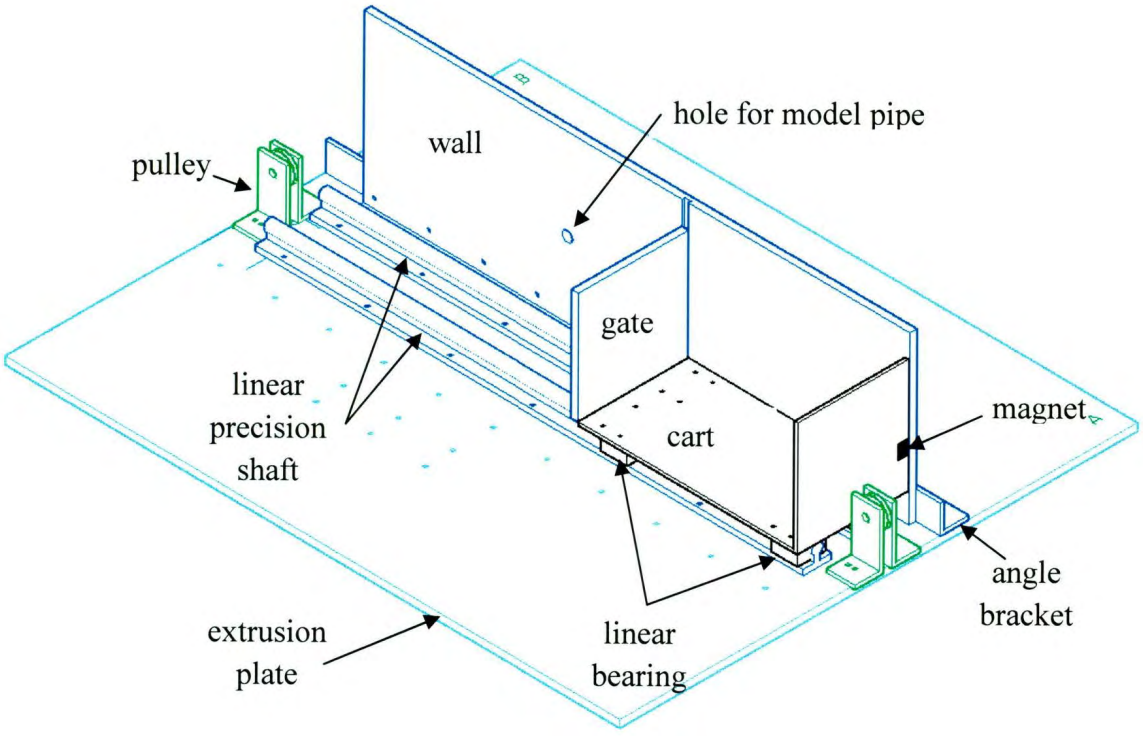

Figure 3.7: Isometric view of the flume and cart. Note that only one wall is displayed for clarity.

3.2.3.2 Instrumentations on the cart

Located to the front of the clay block and above the water, was a Parker BE344JJ servo motor, see Figure 3.8 . It was connected to the cart via a 2.4 mm air craft cable through a pulley. The motor was used to move the cart at various velocities. The motor is capable of generating 4 N·m torque and consumes 1,476 watts at a speed of 3,600 rpm. A 5:1 ratio gear box was attached to the motor.

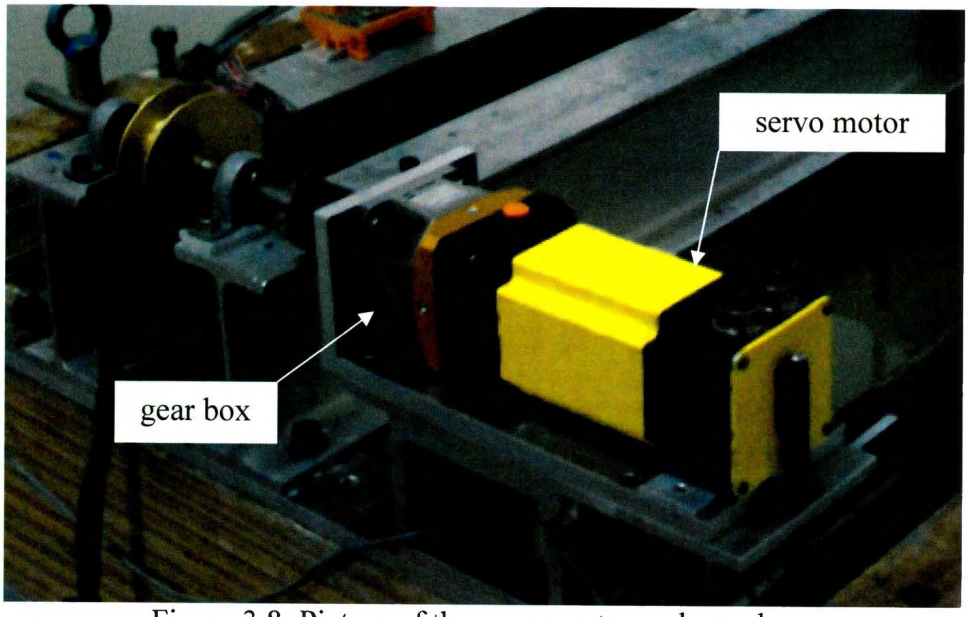

Figure 3.8: Picture of the servo motor and gear box.

Attached to the back of the cart is a magnet, and above the water is a string potentiometer. The magnet was used to trigger the limit switch to stop the servo motor. A string potentiometer is a transducer used to measure displacement using a flexible cable and spring-loaded spool. The spring-loaded spool reduces the slack of the cable in the centrifuge flights.

3.2.4 The Model Pipe

Solid stainless steel rods were used in the experiment to model the pipeline (Figure 3.9 and Figure 3.10). The outer diameters of the model pipes were 6.35 mm and 9.52 mm (1/4″ and 3/8″), and the length was 405 mm. The diameter of the model pipe has been reduced to 6 mm for a length of 40 mm from both ends in order to fit them into the pipe mounts. The model pipes were placed perpendicular to the direction of the moving clay block, with ends extended through the walls, and suspended in the water by the load

cells. The moving clay block interacts only with 200 mm length of the pipe (i.e. the width of the flume).

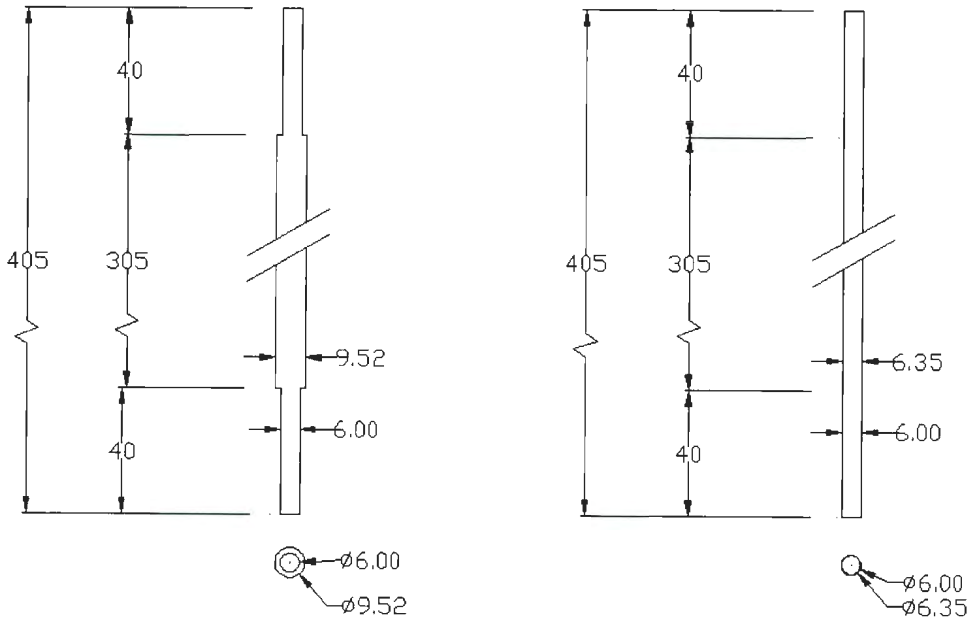

Figure 3.9: Dimensions of model pipes used in experiment (all dimensions are in mm).

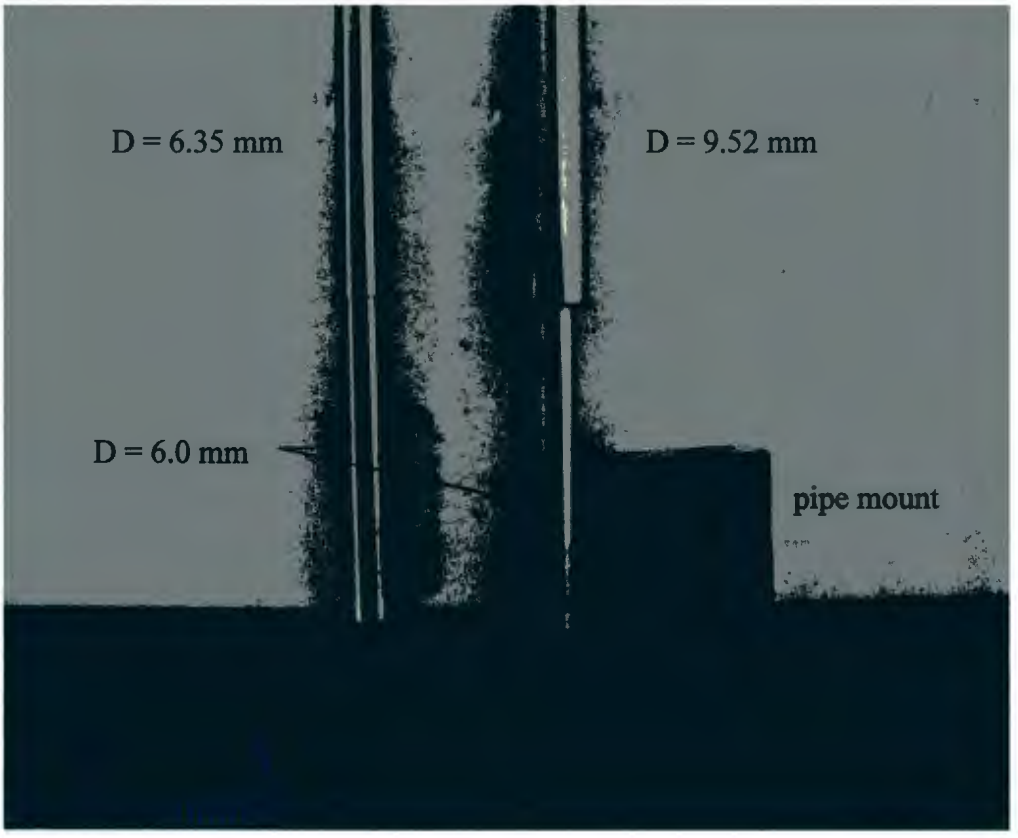

Figure 3.10: Picture of the model pipes and pipe mount.

3.2.4.1 Instrumentations on the model pipes

Figure 3.11 and Figure 3.12 show the load cell arrangement developed in this study. Each end of the pipe was fitted inside of a pipe mount and connected to two load cells. One load cell measured the drag force parallel to the direction of the moving clay blocks, and the other measured the force perpendicular to the direction of the moving clay blocks. Aluminum rods of 3 mm diameter were used to connect the load cells and pipe mounts, and the connections form of a flex link, see Figure 3.11. Verification was conducted to ensure that the load cells do not significantly interfere with each other by pulling the pipe horizontally with a known force, and compare the readings between the

vertical and horizontal load cells, see Appendix. The load cells were connected to two adjustable load cell stands and were connected to the extrusion plate located outside of the flume (Figure 3.12). The load cells were made from 6061 T6 aluminum and the maximum design force was 300 N.

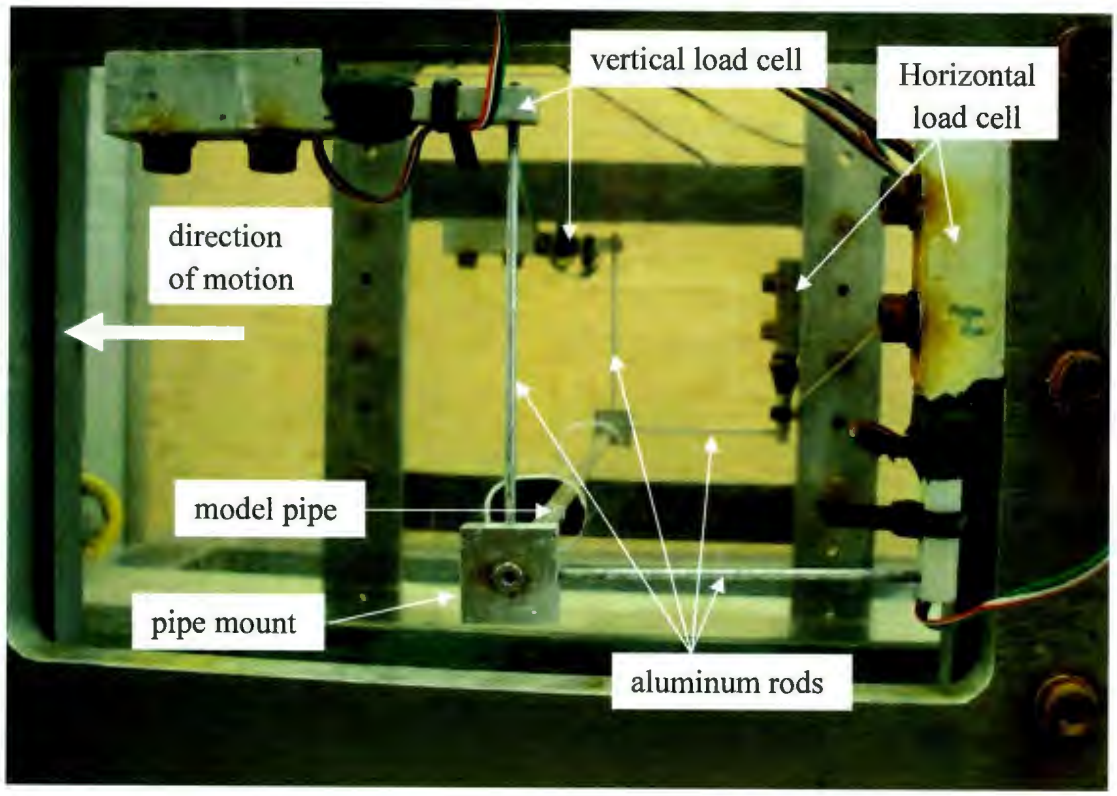

Figure 3.11: Load cell systems with the model pipe going through the plexiglass.

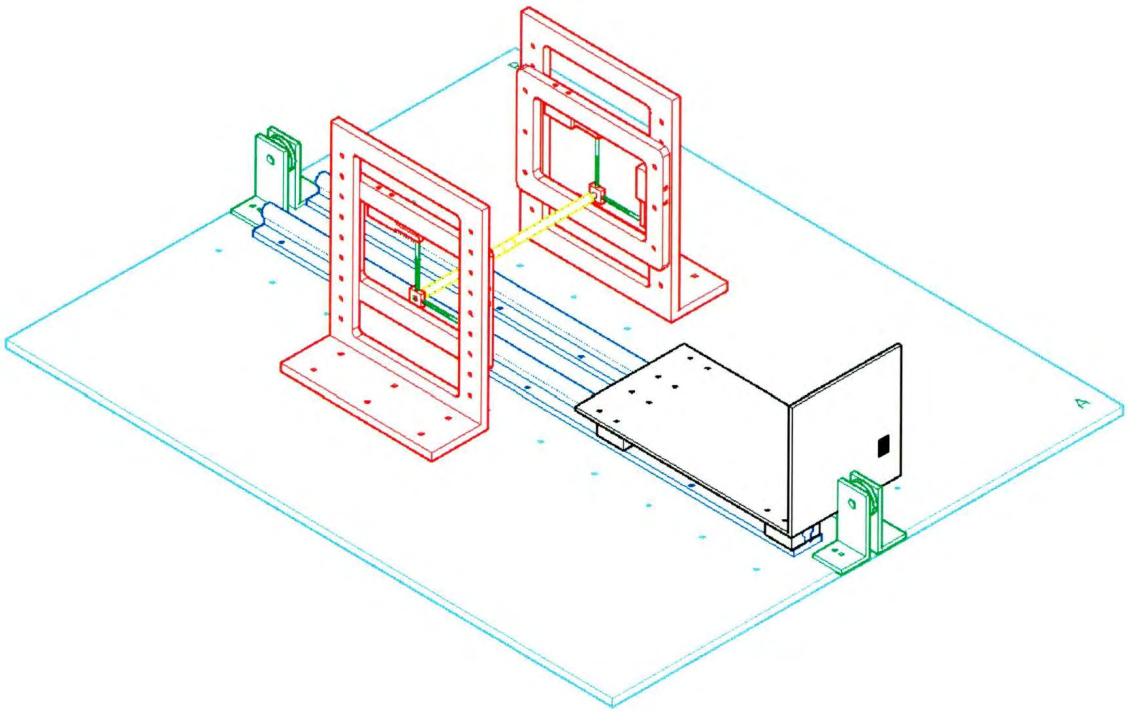

Figure 3.12: Isometric view of the load cell system, along with the cart as a reference in location.

3.2.5 Square Tube for Monitoring Consolidation

A 3 mm thick aluminum square tube of 80 mm long × 80 mm wide × 200 mm high was used to facilitate centrifuge consolidation. This square tube was placed outside of the flume and near the cart (Figure 3.6). The bottom of the aluminum section was filled with a thin layer of sand to allow drainage during consolidation and the rest was filled with the same clay as the clay block.

3.2.5.1 Instrumentations on the square tube

A linear variable differential transformer (LVDT) consists of an armature (solid rod) that moves through a slot within LVDT casing and it is used to measure vertical displacement. The movement of armature changes the voltage, which translates into a

change in position. The armature was attached to a square plexiglass plate through an aluminum rod extension and the plexiglass plate sat on top of the clay square. This plexiglass measured 4.76 mm (3/16") thick and with an area greater than 20 mm × 20 mm. The LVDT was use to measure soil settlement to determine the progress of consolidation during the centrifuge test.

Two pore pressure transducers (PPT) were inserted into the clay square at a depth equals to half of the clay square height. The PPT had a design pressure of 1,379 kPa (200 psi) and it was used to monitor pore water pressure in the clay square.

3.2.6 Vertical Actuators

Two vertical actuators designed by C-CORE were employed to conduct T-bar test and to lift the gate prior to the impact test (Figure 3.13). The actuators were placed above the flume and supported by two wide flange beams. The actuators consisted of a motor which connects to a 20:1 ratio gear box. The actuators are capable of generating a displacement of 550 mm, and can carry a load of 10 kN at a rate of 10 mm/s.

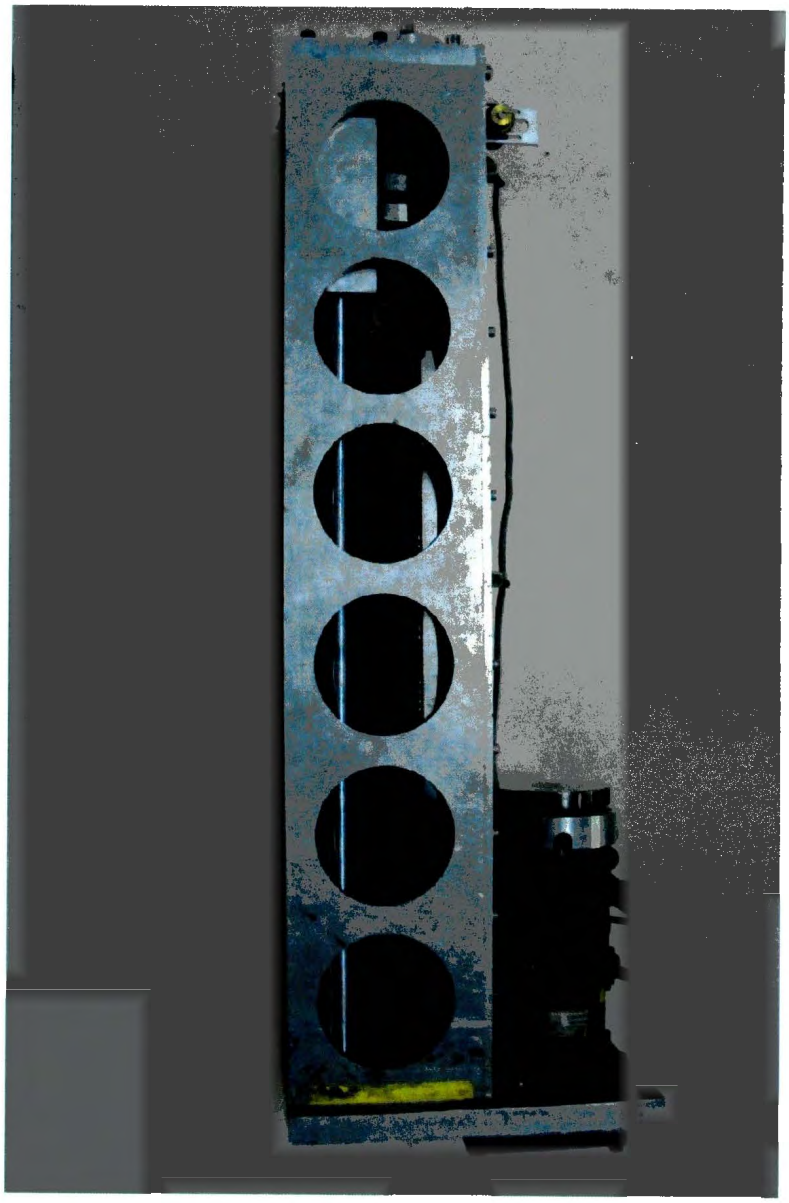

Figure 3.13: Picture of a vertical actuator.

3.2.6.1 Instrumentations on the vertical actuators

Two vertical actuators were employed in this experiment. One was used to conduct the T-bar test, and the other one was used for lifting the gate prior to the impact test. A T-bar is an apparatus used in the offshore industries and centrifuge experiments to determine the undrained shear strength profile in soft clay. The recommended length of

the T-bar should be four to six times the diameter of the cylindrical bar, and the recommended dimensions for the T-bar are a length and diameter of 250 and 40 mm, respectively for in situ testing (DeJong et al., 2010). The T-bar apparatus employed consisted of a solid 30 mm long and 7.5 mm diameter aluminum cylindrical bar, and it is connected perpendicular to the main shaft (see Figure 3.14). Immediately above it was a load cell which measures the resistance generated when the cylindrical bar was pushed into the clay

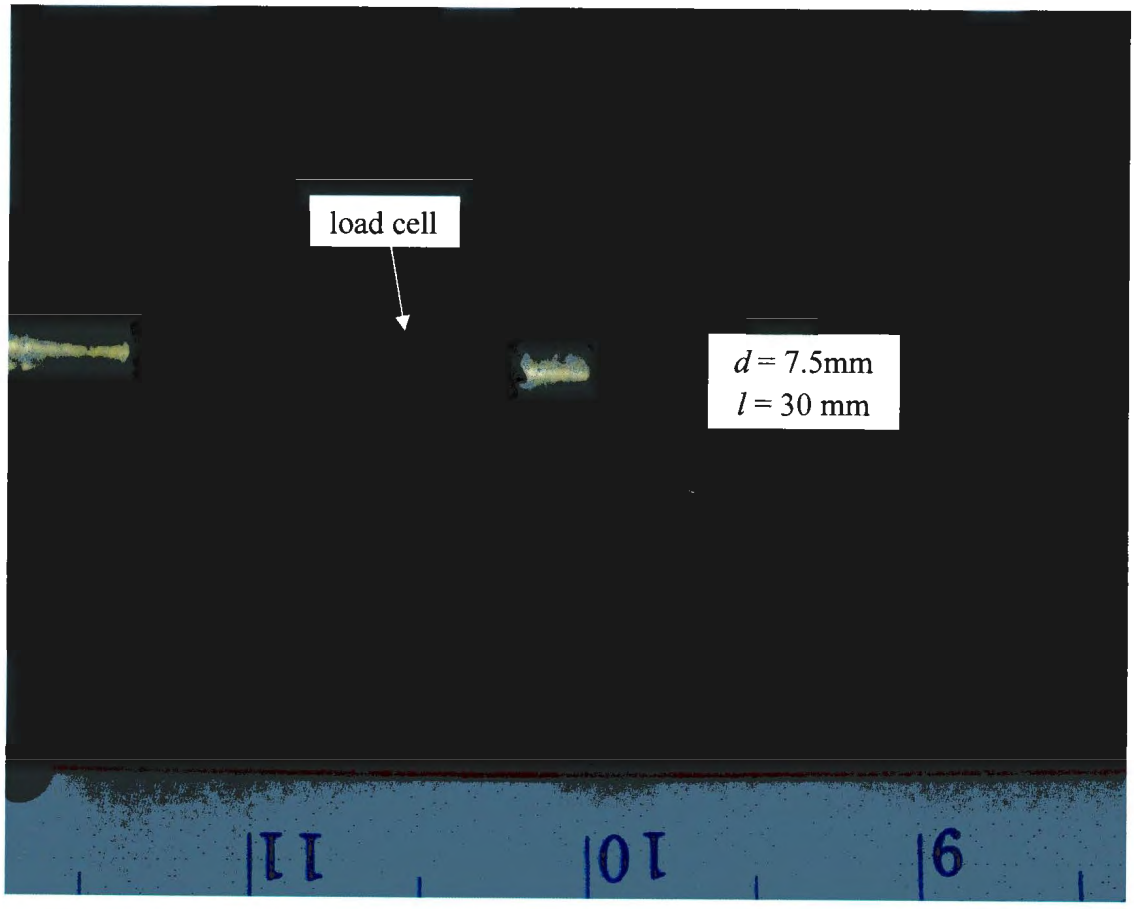

Figure 3.14: T-bar apparatus.

3.2.7 Camera

A black and white underwater camera was placed outside the flume and next to a pipe mount. The camera was used to ensure that the ends of a pipe were in the pipe mounts during the centrifuge flight and to record impact tests.

3.2.8 Data Acquisition System

Data acquisition in the centrifuge was accomplished by using the data acquisition software DAC Express. This software ran on the DACPC computer. This computer can be accessed from the computer CENTDAS through fibre optic hubs and rotary joint. DACPC then interfaces to a VXI data acquisition chassis with a VT1415 and a VT1503 data acquisition cards. These cards receive signals from the C-CORE signal conditioning boxes (S/C box) to which individual transducers/instruments were plugged in (C-CORE, 2011). Figure 3.15 shows the general overview of the data acquisition and signal conditioning system.

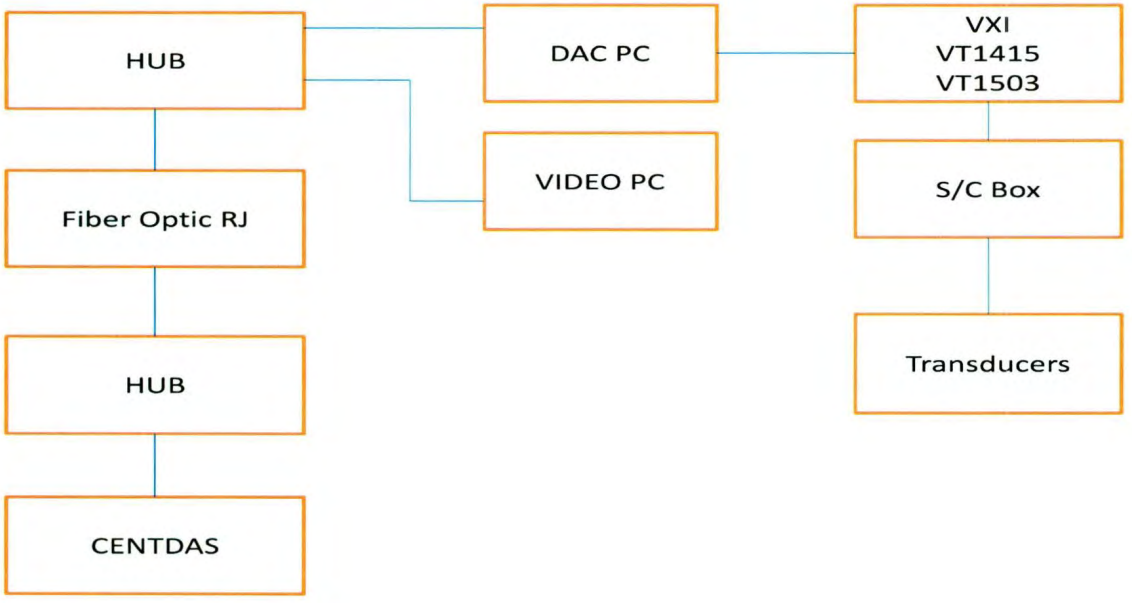

Figure 3.15: Signal Conditioning Schematic (C-CORE, 2011).

Data processing was done using of MATLAB software, which is one of the high performance interactive software programs for scientific and engineering numeric computations.

3.2.8.1 Signal conditioning boxes

For successful data acquisition, the signal from the transducers/instruments must be conditioned. This was done by using a signal conditioning (S/C) box. It allows amplification, filtering, and linearization of the signal.

There are 24 channels in the S/C box used in the experiment. Each of the transducer connections was configured on their respective S/C cards inside the box. There are 12 S/C cards and each had one circuit for 2 channels. Gain and excitation were set using these cards. To set the gain, the jumper was placed on its respective pins (Figure 3.16). To set the excitation, the same approach was used. Set the jumper on the respective pin for 2.5, 5, 7.5 or 10V excitation. The differential devices were zeroed prior to flight.

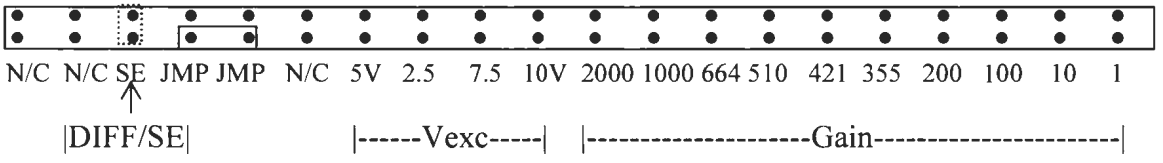

Figure 3.16: S/C channel configuration.

3.3 Soil Specimen Preparation

In general, a glide or out-runner block is a cohesive soil block. The geotechnical properties of these soil blocks vary from site to site. As the soil block can travel very fast and permeability of clay is very low, the undrained shear strength should be considered. Different types of undrained shear strength profiles have reported from various sites and used in modeling pipe/soil interaction behaviour (e.g., Morrow and Bransby (2011), Cheuk and White (2011)) The undrained shear strength of clay near the seabed might increase linearly with depth (e.g., Cheuk and White (2011)) or might be constant up to certain depth (e.g., Morrow and Bransby (2011)) in some cases. In this study, a constant shear strength profile was used. Clay specimens were prepared using kaolin clay since it is readily available.

3.3.1 Soil Properties

The soil used in this experiment was 100 % Speswhite kaolin clay. The geotechnical properties of the kaolin clay are: Liquid Limit (LL) = 60 %, Plastic Limit (PL) =32 %, Specific Gravity (G_s) =2.6, and coefficient of consolidation, c_v, reported by Dingle et al. (2008) was 2.0 m^2/year. The particle size distribution curve of kaolin clay is shown in Figure 3.17.

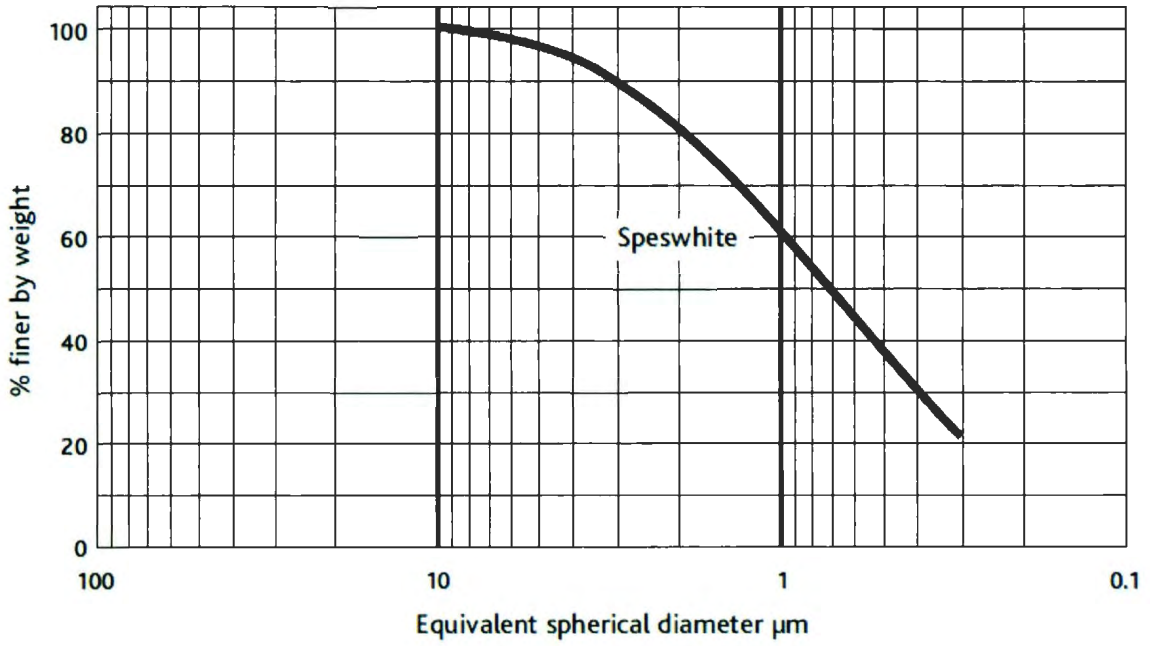

Figure 3.17: Typical particle size distribution for Speswhite kaolin clay (Speswhite, 2007).

3.3.2 Lab-Floor Consolidation

The kaolin clay slurry was mixed under vacuum condition at water content of 120 %, which is equal to 200 % of *LL*. The clay was then consolidated on the laboratory floor. This reduced the time required to consolidate in centrifuge. Clay consolidation on the laboratory floor will be referred to as "lab-floor consolidation". Below are the apparatus and procedures for the lab-floor consolidation.

A plain strain box, hereafter will be referred to as "consolidation box", with an inner dimension measured 900 mm long × 300 mm wide × 400 mm high was used to contain the clay during the lab- consolidation. One side of the consolidation box can be taken out by loosen sixteen (16) M16 bolts.

A drainage layer was prepared by placing an approximately 10 mm thick layer of sand followed by a layer of geotextile (see Figure 3.18). Above this geotextile layer were geotextile sandwiches measured 398 mm long ×198 mm wide. This sandwich consisted of a layer of geotextile laid between two 3 mm thick perforated aluminum plates. These two sandwiches were placed at the corners of the consolidation box, as shown in Figure 3.18.

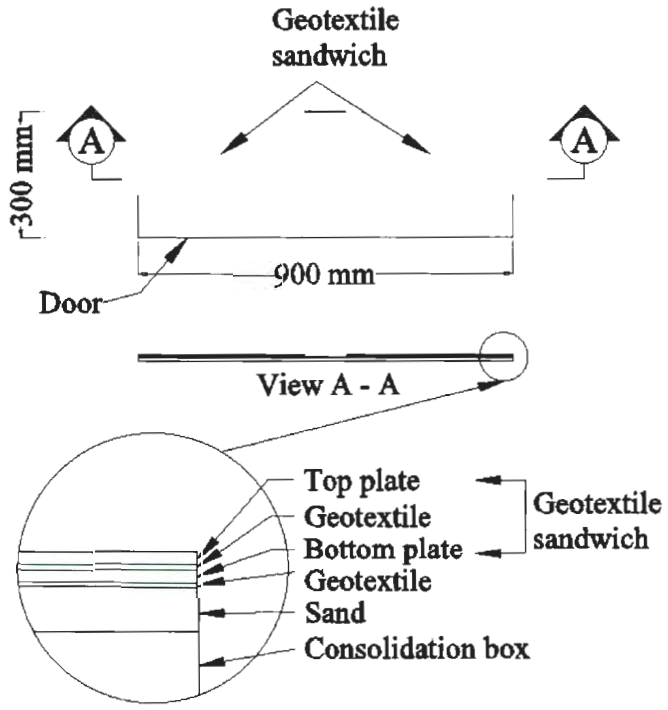

Figure 3.18: Consolidation box and drainage layer layout.

Kaolin clay was mixed with deionised water under vacuum for three hours at a moisture content of 120 %, which is equal to 200 % of *LL*. The slurry was poured into the consolidation box through a chute for the lab-floor consolidation.

After the slurry was poured to the desired height, a layer of filter paper and a layer of geotextile were placed on the top of the slurry. On top of this, a piston was placed with

a load of 110 kg that created a consolidation stress of 4.0 kPa. Due to the weak strength of the slurry, this consolidation stress was required for overnight to develop enough strength to carry the lowest applied load produced by the hydraulic ramp. After that the consolidation box was carefully transferred to the center of a consolidation frame, where a hydraulic ramp was used to apply a vertical force on top of the piston. The lowest force generated from the hydraulic ramp was around 3.0 kN, corresponding to a vertical stress of 15.11 kPa (including the stress from the piston).

The progress of consolidation was monitored by Taylor's square-root-of-time method (Holtz and Kovacs, 1981). Once the degree of consolidation past 90%, the next load increment was applied. Each load increment was two to three times of the current load. The maximum consolidation stress applied to the clay in lab-floor consolidation ranged from 40 to 120 kPa. During the progress of consolidation, the bottom drainage valve was opened to allow for two-way drainage. The plots of lab-floor consolidation are shown in the Appendix.

After the desired maximum consolidation pressure was achieved and, the load was removed in the reverse order. The unloading steps were typically once per 24 hours, with bottom drainage still open. Once the unloading was finished, the consolidation box was removed from the consolidation frame, with the piston still on top of the clay and bottom drainage valve closed. A stress of 4.0 kPa generated from the piston was maintained on top of the consolidated clay to reduce clay expansion.

3.3.3 Soil Specimen Preparation

The piston was lifted out of the consolidation box prior the clay block and clay square preparation. Figure 3.19 illustrates the cutting layout. Two clay blocks were

obtained from a single consolidated clay block on lab floor. When preparing to cut, lubrication (WD 40) was applied to two 1 mm thick aluminum plates (400 mm × 200 mm and 210 mm × 200 mm), the square tube, and the plexiglass near the cart where it will contact with the clay block. This lubrication reduces the chances of the clay from sticking to the glass and metals. In addition, the surface of submerged plexiglass (wetted surface) becomes very slippery, and their influence on the clay was considered insignificant (Zakeri et al., 2008).

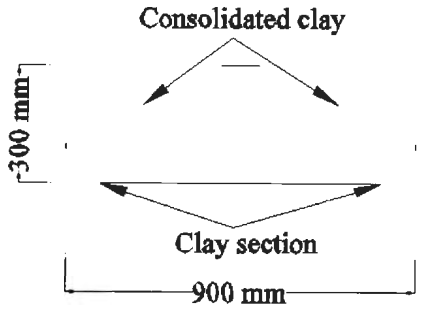

Figure 3.19: Layout for cutting the clay blocks and clay squares.

The clay block was cut from the consolidated clay by pushing the two 1 mm plates vertically at the location above the geotextile sandwich edges. The square tube was also pushed into the consolidated clay from the top end. This allows the top portion of the tube flushed with clay, leaving the bottom portion empty for fine sand afterward. Once the plates and square tube were inserted into the consolidated clay, the door from the consolidation box was removed and excess clay was removed around the square tube and clay block. The clay block, which sat on top of the geotextile sandwich, was lifted out of the consolidation box by the support from the top plate of the sandwich. The clay block was trimmed to the desired height by a thin air craft cable, and transported to the

cart along with the clay square. Figure 3.20 shows a picture of a clay block ready to be placed on top of the cart.

Figure 3.20: A clay block ready to be placed on top of the cart.

Supports were provided all around the remaining consolidated clay (see Figure 3.21) and weights were placed on top to reduce failures from the sides and expansion, respectively.

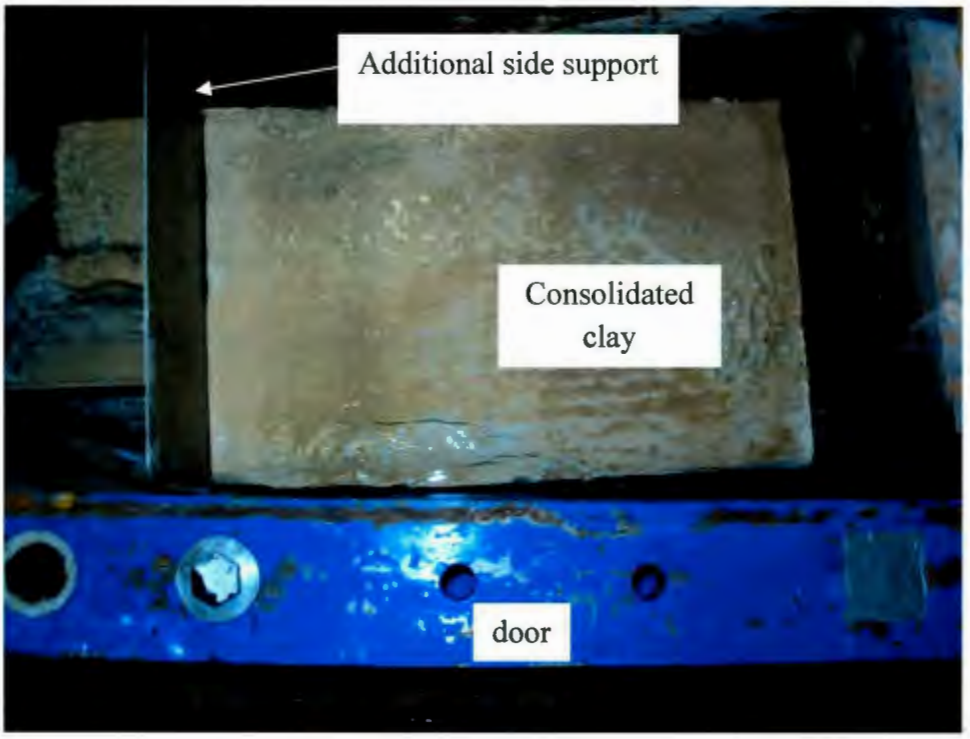

Figure 3.21: Preserving the second clay block.

3.4 Centrifuge Test Procedures

Once the experimental setup was complete, the package was transferred to the centrifuge where a centrifugal force of 30 times of Earth's gravity was applied to the soils. The soil was allowed to consolidate under 30g in the centrifuge. After 90% consolidation in the centrifuge, T-bar tests were conducted to determine the undrained shear strength profile of the clay block. The impact tests were conducted after this. Further details of test procedure are given in the following sections.

3.4.1 Test Preparation

After the clay blocks were placed in its appropriate place, water was transferred to the strong box via water hose. Water supply was stopped once the water level reached

approximately 20 mm over the top of the walls. Two PPT were inserted into the clay square at a depth equals to half of the clay block's height. Additional clay was used to fill the borehole created from the PPT insertion. LVDT was placed in the middle of the clay square and was slightly pushed into the clay to ensure water splash generated from the centrifuge spin up does not move it.

Distances from the top of the clay block to the T-bar and top of the wall, and model pipe to the top of plexiglass wall were measured. These measurements were used to determine the penetration depth of the T-bar test and to determine the range of undrained shear strength values which will be used to develop the soil and pipe interaction relationship.

The experimental setup was moved to the centrifuge platform. System check was conducted to ensure all instruments were working properly. The system check include checking the response of the load cells, T-bar, LVDT, string potentiometer, limit switch, actuators, and servo motor.

3.4.2 Centrifuge Consolidation and Impact Test

The sides of the clay block were supported by the cart and plexiglass. The clay block was allowed to consolidate (two-way drainage) under self weight during the centrifuge flight. The centrifuge consolidation progress was monitored by the use of clay square, LVDT, Taylor's square-root method, and two PPT. Centrifuge consolidation was terminated when it has past 90% degree of consolidation. During that period, the excess pore water pressure within the clay square was not fully dissipated. Nonetheless, more than 90% centrifuge consolidation was achieved by two to three hours. The plot of

centrifuge consolidations is shown in the attached Appendix. The minimum height of the clay blocks after completion of the centrifuge consolidation was 140 mm.

T-bar tests were conducted on the clay block to determine its undrained shear strength profile. DeJong et al. (2010) recommended a penetration rate of 20 mm/s for standard sized T-bar (length 250 mm and diameter 40 mm) and $0.5d$/s for non-standard size, where d is the diameter of the T-bar. The T-bar currently employed has a diameter of 7.5 mm and it was penetrated vertically into the clay block, at 3 mm/s, to a depth until 20 mm from the bottom. This initial penetration provides the intact undrained shear strength profile. It was then cycled within the clay block. This cyclic loading provides the remoulded undrained shear strength profile. The frequency used to record the T-bar test data was 40 Hz.

After the T-bar test, the gate at the front of the clay block was lifted. The cart was moved forward towards the model pipe by the servo-motor and impacts the model pipe at its mid height. The cart traveled at a velocity ranged from 0.04 to 1.30 m/s. The frequency used to record the impact test data ranged from 400 to 2,000 Hz.

3.4.3 Post Test

Once the clay block impacted the model pipe and the centrifuge stopped, water was removed from the strong box via a water pump. A number of soil specimens were collected from various depths by inserting a Shelby tube into the undisturbed clay of the clay square. These specimens were used for moisture content test.

3.5 Limitations

There are some limitations of this experiment which are related to the method used to monitor centrifuge consolidation and modeling of the submarine glide block and out-runner block.

Monitoring of centrifuge consolidation was done on the clay square, not directly of the clay block. To accurately monitor the clay block with the clay square, the container of the clay square must not have boundary effect, and the material, thickness, and the radius from the center of centrifuge rotation must be identical. The clay square was located inside of the lubricated (WD-40) aluminum square tube near the clay block, and was prepared from the same parent lab-floor consolidated clay block. The distance from the centrifuge to mid-height of the clay block is around 5.3 m. If the height of the clay square is ± 10 mm of the height of the clay block. The centrifugal force experienced by the clay block and clay square is almost identical, and therefore the clay square is a representative of the clay block for consolidation monitoring.

The clay block being model was ideally a rectangular shape. When the gate was lifted prior to the impact test, a section located at the front of the clay block sheared off due to the removal of front support and created a wedge shaped block. The failure pattern was similar to an undrained failure of a vertical cut with a slope of approximately 45° (Figure 3.22a). It was thought that it would interfere with the drag force results but there was enough intact soil for the test to achieve a steady state. Also, the system was properly designed such that the failed soil went under the cart while it advanced and therefore no accumulation of clay occurred at the front of the clay block (Figure 3.22b).

a)

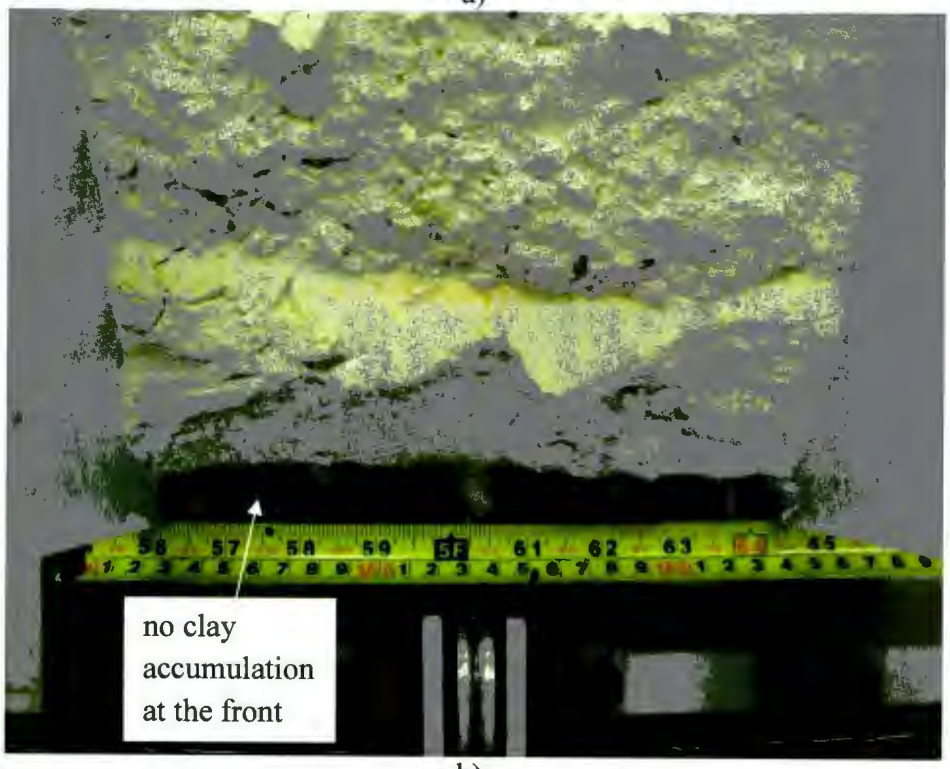

b)

Figure 3.22: Pictures of the clay block after the test (Test 4).

Chapter 4

Experimental Results and Discussions

4.1 Overview

A total of 11 centrifuge tests were conducted at a g-level of 30. In the following sections, these tests are referred to as Test 1 to 11. A 12 m long × 6 m wide ×5 m high block of clay was used to simulate a submarine glide block or out-runner block impacting suspended pipelines with an outer diameter of 0.19 m and 0.29 m.

A geotechnical approach was used to develop a relationship to estimate the drag force generated from the glide block or out-runner block onto a suspended pipeline. This is an appropriate approach since a glide block and out-runner block are essentially an intact soil, and carries the strength properties of the parent soil mass. To develop this relationship, Equation 2.1 was rearranged to:

$$k = \frac{F_D}{s_u \cdot D \cdot L} \tag{4.1}$$

where F_D is the drag force generated from the moving clay block, s_u is the intact undrained shear strength at pipe center, D is the pipe diameter, and L is the length of pipes. The length of the pipes used was 200 mm.

Giving the recorded frequency used in the tests ranged from 400 Hz for slow tests to 2,000 Hz for the fast tests, the number of scans as the clay particle moves from one end of the pipe to the other end ranged from 12 to 93 scans. Therefore, the frequency used this study is adequate for recording.

The following sections describe the methods used to convert the experimental data to useful engineering values.

4.2 Undrained Shear Strength

T-bar is an apparatus used to determine the undrained shear strength profile in soft clay. T-bar does not displace soil like the cone penetration test; it allows the soil to flow around the cylindrical bar. It can generate a continuous profile of undrained shear strength like the cone penetration test, and the resisted force is related to the shear strength without an empirical correlation, like the vane test (Stewart and Randolph, 1994). The undrained shear strength profile of the clay block was determined by using the following equation:

$$s_u = \frac{P}{N_b \cdot d \cdot l} \tag{4.2}$$

where P is the resisted force acting on the T-bar, N_b is the T-bar factor, and d and l are the diameter and length of the cylindrical bar, respectively. For general purpose, a T-bar factor of 10.5 was recommended by Stewart and Randolph (1994). To ensure the test was conducted in an undrained condition, a non-dimensional velocity of $v \cdot d/c_v > 30$ was maintained in this study as suggested by Dingle et al. (2008), where v is the vertical rate of penetration of the T-bar, and c_v is the coefficient of consolidation. In this study, the diameter of the T-bar is 7.5 mm, c_v is 2.0 m^2/year (Dingle et al., 2008) and the velocity of penetration is 3 mm/s (recommended rate was $0.5d$/s for non-recommended T-bar size (DeJong et al., 2010) which gives $v \cdot d/c_v > 30$

Some technical issues encountered during T-bar test for Test 4, 5, and 8. For Test 4 and 5, the T-bar test data were not recorded properly. The undrained shear strengths were estimated from Test 1 since it had the same final lab-floor consolidation. For Test

8, the voltage shifted during the T-bar test and most likely it occurred after the initial penetration.

4.2.1 Correction Factor

The load cell for the T-bar is located above the T-junction (see Figure 3.14) and it measures not only the resistance acting on the bar as it penetrates into a soil, but it can measure the buoyancy force as well. The general equation for buoyant force is shown in Equation 4.3.

$$F_b = \rho_f \cdot V_{disp} \cdot g \tag{4.3}$$

where ρ_f is the density of the submerged fluid, V_{disp} is the volume of displaced fluid, and g is the gravity. The volume of displaced water created by the T-bar that is below the load cell is constant, therefore, the buoyancy force experienced by the load cell will remain the same regardless of the depth. However, as indicated in Figure 4.1a, the response of the T-bar changes as it travels between the initial/starting position and the surface of the clay block, and if the clay block was not present, this trend seems to continue as shown by the "predicted T-bar response" section. This change was caused by the change in radial acceleration as it travels away from the center of rotation. To eliminate this effect, a correction factor (the linear slope of the predicted T-bar response) was applied to the original data. This was done by adding the product of the correction factor with its corresponding depth and the result is shown in Figure 4.1b. This figure also shows the predicted response does not change as it travels. The correction factor for each test is shown in Table 4.1. Theoretically, there should be only one correction factor for all of the tests given that the tests were conducted at the same g level. However, due

to the low sensitivity of the T-bar apparatus and weak soil strength, a gain of 2,000 was applied, (i.e., outputs 2,000 times higher). Because of this large gain, the output may have changed slightly from each test.

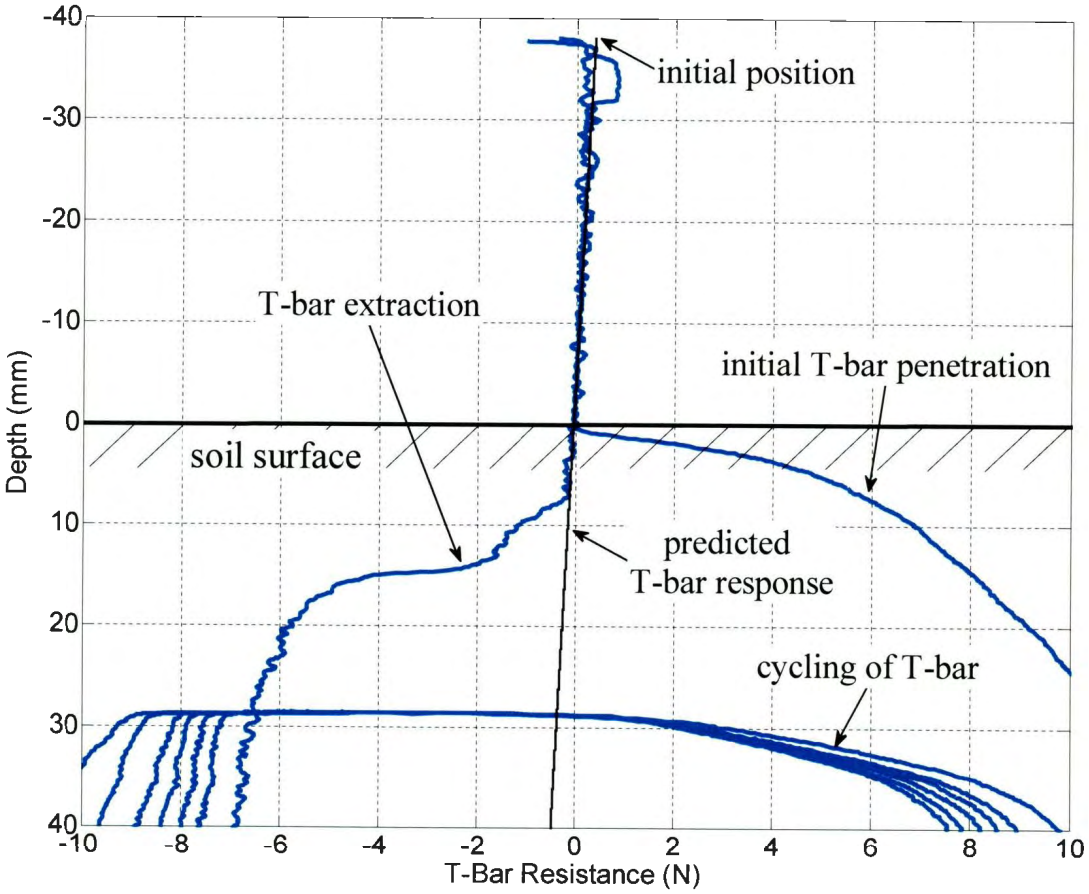

a)

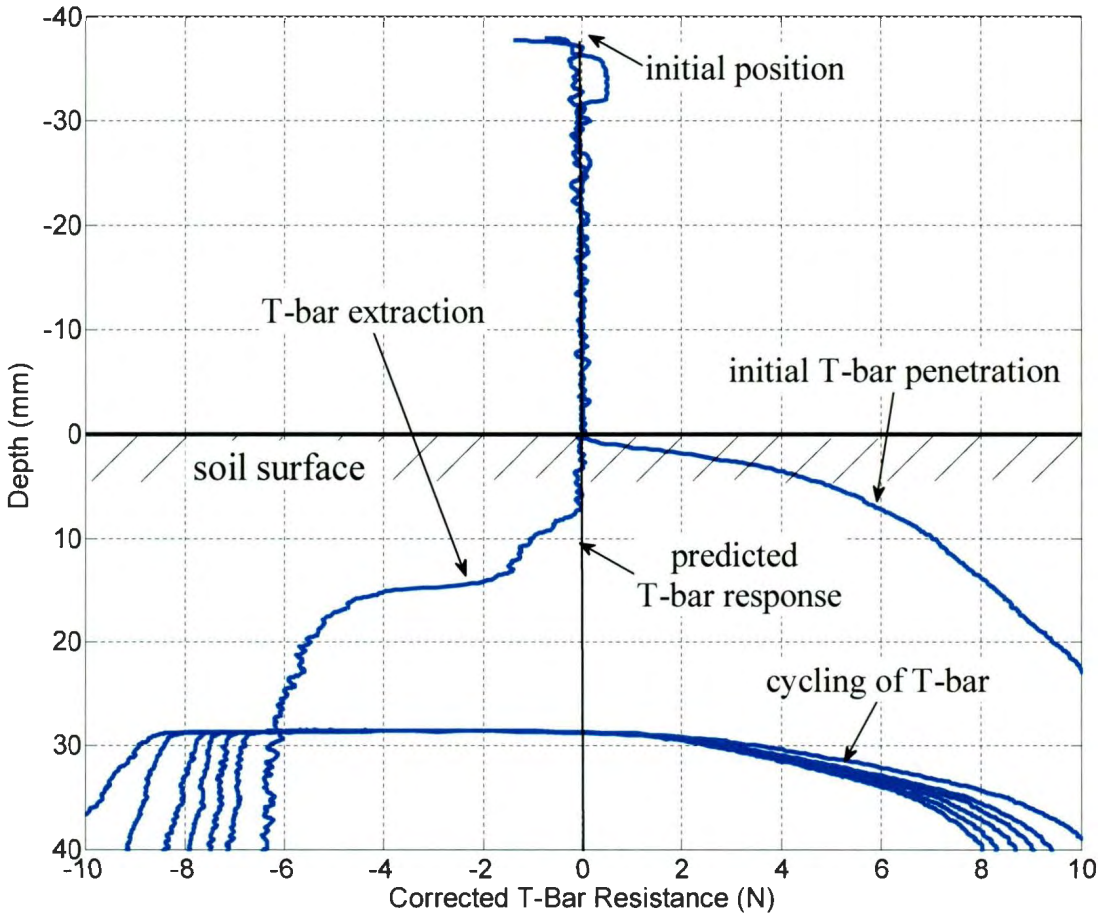

b)

Figure 4.1: T-bar response: a) without and b) with the correction factor (Test 11).

Applying the correction factors listed in Table 4.1 for different tests, the corrected values of P were obtained. Now using Equation 4.2, the undrained shear strength profile was calculated. Figure 4.3 shows the undrained shear strength profile of the clay block in Test 11. Similar undrained shear strength profile was obtained for other tests which are shown in Appendix.

Table 4.1: Correction factors for T-bar tests in submerged condition.

Test	Correction Factor
1	0.00604
2	0.00809
3	0.00591
4	N/A
5	N/A
6	0.00572
7	0.00451
8	0.00032
9	0.00642
10	0.00680
11	0.01086

4.2.2 Undrained Shear Strength as a Function of Depth

A relationship between vertical stress and s_u have been proposed by many authors (see page 410 of Das (2006)). For normally consolidated (NC) clay, Mesri (1989) proposed the following relationship:

$$\left(\frac{s_u}{\sigma_v'}\right)_{NC} = 0.22 \tag{4.4}$$

where s_u is the undrained shear strength and σ_v' is the vertical effective stress. For overconsolidated (OC) clay, Ladd et al. (1977) proposed:

$$\left(\frac{s_u}{\sigma_v'}\right)_{OC} = \left(\frac{s_u}{\sigma_v'}\right)_{NC} \cdot OCR^n \tag{4.5}$$

Lehane and Gaudin (2005) conducted T-bar tests on overconsolidated kaolin clay. They found good match between the experimental and theoretical values when Equation 4.5 and Mesri, (1989) proposed value was used along with $n = 0.8$. A more recent study by Dingle et al. (2008) on kaolin clay found good match between the experimental results and theoretical values when $\left(\frac{s_u}{\sigma_v'}\right)_{NC} = 0.19$ and $n = 0.71$ was used in Equation 4.5.

The undrained shear strength at the centre of the pipe is compared. The over consolidated ratio (OCR) at this depth was calculated by dividing the lab-floor consolidation pressure by the vertical effective stress at this depth during the centrifuge flight. In this experimental program, a value of $\left(\frac{s_u}{\sigma_v'}\right)_{NC} = 0.16$ and $n = 0.68$ were used to match the theoretical values with the experimental results, and are plotted in Figure 4.2 and tabulated in Table 4.2. This small variation of shear strength parameters between the current study and Lehane and Gaudin (2005) or Dingle et al. (2008) could be caused by different kaolin clay used and/or the sensitivity of the T-bar apparatus.

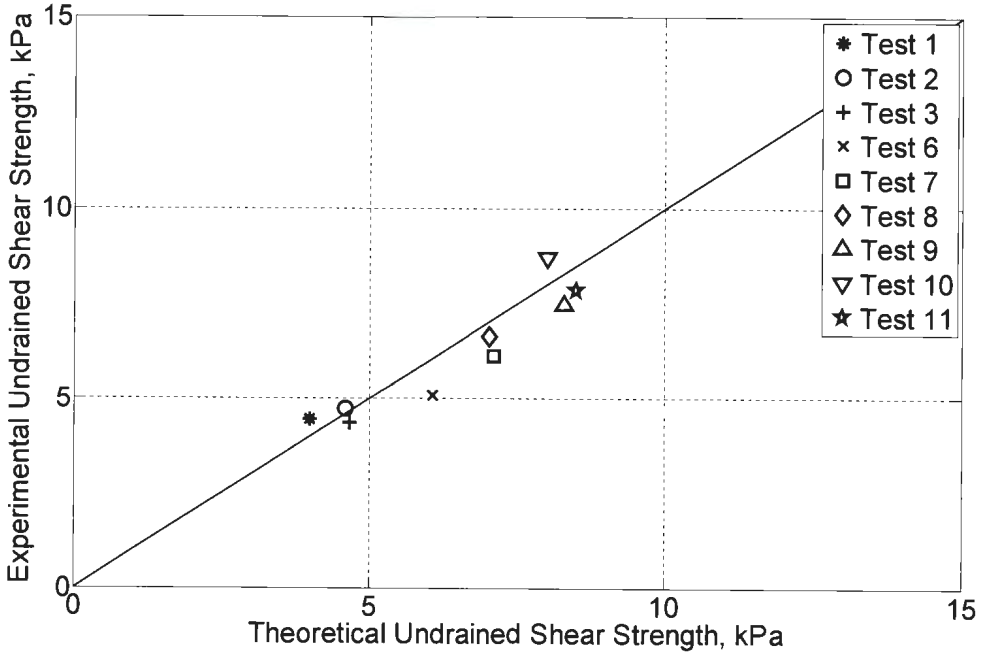

Figure 4.2: Comparison between theoretical and experimental results of undrained shear strength.

Table 4.2: Summary of theoretical and experimental results on undrained shear strength.

Test	Theoretical (kPa)	Experimental (kPa)
1	3.95	4.45
2	4.52	4.74
3	4.58	4.36
4	3.94	-
5	3.93	-
6	5.97	5.09
7	6.97	6.13
8	6.91	6.64
9	8.12	7.47
10	7.86	8.71
11	8.34	7.86

Figure 4.3 shows that the shear strength is zero at the clay surface. During the first penetration, the undrained shear strength increased rapidly near the ground surface. It is to be noted here that the shear strength obtained by using the T-bar factor of 10.5 near the ground surface is not representative and a T-bar factor of 10.5 is suitable when $h/d \geq 4$, where h is the embedded depth and d is the diameter of the T-bar (Oliveira et al., 2010). C-CORE uses a T-bar factor of 6.3 at the surface and linearly increases to 10.5 at a depth of $2d$. For this experiment, the soil strengths that were interested were located well below $2d$ and the proposed T-bar factors from C-CORE have no influence on it. Figure 4.3 also shows that the undrained shear strength increase nearly linear with depth and it is expected in soft clay after a depth of approximately 10 mm. Neglecting the data in the upper 10 mm, the undrained shear strength profile can be represented as:

$$s_u = s_{um} + y \cdot h \tag{4.6}$$

where s_u is the undrained shear strength of clay during the first penetration, s_{um} is the undrained shear strength of clay at depth equal to zero (i.e., at the surface), y is the

strength gradient in kPa/m and h is the depth in meter. Based on the experimental results presented in this study, the values of s_{um} ranged from 1.89 to 5.42 kPa and y values ranged from 0.02 to 0.05 were obtained and it is listed in Table 4.3.

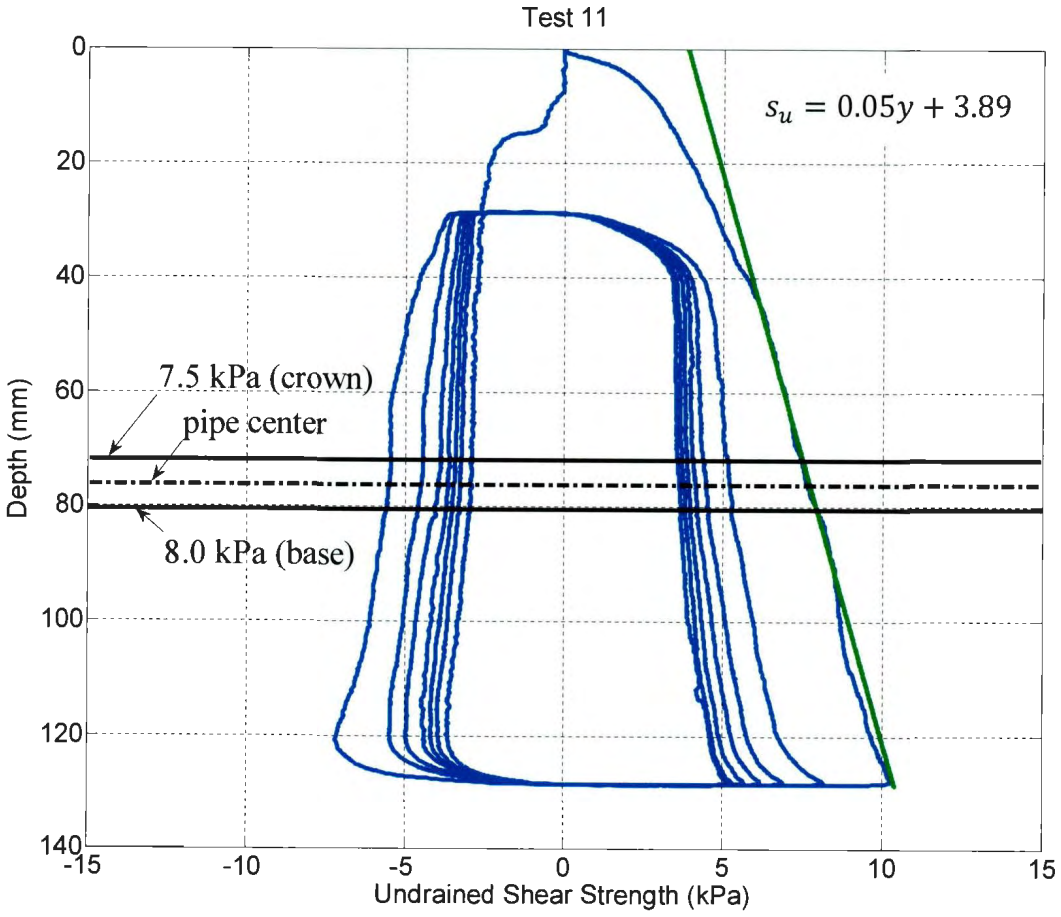

Figure 4.3: Undrained shear strength profile of the clay block of Test 11.

Table 4.3: List of y and s_{um} values.

Test	y	s_{um}
1	0.02	2.17
2	0.04	2.70
3	0.04	1.89
6	0.04	2.04
7	0.02	4.29
8	0.04	4.17
9	0.05	3.66
10	0.04	3.42
11	0.05	3.89

4.2.3 Sensitivity of Clay

Sensitivity, S_t, can be determined by using the following equation:

$$S_t = \frac{s_u}{s_{ur}} \tag{4.7}$$

where s_u is the intact undrained shear strength and s_{ur} is the remoulded undrained shear strength. The remoulded undrained shear strength was assessed by cycling (i.e., a cycle is defined as one penetration and extraction) the T-bar within the clay until the values of the resistance reach a steady value. DeJohn et al (2010) suggest this remoulded value to be taken after the 10th cycle. In this experiment, the T-bar was cycled 4 to 7 times; lower than the one recommended by DeJohn et al (2010). However, as shown in Figure 4.3, the strength variation between the 6th and the 7th cycle was very small and can consider that the remoulded strength value to be taken at the 7th cycle. Figure 4-4 shows the degradation of undrained shear strength and sensitivity of the clay used in the present experiments. An average sensitivity value of 2.13 was calculated for the T-bar tests with remoulded shear strength at 7 cycles, as shown in Table 4.4. Typical sensitivity values

for marine clay ranged from 2 to 5, and 2.0 to 2.8 for reconstituted kaolin clay (Hossain and Randolph, 2009). The sensitivity average values calculated from this experiment fall within the range of marine and reconstituted kaolin clay.

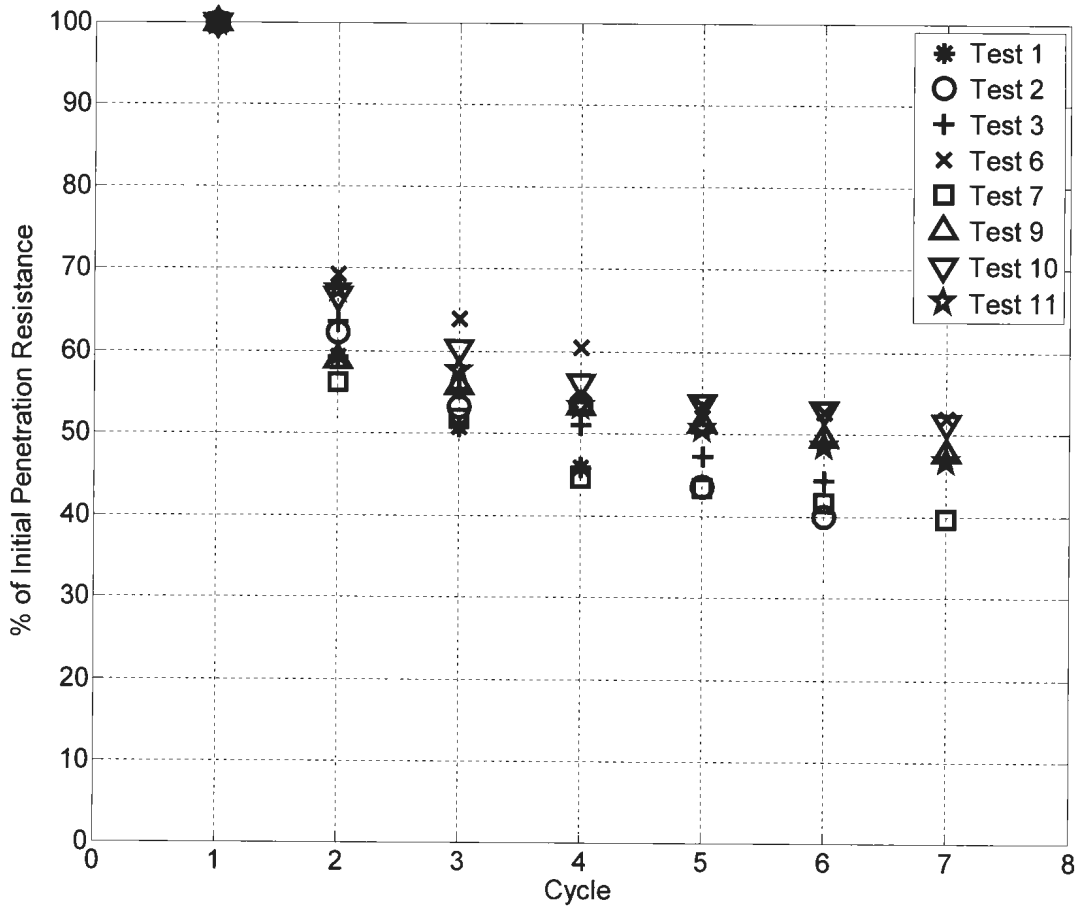

Figure 4.4: Degradation of soil strength during cycling (Note tests 4, 5 and 8 are not displayed due to technical problems).

Table 4.4: Number of cycles conducted for each T-bar test and the sensitivity value.

Test	No. of Cycles	Sensitivity
1	4	2.18
2	6	2.50
3	6	2.26
4	-	-
5	-	-
6	7	1.93
7	7	2.55
8	-	-
9	7	2.10
10	7	1.94
11	7	2.14

4.3 Shear Strain Rate

As mentioned in Section 3.1.1.3, velocity for model and prototype in centrifuge modeling has a 1:1 ratio, and shear strain rate in the prototype is N times higher than the model.

For example, if a glide block is moving through a 1 m diameter pipe at a speed of 1 m/s, the shear strain rate in prototype term (using subscript p to represent the prototype) would be $\dot{\gamma}_p = \frac{V_p}{D_p} = \frac{1\ m/s}{1\ m} = 1\ s^{-1}$. To simulate this in a centrifuge under $50g$, it is possible to model it with a clay block moving at a speed of 0.5 m/s through a 0.01 m diameter pipe. The shear strain rate for the model (using subscript m to represent the model) would be $\dot{\gamma}_m = \frac{V_m}{D_m \cdot N} = \frac{0.5\ m/s}{(0.01\ m)\cdot(50)} = 1\ s^{-1}$.

The shear strain rates for all of the experiments are tabulated in Table 4.5 and it ranged from 4 to 137 s^{-1}.

4.4 Drag Forces

The generated forces from the clay block onto the suspended pipes were measured using two sets of vertical and horizontal load cells. The configuration of the load cells was illustrated in Figure 3.11. It has been verified that horizontal and vertical load cells does not significantly influence each other, see the Appendix for details.

4.4.1 Horizontal Drag Force

Figure 4.5 shows the typical plot of horizontal drag force response measured in this study. It seems that there are two steady state sections. The initial steady state could have created by the inclined face of the clay block, and the second steady state could have caused by the remaining undisturbed clay as it advances.

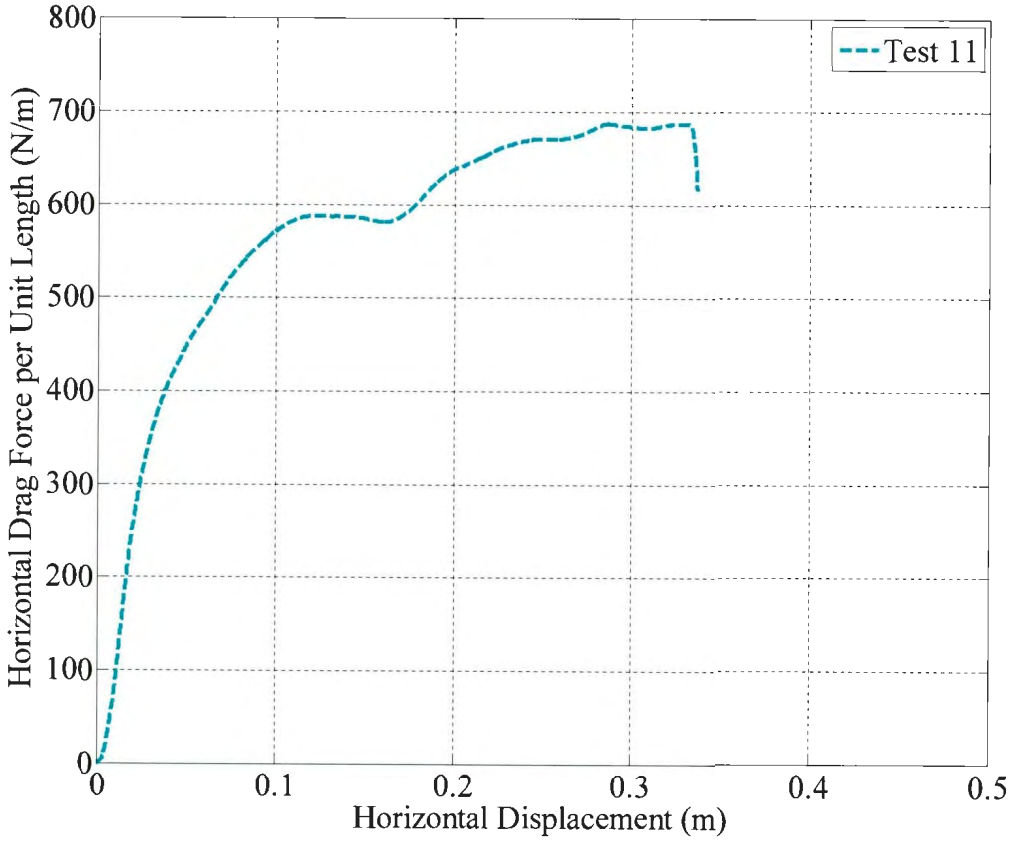

Figure 4.5: Horizontal drag force response of Test 11.

The horizontal drag force values used in the analyses were the maximum values experienced in the test (excluding the little jump near the end, see Test 5 for example). The drag force response for all of the tests are plotted in Figure 4.6.

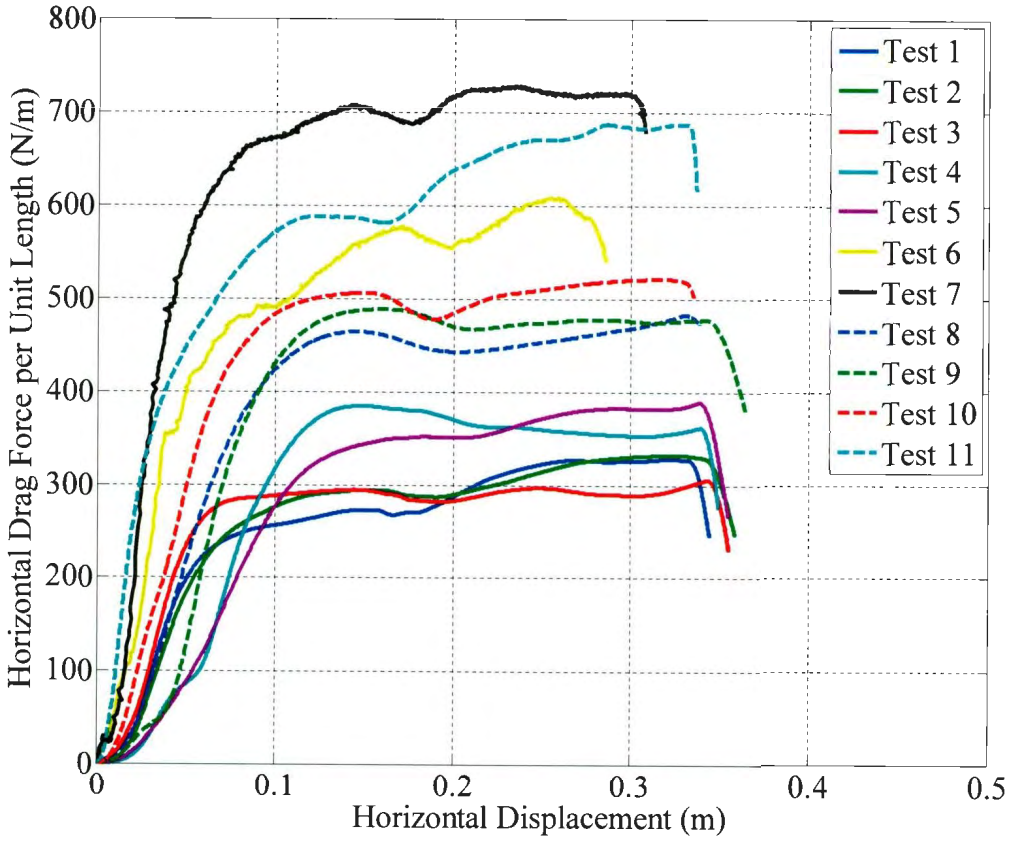

Figure 4.6: Horizontal drag response for all the tests.

4.4.2 Vertical Drag Force

At the beginning of the impact, there is a vertical drag force on the pipes until it displaced approximately 50 mm in the horizontal direction. This vertical drag force was mainly due to the inclined face of the clay block, as discussed in Chapter 3, Section 3.5. This vertical drag force diminishes as the pipe penetrates into the block. Oliveira et al. (2010) demonstrated in physical modeling, by moving a pipe through a 80% kaolin and 20% smectite clay at different *h*/*D* (height/diameter) ratio, that when *h*/*D* is greater than 1, the vertical force becomes virtually negligible. In these tests conducted, the *h*/*D* ratio

ranged from 6.8–12.8 and the magnitude of the upward vertical forces at steady state were insignificant compared to the horizontal drag force, see Figure 4.6 and Figure 4.7.

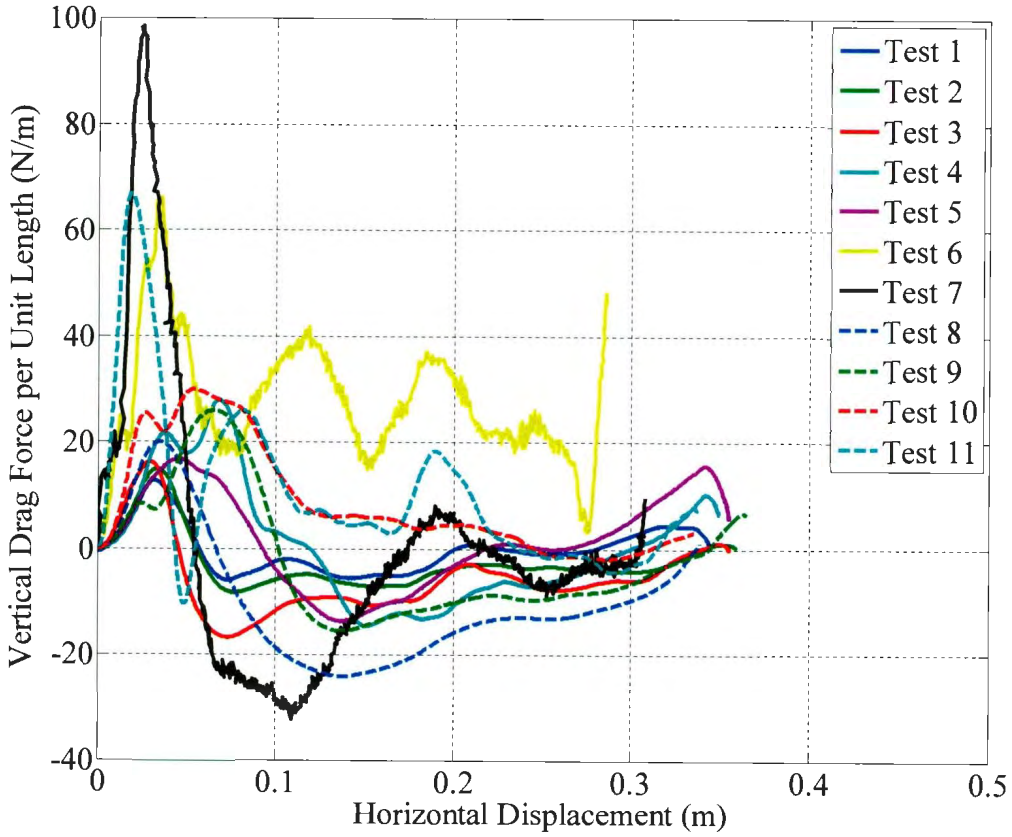

Figure 4.7: Vertical drag force response for all tests.

4.5 Test Results and Proposed Relationship

A summary of all the test results and corresponding test conditions are shown in Table 4.5. All the values listed in this table are in model terms. The conversion factors shown in Table 3.1 could be used to find the values in prototype scales. Pipe diameter of 6.35 mm was used in test 1 to 3 and 8 to 9, while pipe diameter of 9.52 mm was used in test 4 to 7 and 11.

Table 4.5: Experimental parameters and results.

Test	Consolidation Pressure (kPa)	Clay[1] Height (mm)	h/D[2]	Moisture Content (%)	Undrained Shear Strength[3] (kPa)		Velocity (m/s)	Horizontal Drag Force (N)	Shear Strain Rate (1/s)	k
					Intact	Remoulded				
1	40	156	13	68.7	4.45	2.05	0.16	65.49	24.45	11.58
2	60	142	8	64.3	4.74	1.89	0.21	66.64	32.79	11.08
3	60	144	9	65.5	4.36	1.93	0.10	59.44	16.45	10.73
4	40	160	8	65.6	4.09	2.05	0.10	77.07	10.75	9.91
5	40	160	8	65.7	4.09	2.05	0.20	76.60	21.35	9.85
6	80	140	7	64.1	5.09	2.64	1.30	121.80	136.55	12.57
7	100	142	7	62.1	6.13	2.40	0.77	145.70	81.36	12.48
8	100	144	11	62.5	6.64	2.60	0.30	96.74	47.82	11.47
9	120	151	12	60.4	7.47	3.56	0.20	97.98	32.14	10.33
10	120	141	11	60.6	8.71	4.49	0.10	104.40	16.15	9.43
11	120	151	8	58.6	7.86	3.68	0.04	137.40	4.31	9.18

[1] height measured after centrifuge consolidation.
[2] defined as the distance from the clay surface to pipe center over pipe diameter.
[3] at the depth equal to pipe center.

Figure 4.8 plots the calculated drag force coefficient values (k) against the shear strain rates. The fit for the test data can be described by Equation 4.8 and the R-squared value was 0.79.

$$k = 7.5 \cdot \dot{\gamma}^{0.12} \tag{4.8}$$

To proof that k is applicable for various combinations of s_u and $\dot{\gamma}$, Test 9 and 10 were conducted and confirmed with Test 2 and 3, respectively, with the same shear strain rate but a higher soil strength. Figure 4.8 shows that k values generated from Test 2 and 9, and Test 3 and 10 matched closely.

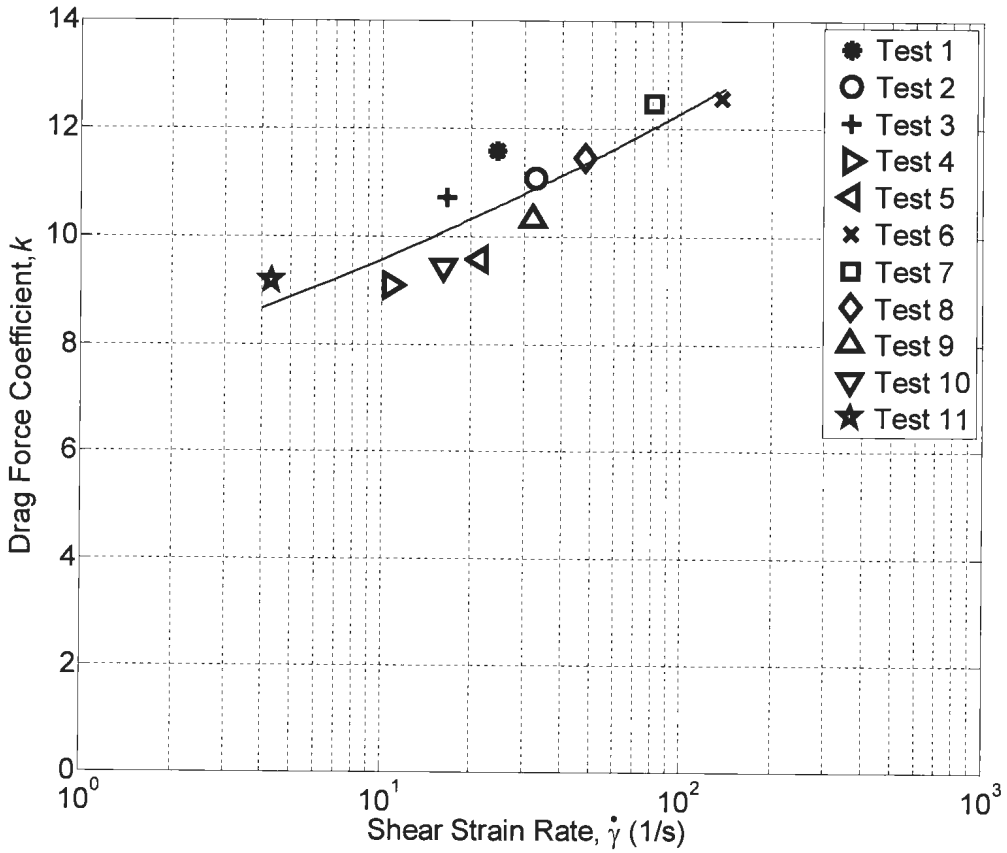

Figure 4.8: Drag force coefficient, k, *vs.* shear strain rate, $\dot{\gamma}$.

4.6 A Worked Example for Impact Drag Force Estimation

Consider a 100 m section of a 0.15 m diameter suspended (free-span) pipeline that is subjected to impact by a submarine glide block approaching at 3 m/s average undrained shear strength of 5 kPa at pipeline location. The impact is normal to the pipe axis. The shear strain rate is:

$$\dot{\gamma} = \frac{V}{D} = \frac{3\ m/s}{0.15\ m} = 20\ (1/s)$$

The drag coefficient, k, is:

$$k = 7.5 \cdot \dot{\gamma}^{0.12} = 7.5 \cdot (20)^{0.12} = 10.75$$

Using Equation 2.1, one obtains the impact drag force in kN normal to the pipe axis as per below:

$$F_D = k \cdot s_u \cdot D \cdot W = 10.75 \cdot (5) \cdot (0.15) \cdot (100) = 806\ \text{kN}$$

It should be noted that it is assumed that the pipeline is moored to the seafloor and it does not deform or move when hit by the glide block.

4.7 Discussions

The relationship for the soil/pipe interaction under glide block impact could be explained by a power-law equation as a function of strain. At a low strain rate, the drag coefficient move towards 7.5, and this is close to the value proposed by Swanson and Jones (1982) and the upper limits from Demars (1978) and Bea and Aurora (1983), but lower than 16 which was recommended by Towhata and Al-Hussaini (1988). Comparing to the authors who used the strain-rate dependent approach, the experiment results show that the values proposed by Georgiadis (1991) and Schapery and Dunlap (1978) were higher than the value found in this study.

Chapter 5

Conclusions and Further Recommendations

The impact of submarine landslides on suspended pipelines is one of the important issues that must be considered in offshore pipeline design. In order to estimate the drag force that might be generated from the impact of submarine glide block or out runner block onto a suspended offshore pipeline, a new experimental technique has been developed in this study. Using this new experimental setup, a total of 11 tests were conducted in an attempt to develop an empirical relationship that can be used to estimate the generated horizontal drag force.

The tests were conducted in the geotechnical centrifuge at C-CORE. The effects of key parameters including shear strain rate, pipe diameter, and undrained shear strength of clay are investigated. The glide block was created from reconstituted kaolin clay consolidating on laboratory floor under a given vertical stress to achieve targeted undrained shear strengths. The test setup allows this clay block to further consolidate during centrifuge flight under self-weight. Undrained shear strength profile of the clay was obtained by T-bar tests. In centrifuge, the clay (glide) block impacted a pipe on its way. The velocity of the clay block was determined by a string potentiometer, and the impact drag forces was measured by two sets of independent horizontal and vertical load cells attached to the pipe. Based on this study, the following conclusions can be made:

- The new experimental setup can be used in geotechnical centrifuge for successful modeling of glide block impact on suspended offshore pipelines.

- There was a small vertical drag force at the beginning of the impact, and it diminishes as the clay block continues through the model pipe. This vertical drag force could be explained by the impact on the sheared off portion of the clay block located at the front.

- Horizontal drag force is much larger than the vertical drag force as expected in deep burial condition ($h/D>1$) considered in this study. This is the main component of drag force if the glide block impacts perpendicular to the pipe as considered in this study.

- Drag force is rate dependent and varies according to a power-law relationship as function of shear strain rate. The drag force is in direct relationship with the undrained shear strength of the soil. It is logical to assume that the undrained shear strength of a soil also varies with shear strain rate according to the power-law relationship.

- In practice, submarine pipe diameters range between 0.1 m to 1.0 m. Assuming a glide or out-runner block velocity of between 1 m/s to 10 m/s, the shear strain rate upon the impact with a pipe would be in the range of 1 s^{-1} and 100 s^{-1}. The experiments covered shear strain rates between about 4 s^{-1} and 137 s^{-1} (i.e., about two log cycles), and therefore, are considered appropriate for practical purposes.

- For design purposes, the recommended k value for estimating the normal drag force is $k = 7.5 \cdot \dot{\gamma}^{0.12}$. This model is based on a fit to physical test data and valid within the range tested. It is directly applicable to prototype situations. Given the scatter in the data and absence of numerical modeling, one may choose to allow for some factor

of safety when applying this equation to prototype situations. Numerical modeling is recommended to further investigate the matter and to increase the confidence in the model.

Although the present study provides a method for quick and efficient estimation of drag force, the model is simply based on the experimental results presented above and valid for impact situations normal to the pipeline axis. Confirmatory and complementary physical testing and numerical modeling is recommended to investigate the drag forces, normal and longitudinal, for various impact angles.

At the end, it should be noted that the above model and test results are based on an intact block of soil impacting a pipe. This may be somewhat conservative as glide-blocks and out-runner blocks undergo some internal deformations as they travel downstream, which in turn, results in reduction in shear strength. As such, the model presented here is likely to provide an upper-bound estimate. Given some scatter in the data, numerical modeling can provide valuable insight and increase the confidence in the model.

References

Audibert, J.M.E., Lai, N.W., and Bea, R.G. 1979. Design of Pipelines-Sea Bottom Loads and Restraints. *In* ASCE Specialty Conference on Pipelines in Adverse Environments - A State of the Art, New Orleans, pp. 15-17.

Bea, R.G., and Aurora, R.P. 1983. Design of Pipelines in Mudslide Areas. Offshore Technology Conference: 1985-1995.

Bjerrum, L. 1972. Embankments on Soft Ground. *In* Proceedings ASCE Specialty Conf. On Performance of Earth and Earth Supported Structures. West Lafayette, IN. Purdue Univ., Vol.2, pp. 1-54.

Blasio, F., Engvik, L., and Elverhoi, A. 2006. Sliding of Outrunner Blocks from Submarine Landslides. Geophysical Research Letters, **33**: 1-4.

Boukpeti, N., White, D.J., Randolph, M.F., and Low, H.E. 2012. Strength of fine-grained soils at the solid-fluid transition. Geotechnique, **3**(62): 213-226.

C-CORE 2011. Centrifuge Instrumentation, Calibration and Data Acquisition Procedures.

Cheuk, C.Y., and White, D.J. 2011. Modelling the Dynamic Embedment of Seabed Pipelines. Geotechnique, **61**(1): 39-57.

Das, B.M. 2006. Principles of Geotechnical Engineering. Thomson, Toronto, ON.

DeJohn, J., Yafrate, N., Degroot, D., Low, H.E., and Randolph, M. 2010. Recommended Practice for Full-Flow Penetrometer Testing and Analysis. Geotechnical Testing Journal, **33**(2): 1-13.

Demars, K. 1978. Design of Marine Pipelines for Areas of Unstable Sediment. Transportation Engineering Journal, **104**: 109-112.

Dingle, H.R.C., White, D.J., and Gaudin, C. 2008. Mechanisms of Pipe Embedment and Lateral Breakout on Soft Clay. Canadian Geotechnical Journal, **45**(5): 636-652.

Fine, I.V., Rabinovich, A.B., Bornhold, B.D., Thomson, R.E., and Kulikov, E.A. 2005. The Grand Banks landslide-generated tsunami of November 18, 1929: preliminary analysis and numerical modeling. Marine Geology, **215**: 45-57.

Gaudin, C., Randolph, M.F., and Loughlin, C.D.O. 2006. New insights from model tests of foundation and anchoring systems in offshore geomechanics. *In* Physical Modelling in Geotechnics. Taylor & Francis. pp. 47-61.

Georgiadis, M. 1991. Landslide Drag Forces on Pipelines. Japanese Society of Soil Mechanics and Foundation Engineering, **31**(1): 156-161.

Harbitz, C., Parker, G., Elverhoi, A., Marr, J., Mohrig, D., and Harff, P. 2003. Hydroplaning of Subaqueous Debris Flows and Glide Blocks: Analytical Solutions and Discussion. Journal of Geophysical Research, **108**: 3-1 - 3-18.

Holtz, R.D., and Kovacs, W.D. 1981. An Introduction to Geotechnical Engineering. Prentice-Hall, Inc., Englewood Cliffs, New Jersey.

Hossain, M.S., and Randolph, M.F. 2009. Effect of Strain Rate and Strain Softening on the Penetration Resistance of Spudcan Foundations on Clay. International Journal of Geomechanics, **May/June**: 122-132.

Ilstad, T., Blasio, F., Elverhoi, A., Harbitz, C., Engvik, L., Longva, O., and Marr, J. 2004. On the Frontal Dynamics and Morphology of Submarine Debris Flows. Marine Geology, **213**(1-4): 481-497.

Kulhawy, A.H., and Mayne, P.W. 1990. Manual on Estimating Soil Properties for Foundation Design.

Ladd, C.C., Foote, R., Ishihara, K., Schlosser, F., and Poulos, H.G. 1977. Stress Deformation and Strength Characteristics. A Proceedings, 9th International Conference on Soil Mechanics and Foundation Engineering, Tokyo, **2**: 421-494.

Lehane, B.M., and Gaudin, C. 2005. Effects of Drained Pre-Loading on the Performance of Shallow Foundations on Overconsolidated Clay. 24th International Conference on Offshore Mechanics and Aractic Engineering, June 12 - 17, 2005, Halkidiki, Greese: 1-6.

Locat, J., and Lee, H. 2000. Submarine Landslides: Advances and Challenges. Proceedings of the 8th International Symposium on Landslides: 1-30.

Longva, O., Janbu, N., Blikra, L.H., and Boe, R. 2003. The 1996 Finneidfjord Slide: Seafloor Failure and Slide Dynamics. *In* Submarine Mass Movements and Their Consequences.

Masson, D., Harbitz, C., Wynn, R., Pedersen, G., and Lovholt, F. 2006. Submarine Landslides: Processes, Triggers, and Hazard Prediction. Philosophical Transaction of Royal Society, **364**: 2009-2039.

Mesri, G. 1989. A Re-evaluation of Undrained Shear Strength Using Laboratory Shear Tests. Canadian Geotechnical Journal, **26**(1): 162-164.

Mohrig, D., Whipple, K., Hondzo, M., Ellis, C., and Parker, G. 1998. Hydroplaning of Subaqueous Debris Flows. Geological Society of America Bulletin, **110**(3): 387-394.

Morrow, D.R., and Bransby, M.F. 2011. Pipe-soil interaction on Clay with a variable shear strength profile. *In* Frontiers in Offshore Geotechnics II. CRC Press, London. pp. 821-826.

Mulder, T., and Alexander, J. 2001. The Physical Character of Subaqueous Sedimentary Density Flows and Their Deposits. Sedimentology, **48**: 269-299.

Nadim, F., and Locat, J. 2005. Rish Assessment for Submarine Slides. *In* Landslide Risk Management: Proceedings of the International Conference on Landslide Risk Management. *Edited by* O. Hungr, R. Fell, R. Couture, and E. Eberhardt. Vancouver. Taylor and Francis Group.

Nakase, A., and Kamei, T. 1986. Influence of Strain Rate on Undrained Shear Characteristics of Ko-Consolidated Cohesive Soils. Soil and Foundations, **26**(1): 89-95.

Oliveira, J., Almeida, M., Almeida, M., and Borges, R. 2010. Physical Modeling of Lateral Clay-Pipe Interaction. Journal of Geotechnical and Geoenvironmental Engineering, **136**(7): 950-956.

Pazwash, H., and Robertson, J.M. 1975. Forces on Bodies in Bingham Fluids. Journal of Hydraulic Research, **13**(1): 35-55.

Prapaharan, S., Chameau, J.-L., and Holtz, R.D. 1989. Effect of Strain Rate on Undrained Strength Derived from Pressuremeter Tests. Geotechnique, **39**(4): 615-624.

Schapery, R.A., and Dunlap, W.A. 1978. Prediction of Storm-Induced Sea Bottom Movement and Platform Forces. Offshore Technology Conference, **OTC 3259**.

Speswhite 2007. http://www.imerys-perfmins.com/uploadfiles/44/DAT002K_Speswhite.pdf.

Stewart, D.P., and Randolph, M.F. 1994 T-Bar Penetration Testing in Soft Clay. Journal of Geotechnical Engineering, **120**(12): 2230-2235.

Swanson, R.C., and Jones, W.T. 1982. Mudslide Effects on Offshore Pipelines. Transportation Engineering Journal, **108**(6): 585-600.

Taylor, R.N. 1995. Geotechnical Centrifuge Technology. Blackie Academic & Professional, London.

Towhata, I., and Al-Hussaini, T.M. 1988. Lateral Loads on Offshore Structures Exerted by Submarine Mudflows. Soil and Foundations, **28**(3): 26-34.

Vaid, Y.P., and Campanella, R.G. 1977. Time Dependent Behavior of Undisturbed Clay. Journal of Geotechnical Engineering, **103**(7): 693-709.

Vanneste, M. 2010. Offshore Geohazards. International Centre for Geohazards, Ulleval Stadion.

Yang, W. 2009. Physical Modeling of Subgouge Deformations in Sand, Memorial University of Newfoundland, St. John's.

Zakeri, A. 2009. Submarine Debris Flow Impact on Suspended (Free-Span) Pipelines: Normal and Longitudinal Drag Forces. Ocean Engineering(36): 489-499.

Zakeri, A., Hoeg, K., and Nadim, F. 2008. Submarine Debris Flow Impact on Pipelines - Part I: Experimental Investigation. Coastal Engineering, **55**(12): 1209-1218.

Zakeri, A., Hoeg, K., and Nadim, F. 2009a. Submarine Debris Flow Impact on Pipelines: Numerical Modeling of Drag Forces for Mitigation and Control Measures. Offshore Technology Conference: 1-11.

Zakeri, A., Hoeg, K., and Nadim, F. 2009b. Submarine Debris Flow Impact on Pipelines - Part II: Numerical Analysis. Coastal Engineering, **56**: 1-10.

Zakeri, A., Hoeg, K., and Nadim, F. 2009c. Submarine Debris Flow Impact on Pipelines: Drag Forces, Mitigation, and Control. Offshore Technology Conference: 10.

Appendix A
Details of Experiments

A.1 Load Cell Calibration

C-CORE	Calibration Sheet				Page 1 of 1
Description:	Moment Based Load Cell		Performed by:	Ken Chi	Equipment Used / Source Details:
Manufacturer:	C-CORE		Approved by:		hp Hewlett Packard, ID:34401A
Model Number:	Graduate Study		Date:	5/10/2010	attachment, ID: cal ps-001
Serial Number:	1		Excitation (volts):	5	weight scale, ID: 06626
Factory Calibration:	ADD		Notes:		
Factory Calibration Date:	ADD		ADD		

Engr Units 1	Voltage 1	Engr Units 2	Voltage 2	Results	
kg	mV	kg	mV	Slope 1	-1.324 kg / mV
0	0.594	0	0.585	Slope 2	-1.325 kg / mV
2.79	-1.56	2.79	-1.56	Average Slope	**-1.324 kg / mV**
7.33	-4.95	7.33	-4.96	R-square 1	1.000
2.79	-1.55	2.79	-1.57	R-square 2	1.000
0	0.59	0	0.583	Average	1.000
10.21	-7.13	10.21	-7.13	**Slope**	**-0.755 mV / kg**
					0.000 mV / v / kg

Cal Note:
ADD

Complete Update ALL red cells ONLY
Rename file with serial number in name
Sheet Version 1, 7 May 2009

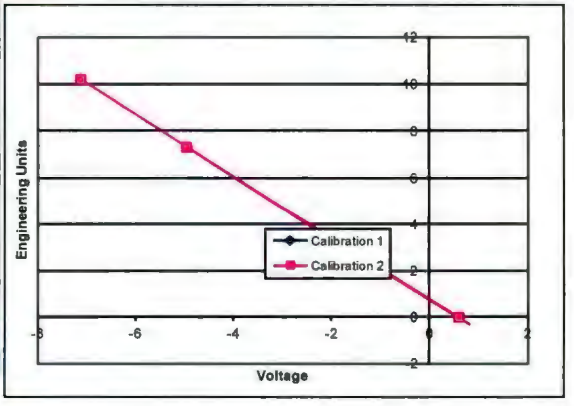

C-CORE	Calibration Sheet				Page 1 of 1
Description:	Moment Based Load Cell		Performed by:	Ken Chi	Equipment Used / Source Details:
Manufacturer:	C-CORE		Approved by:		hp Hewlett Packard, ID:34401A
Model Number:	Graduate Study		Date:	5/10/2010	attachment, ID: cal ps-001
Serial Number:	2		Excitation (volts):	5	weight scale, ID: 06626
Factory Calibration:	ADD		Notes:		
Factory Calibration Date:	ADD		ADD		

Engr Units 1	Voltage 1	Engr Units 2	Voltage 2	Results				
kg	mV	kg	mV	Slope 1	-1.333	kg	/	mV
0	2.375	0	2.376	Slope 2	-1.323	kg	/	mV
2.79	0.24	2.79	0.24	Average Slope	**-1.328**	**kg**	**/**	**mV**
7.33	-3.14	7.33	-3.19	R-square 1	1.000			
2.79	0.24	2.79	0.26	R-square 2	1.000			
0	2.376	0	2.376	Average	1.000			
10.21	-5.29	10.21	-5.33	**Slope**	**-0.753**	**mV**	**/**	**kg**
					0.000	**mV**	**/**	**v / kg**

Cal Note:
ADD

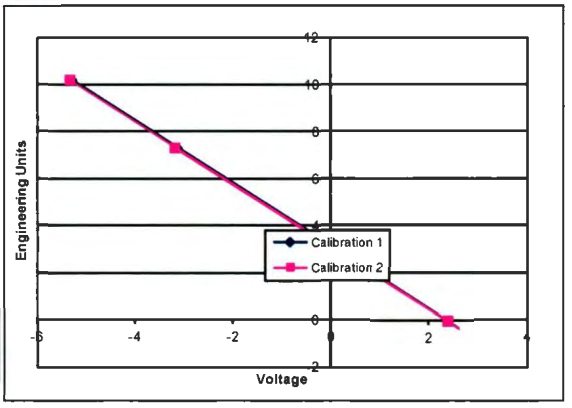

Complete/Update ALL red cells ONLY
Rename file with serial number in name
Sheet Version 1, 7 May 2009

C-CORE

Calibration Sheet

Page 1 of 1

Description:	Moment Based Load Cell	Performed by:	Ken Chi	Equipment Used / Source Details:	
Manufacturer:	C-CORE	Approved by:		hp Hewlett Packard, ID:34401A	
Model Number:	Graduate Study	Date:	5/10/2010	attachment, ID: cal ps-001	
Serial Number:	3	Excitation (volts):	5	weight scale, ID: 06626	
Factory Calibration:	ADD	Notes:			
Factory Calibration Date:	ADD	ADD			

Engr Units 1	Voltage 1	Engr Units 2	Voltage 2	Results				
kg	mV	kg	mV	Slope 1	-1.252	kg	/	mV
0	-0.651	0	-0.606	Slope 2	-1.252	kg	/	mV
2.79	-2.88	2.79	-2.88	Average Slope	**-1.252**	**kg**	/	**mV**
7.33	-6.52	7.33	-6.5	R-square 1	1.000			
2.79	-2.9	2.79	-2.88	R-square 2	1.000			
0	-0.611	0	-0.602	Average	1.000			
10.21	-8.78	10.21	-8.75	**Slope**	**-0.799**	**mV**	/	**kg**
					0.000	**mV**	/	**v / kg**

Cal Note:
ADD

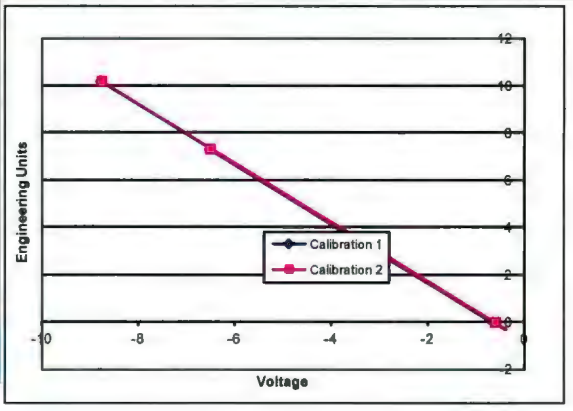

Complete Table ALL red cells ONLY
Rename file with serial number in name
Sheet Version 1, 7 May 2009

C-CORE

Calibration Sheet

Page 1 of 1

Description:	Moment Based Load Cell	Performed by:	Ken Chi	Equipment Used / Source Details:	
Manufacturer:	C-CORE	Approved by:		hp Hewlett Packard, ID:34401A	
Model Number:	Graduate Study	Date:	Nov/9/2010	attachment, ID: cal ps-001	
Serial Number:	4	Excitation (volts):	5	weight scale, ID: 06626	
Factory Calibration:	ADD	Notes:			
Factory Calibration Date:	ADD	ADD			

Engr Units 1	Voltage 1	Engr Units 2	Voltage 2	Results				
kg	mV	kg	mV	Slope 1	-1.344	kg	/	mV
0	-0.604	0	-0.608	Slope 2	-1.345	kg	/	mV
1.18	-1.47	1.18	-1.45	Average Slope	**-1.344**	**kg**	**/**	**mV**
2.79	-2.66	2.79	-2.64	R-square 1	1.000			
7.33	-6.05	7.33	-6.02	R-square 2	1.000			
2.79	-2.65	2.79	-2.63	Average	1.000			
1.18	-1.48	1.18	-1.46	**Slope**	**-0.744**	**mV**	**/**	**kg**
0	-0.605	0	-0.607		**#VALUE!**	**mV**	**/**	**v / kg**
10.21	-8.2	10.21	-8.2	**Cal Note:**				
				ADD				

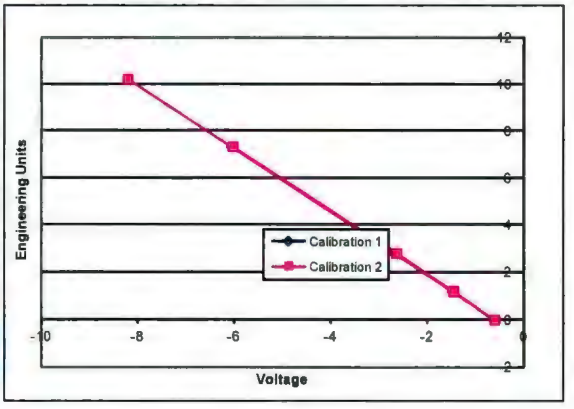

Complete/Update ALL red cells ONLY

Remove file with serial number in name

Sheet Version 1, 7 May 2009

A.2 Load Cell (System) Calibration

Applied Force* (N)	Load Cell Reading (millivolt)				Individual Recorded Force (N)				Combined Force* (N)	Percent Error (%)
	1	2	3	4	1	2	3	4		
0.0	1.33	0.34	-0.17	-1.19	0.0	0.0	0.0	0.0		
6.7	1.33	0.08	-0.46	-1.2	0.0	3.4	3.6	0.1	6.9	4%
76.6	1.35	-2.53	-3.23	-1.2	-0.3	37.4	37.6	0.1	75.0	-2%
85.2	1.36	-2.74	-3.46	-1.2	-0.4	40.1	40.4	0.1	80.5	-5%
155.2	1.37	-5.5	-6.41	-1.2	-0.5	76.1	76.6	0.1	152.7	-2%
155.2	1.38	-5.37	-6.29	-1.2	-0.6	74.4	75.2	0.1	149.6	-4%
76.6	1.38	-2.51	-3.22	-1.22	-0.6	37.1	37.5	0.4	74.6	-3%
6.7	1.33	0.008	-0.47	-1.21	0.0	4.3	3.7	0.3	8.0	20%
85.2	1.34	-2.78	-3.59	-1.22	-0.1	40.6	42.0	0.4	82.7	-3%
0.0	1.34	0.34	-0.19	-1.21	-0.1	0.0	0.2	0.3		

*Horizontal force

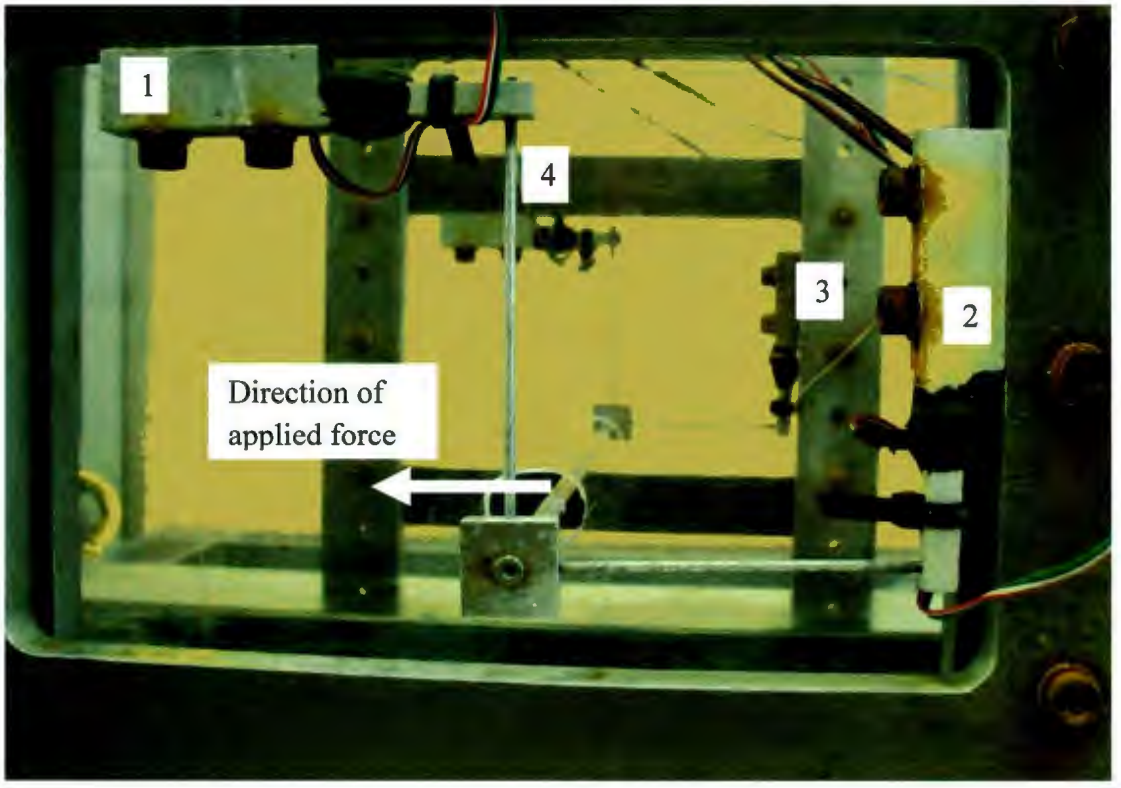

A.3 T-bar Calibration

C-CORE	Calibration Sheet				Page 1 of 1
Description: T-Bar - 01			Performed by:	Ken Chi	Equipment Used / Source Details:
Manufacturer: C-CORE			Approved by:		Hewlett Packard Multimeter, ID 34401A
Model Number:			Date:	7/29/2011	Addition, ID cal PS 001
Serial Number:			Excitation (volts):	5	Weight scale, ID 06626
Factory Calibration:			Notes:		
Factory Calibration Date:					

Engr Units 1	Voltage 1	Engr Units 2	Voltage 2
Kg	mV	Kg	mV
0	-1.4	11.73	0.06
2.75	-1.04	6.74	-0.6
6.74	-0.57	2.75	-1.05
11.73	0.06	0	-1.38
16.87	0.7		

Results		
Slope 1	8.060	Kg / mV
Slope 2	8.177	Kg / mV
Average Slope	**8.118**	**Kg / mV**
R-square 1	1.000	
R-square 2	0.999	
Average	0.999	
Slope	**0.123**	**mV / Kg**
	0.000	**mV / v / Kg**

Cal Note:
ADD

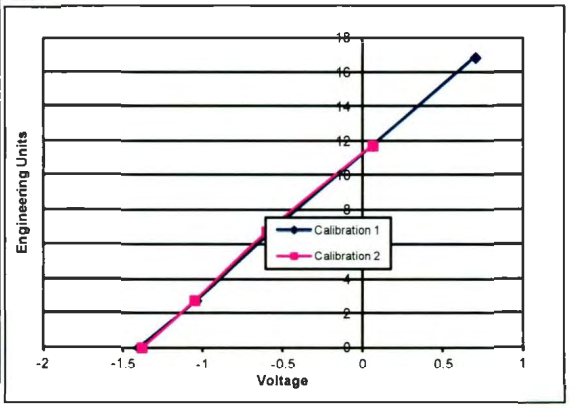

Complete/Update ALL red cells ONLY
Rename file with serial number in name
Sheet Version 1, 7 May 2009

A.4 Lab-Floor Consolidation

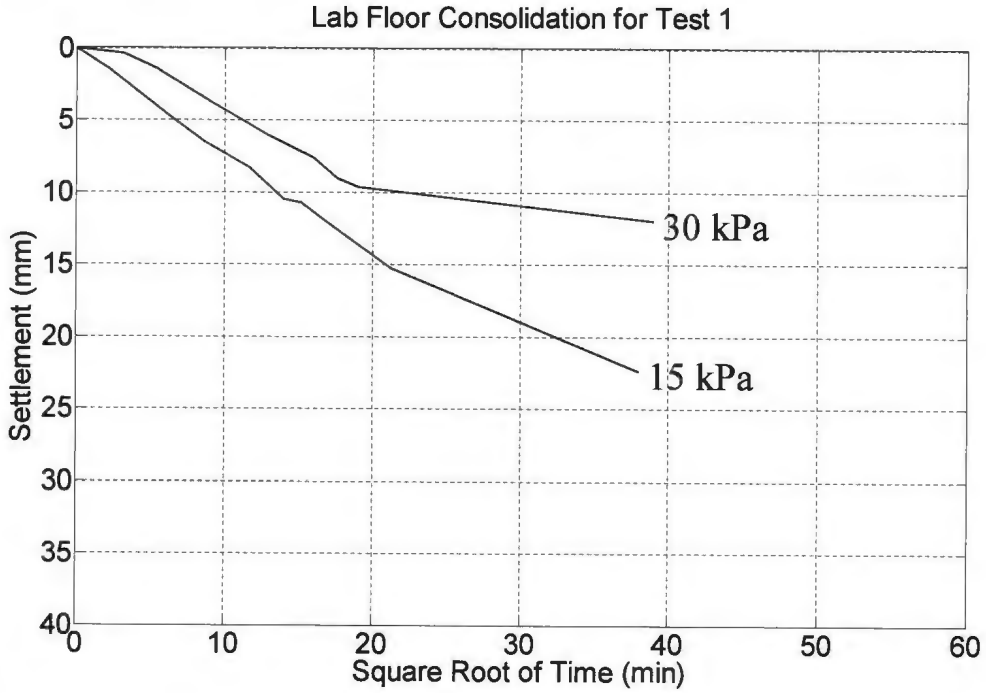

Data for 40 kPa consolidation stress was missing.

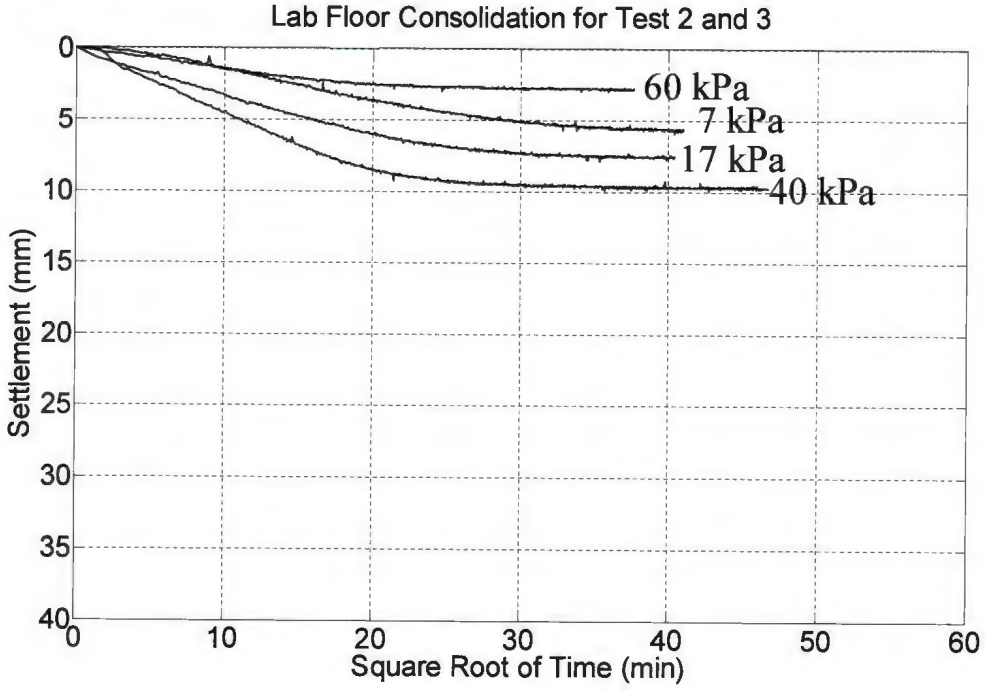

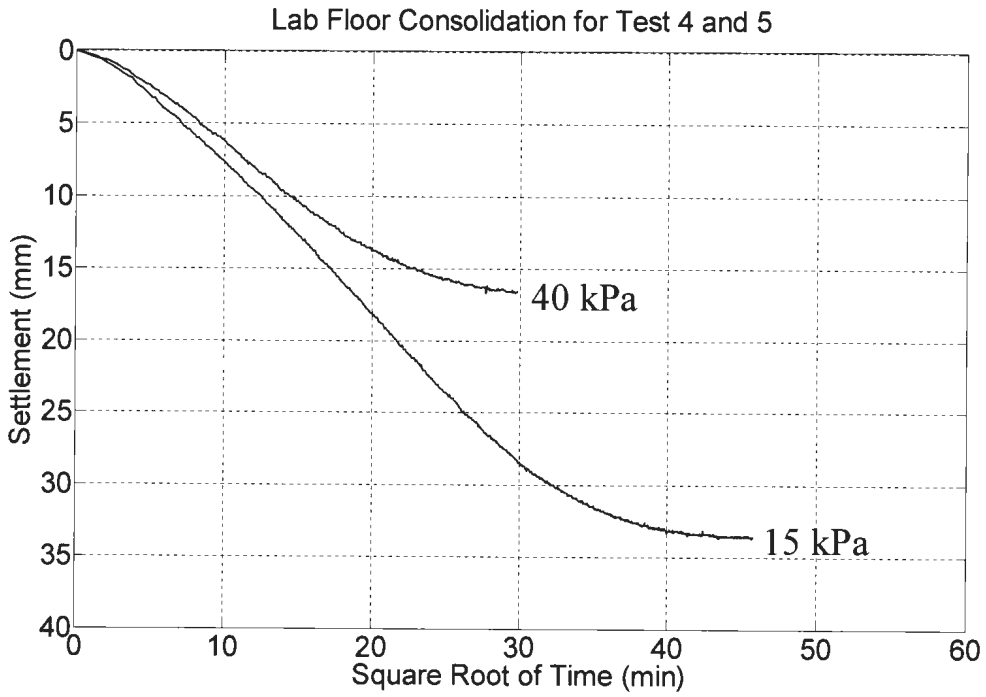

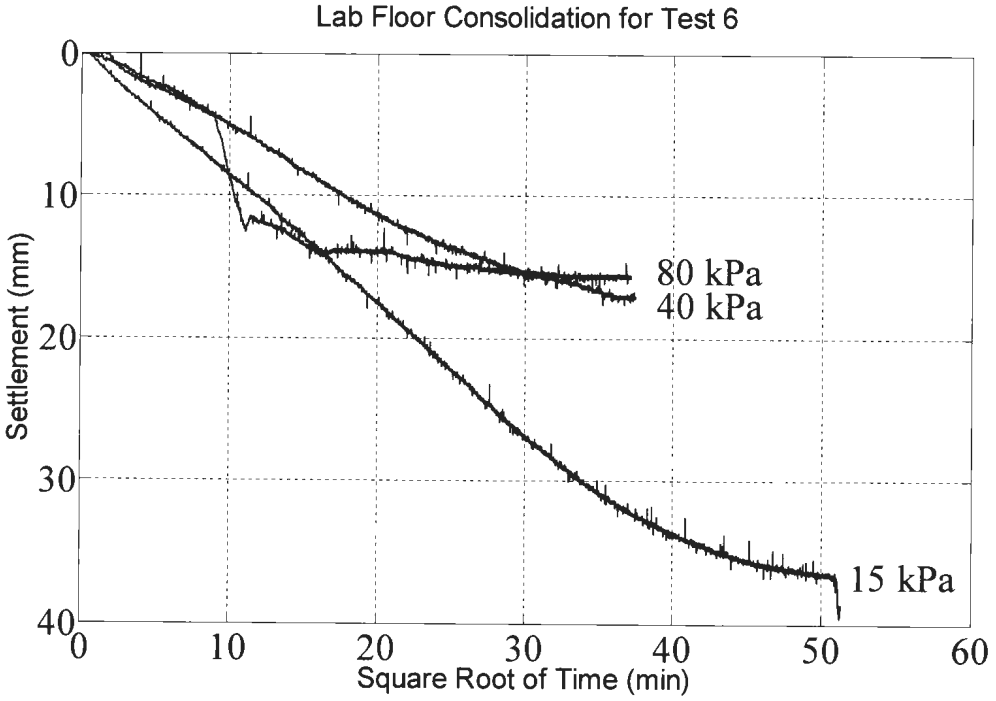

Test 7, 8, 9, and 10 data are missing.

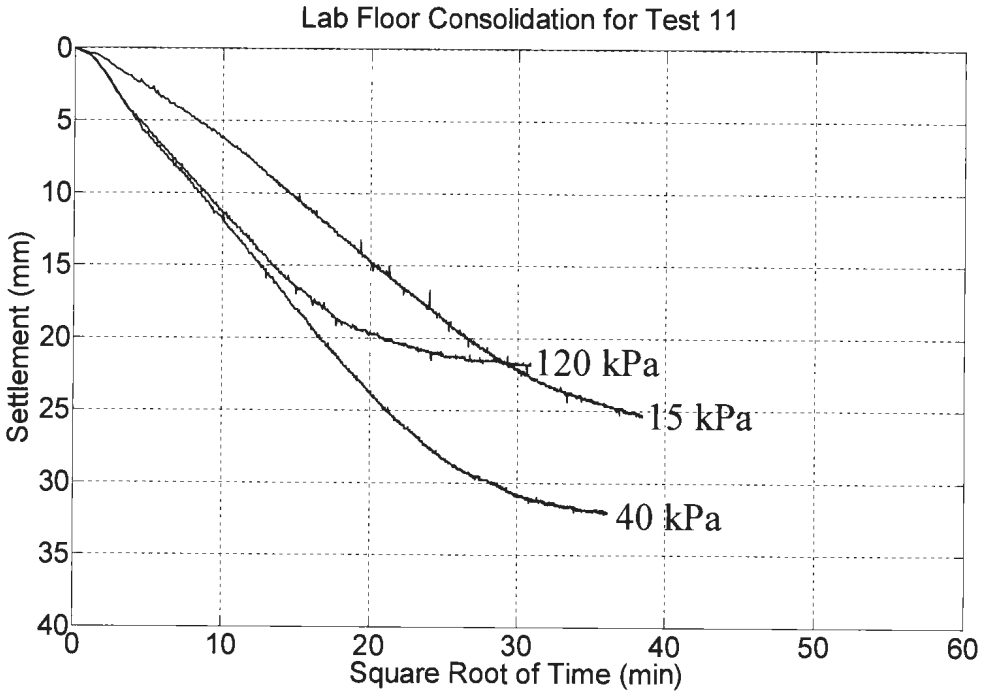
Lab Floor Consolidation for Test 11
Settlement (mm)
Square Root of Time (min)
0
5
10
15
20
25
30
35
40
0
10
20
30
40
50
60
120 kPa
15 kPa
40 kPa

A.5 Centrifuge Consolidation

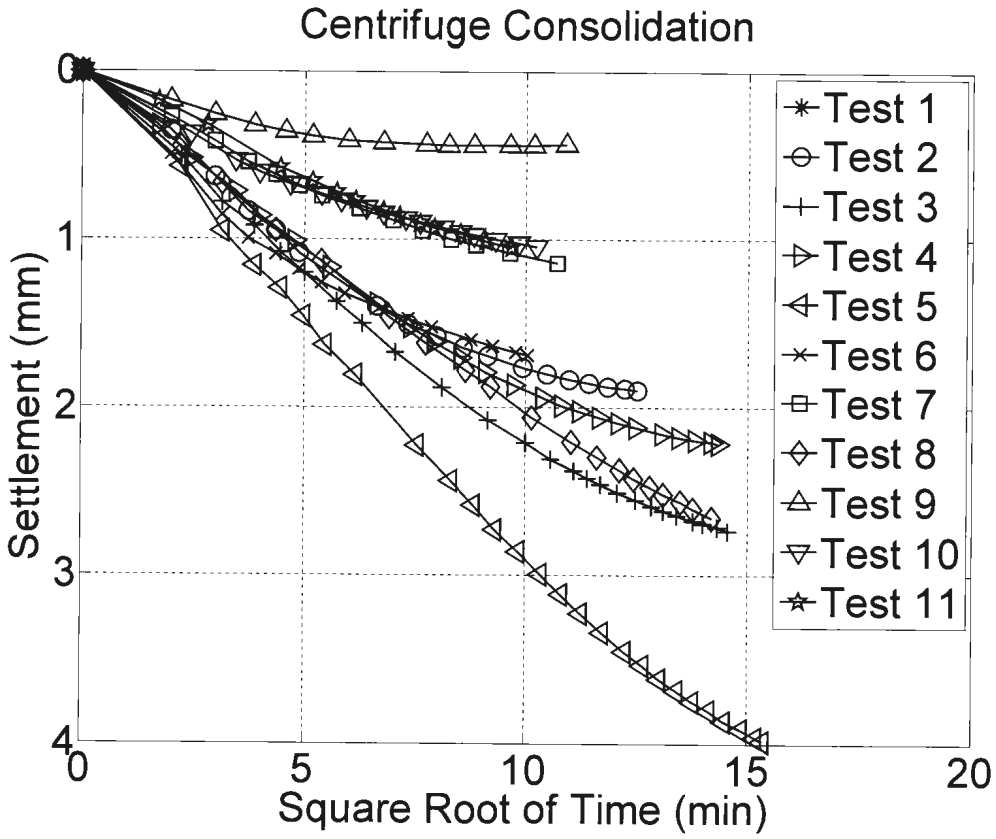

A.6 Undrained Shear Strength Profile

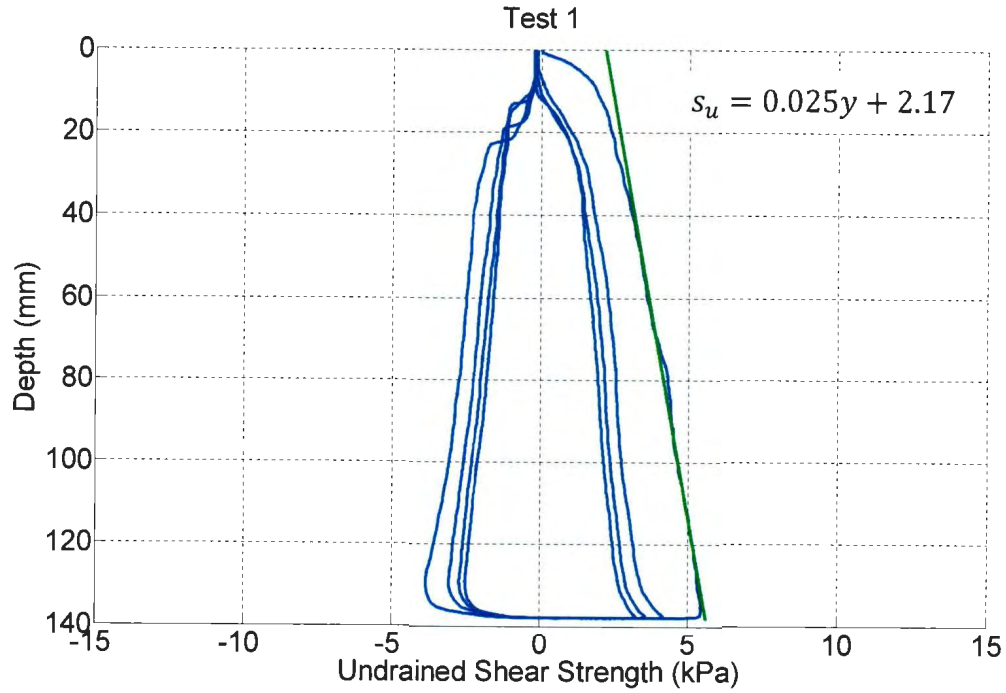

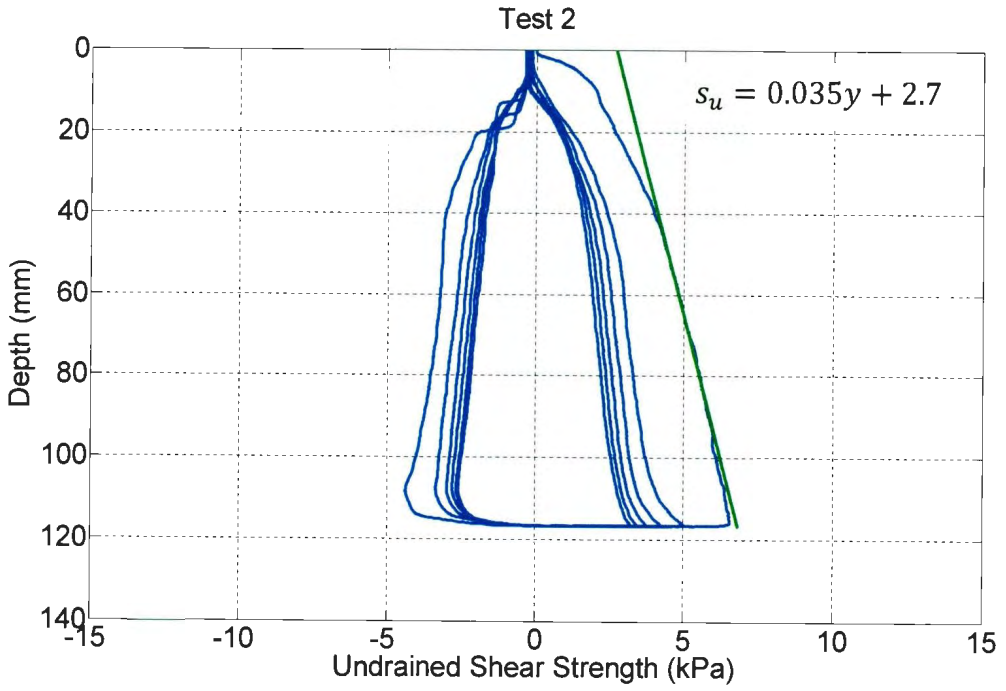

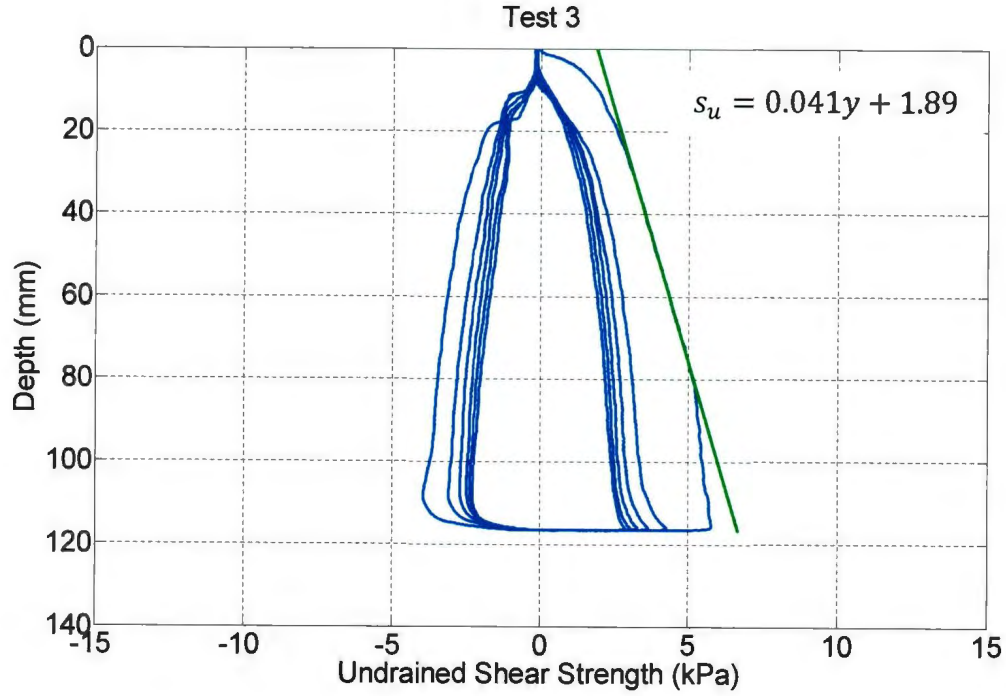
Test 3
$s_u = 0.041y + 1.89$
Depth (mm)
0
20
40
60
80
100
120
140
-15
-10
-5
0
5
10
15
Undrained Shear Strength (kPa)

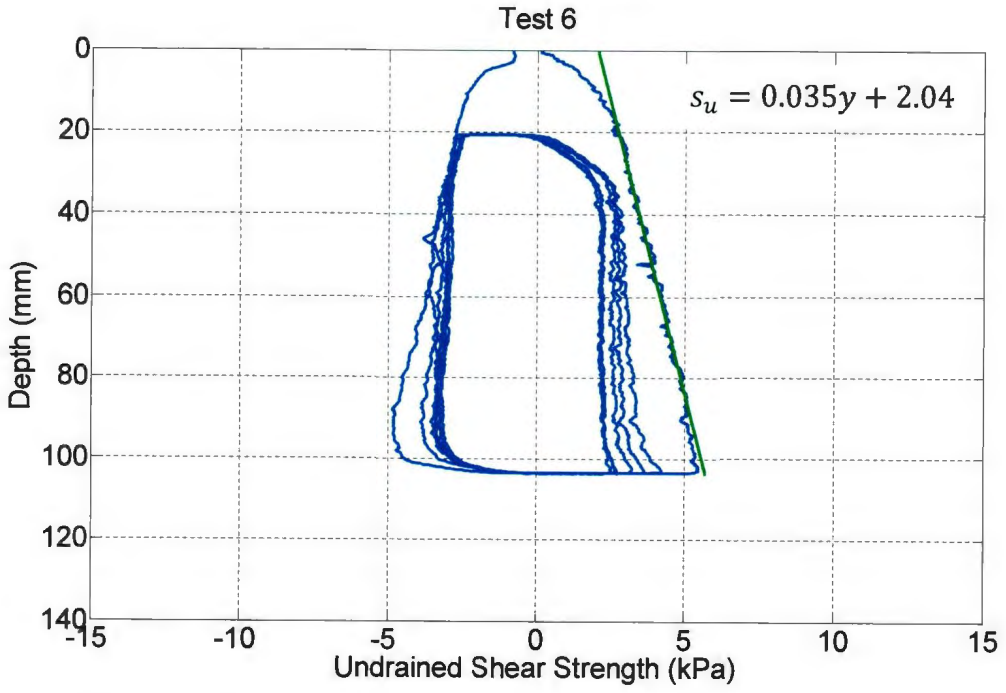
Test 6
$s_u = 0.035y + 2.04$
Depth (mm)
0
20
40
60
80
100
120
140
-15
-10
-5
0
5
10
15
Undrained Shear Strength (kPa)

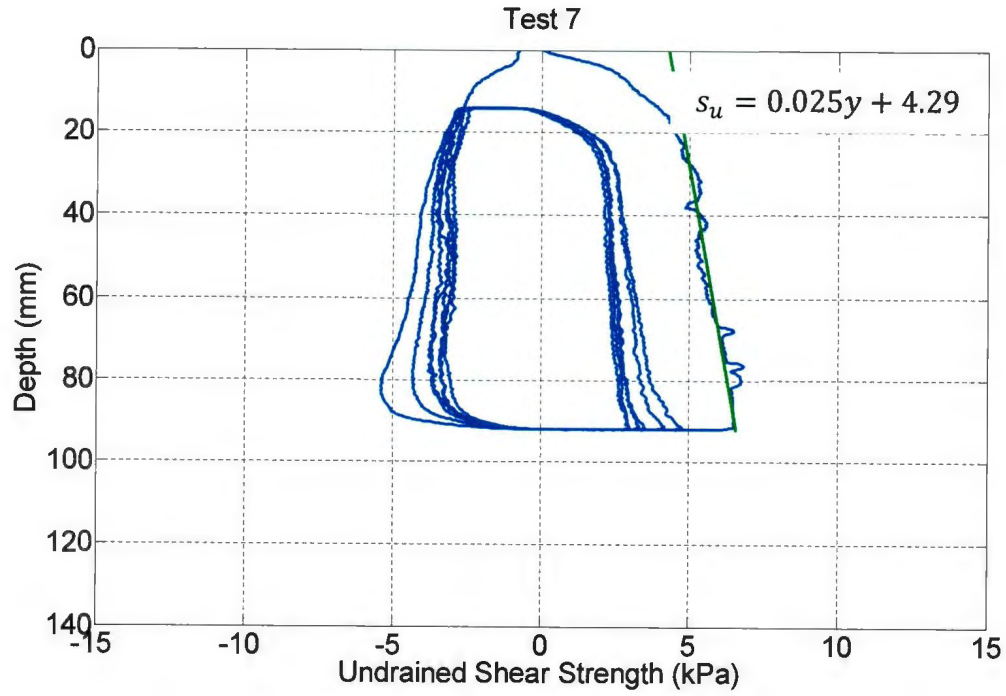
Test 7
$s_u = 0.025y + 4.29$
Depth (mm)
0
20
40
60
80
100
120
140
-15
-10
-5
0
5
10
15
Undrained Shear Strength (kPa)

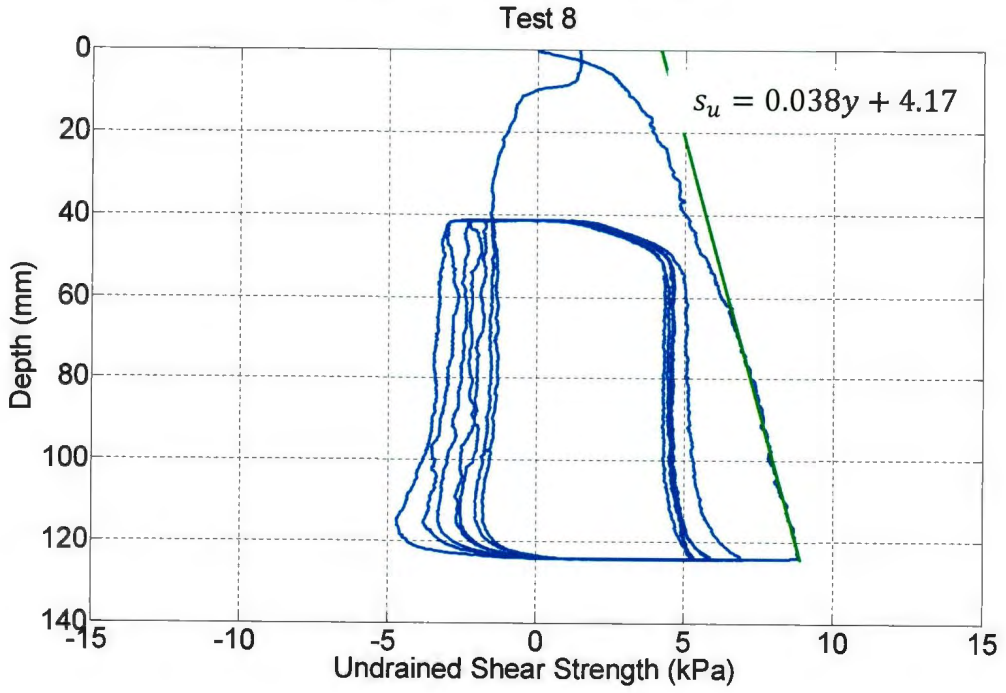
Test 8
$s_u = 0.038y + 4.17$
Depth (mm)
0
20
40
60
80
100
120
140
-15
-10
-5
0
5
10
15
Undrained Shear Strength (kPa)

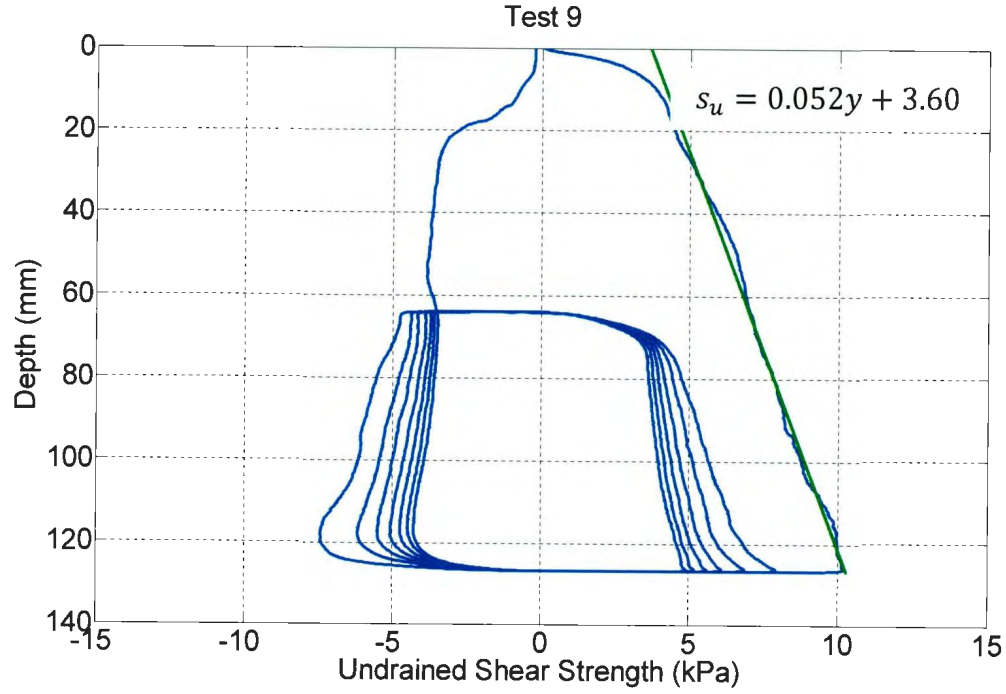
Test 9
$s_u = 0.052y + 3.60$
Depth (mm)
0
20
40
60
80
100
120
140
-15
-10
-5
0
5
10
15
Undrained Shear Strength (kPa)

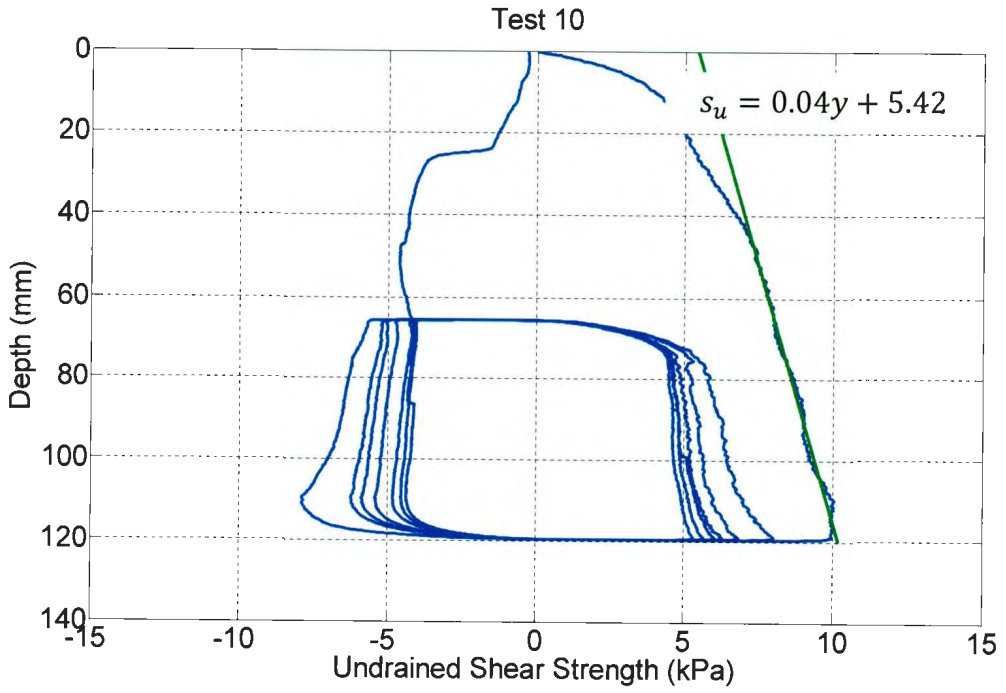
Test 10
$s_u = 0.04y + 5.42$
Depth (mm)
0
20
40
60
80
100
120
140
-15
-10
-5
0
5
10
15
Undrained Shear Strength (kPa)

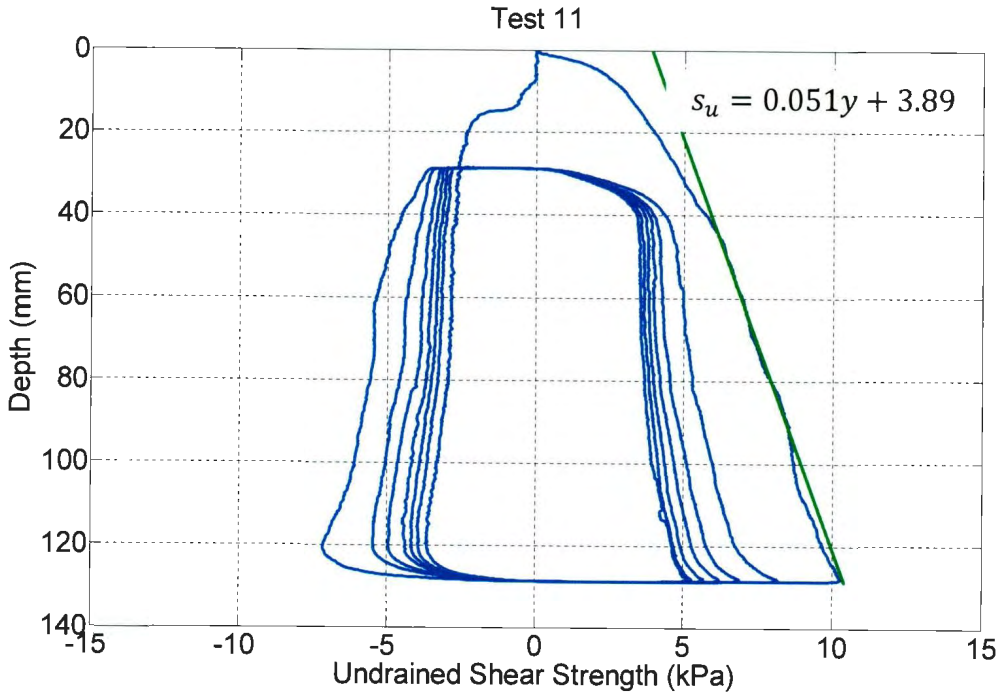
Test 11
$s_u = 0.051y + 3.89$
Depth (mm)
0
20
40
60
80
100
120
140
-15
-10
-5
0
5
10
15
Undrained Shear Strength (kPa)

A.7 Moisture Content Profile